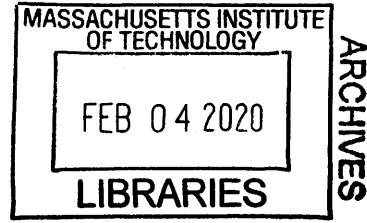


Integrated Photonic Devices for Spectroscopic
Chemical Detection

by

Derek Matthew Kita



B.S., Massachusetts Institute of Technology (2014)

Submitted to the Department of Materials Science and Engineering
in partial fulfillment of the requirements for the degree of

Doctor of Philosophy

at the

MASSACHUSETTS INSTITUTE OF TECHNOLOGY

February 2020

© Massachusetts Institute of Technology 2020. All rights reserved.

Signature redacted

Author

Department of Materials Science and Engineering
December 16, 2019

Signature redacted

Certified by

Juejun Hu
Associate Professor of Materials Science & Engineering
Thesis Supervisor

Signature redacted

Certified by

Lionel C. Kimerling
Professor of Materials Science & Engineering
Thesis Supervisor

Signature redacted

Accepted by

Donald Sadoway
Departmental Committee on Graduate Students

Integrated Photonic Devices for Spectroscopic Chemical Detection

by

Derek Matthew Kita

Submitted to the Department of Materials Science and Engineering
on December 16, 2019, in partial fulfillment of the
requirements for the degree of
Doctor of Philosophy

Abstract

Chemical sensing systems realized with photonic components integrated on traditional semiconductor substrates have emerged as a promising technology for remote sensing applications that require low cost, low power consumption, light weight, small size, and high-performance. In this thesis, I discuss methods and systems for practical implementations of chip-scale integrated photonic chemical sensors and spectrometers. The work focuses on solutions to a variety of obstacles that have hindered real-world implementations of microphotonic chemical sensors. First, a new chip architecture capable of acquiring high channel count, high resolution optical spectra (200 pm resolution in the telecommunications C-band) is presented both theoretically and experimentally, along with a new ‘elastic- D_1 ’ regularized regression method for spectrum reconstruction. Next, evanescent field sensing using dielectric waveguides is studied theoretically and numerically, with a special emphasis on sensing performance in the presence of random, fabrication-induced waveguide sidewall roughness. I demonstrate that a locally flat perturbation approximation is valid for typical experimental roughness in silicon-on-insulator platforms, and use a volume-current method to explicitly compute scattering loss rates for a variety of three-dimensional waveguide structures. To then experimentally realize photonic sensing systems, I developed a low-loss (0.36 ± 0.11 dB/cm), quick-turn (16.4 day turnaround) fabrication process for inexpensively prototyping silicon nitride photonic integrated circuits with heaters, etched edge couplers, and opened sensing windows. Using this fabrication process, I present a successful experimental demonstration of a fiber-packaged, waveguide-enhanced Raman spectroscopic sensor used for detecting liquids in contact with the surface of the chip via measured Raman peaks from $500 - 3500$ cm^{-1} .

Thesis Supervisor: Juejun Hu

Title: Associate Professor of Materials Science & Engineering

Thesis Supervisor: Lionel C. Kimerling

Title: Professor of Materials Science & Engineering

Acknowledgments

I am grateful to so many people that have become a part of my life over the last decade in Cambridge through both undergraduate and graduate studies. Colleagues, supervisors, mentors, and friends have all helped and supported me in unimaginable and unexpected ways. Without all these people in my life, I truly would not be where I am today.

I must thank my parents and my older sister for supporting me throughout my entire life and helping me become the person I am today. Your presence in my life (even if thousands of miles away) has meant so much to me. I'm so grateful to have family that I could both confide in when times were rough, and call with excitement when things were going well.

I am tremendously grateful to Professor Juejun Hu, for always making time to individually meet with me, for providing help when I needed it, and for giving me the freedom and independence to find my own way. His positive spirit made research in the group fun, and I will always remember feeling optimistic at the conclusion of each of our many meetings.

I am also thankful to Professor Lionel Kimerling, who supported me on my journey in photonics ever since I was an undergrad (by giving me a research assistant position as a freshman in 2010). I will forever remember the profound impact he has had on my professional development, and the time he almost convinced JEOL in Tokyo to give me an SEM that I could put in my apartment. Thank you Professor Polina Anikeeva for sparking my interest in electronic and photonic materials and for guiding me through the PhD experience. And thank you, Professor Yoel Fink for also being a caring and supportive committee member. I must also thank Dr. Jurgen Michel, Dr. Anu Agarwal, and Professor Kazumi Wada for making myself (as well as all students) feel included and welcomed into the group.

I also had the opportunity to work with Professor Steven Johnson in the Department of Mathematics on fabrication induced roughness loss in optical waveguides. Thank you Professor Johnson for your willingness to collaborate and provide guid-

ance for this project.

I am tremendously grateful to the entire team at the Microsystems Technology Laboratory (MTL) for keeping the tools up and running, training me on new equipment and procedures, passing on their fabrication experience, and keeping all of us MTL users safe in the cleanroom. Thank you Mark Mondol, Kurt Broderick, Dennis Ward, Eric Lim, Jorg Scholvin, Vicky Diadiuk, Gary Riggott, Bob Bicchieri, and Paudely Zamora.

I also owe a great deal to the help, guidance, and instruction provided by David Bono and Brian Neltner. Thank you for patiently helping with electronics projects, and for teaching me best practices when building quality measurement systems and equipment.

I must pay tribute to the older graduate students in my lab that came to MIT in the winter of 2014 from University of Delaware that taught me best practices in the cleanroom and helped build the lab up to what it is now. Hongtao Lin, Lan Li, Tony Ogbuu, Yi Zou, Qingyang Du, and Sarah Geiger are among the individuals who helped build up the lab and spent countless hours teaching us newer students in cleanroom fabrication, test, and design of photonic devices. Carlos Rios and Samuel Serna, thank you for inspiring me to learn about exciting topics in photonics and for bringing such valuable experience to the group. Peter Su, Skylar Deckoff-Jones, Evi Postelnicu, Yifei Zhang— I am very glad our group managed to recruit you all and have enjoyed our conversations. Thank you Brando Miranda, for so willingly collaborating with me on the on-chip Fourier transform spectroscopy project, and for being a true friend. Thank you to Kyle Markland, David Favela, Cedric Delmy, and Fayed Ali for your help as undergraduate researchers on several of my research projects.

The acknowledgments would not complete without a dedicated sentence (or paragraph) for the labmate who sat two desks to my left nearly every day for the last five years. Thank you Jérôme Michon for being such a good friend and for inspiring me to grow as a researcher. Your passion for good science has been an asset to many fun and exciting projects. In fact, much of the work of this thesis was done in close

contributions.

Thankfully, my life extended beyond research (though often it did not seem this way). I would like to thank Alex Tinguely, Seth Cazzell, Kevin Bogaert, Jonathan Hwang, and Owen Morris for being great friends and making graduate school fun.

Finally, I owe a huge debt to Kristen, my best friend and fiancé. Your love and support has been the brightest light in my life. I cannot wait for our continued adventures together.

To everyone who has become a part of my life (in a big or small way)– *thank you!*

Contents

1	Introduction	25
1.1	Background	25
1.2	On-chip spectroscopic chemical detection	27
1.3	Chemical sensing methods	28
1.3.1	Absorption spectroscopy	28
1.3.2	Raman spectroscopy	30
1.3.3	Refractive index sensing	33
1.4	Evanescent-field waveguide sensing	35
1.5	On-chip spectroscopy	37
1.5.1	Echelle gratings	37
1.5.2	Arrayed waveguide gratings	39
1.5.3	Fourier transform spectrometers	41
1.6	Thesis overview	44
2	A reconfigurable waveguide integrated Fourier-transform spectrom- eter	47
2.1	Introduction	47
2.2	dFT Architecture and Scaling Laws	50
2.3	Experimental demonstration	51
2.4	Spectrum reconstruction	53
2.5	Discussion	56

3	Optimized waveguide geometries for evanescent field sensing in the presence of sidewall roughness	59
3.1	Introduction	60
3.2	Sensing Figures of Merit	62
3.3	Scattering-loss calculations	65
3.4	Comparison of Waveguide Geometries	67
3.5	Comparison with experiment	70
3.6	Concluding Remarks	72
4	A quick-turn fabrication process for Si₃N₄ photonic integrated circuits with heaters	75
4.1	Introduction	75
4.2	A quick-turn silicon nitride photonics process	77
4.3	Device performance	82
4.4	Economic analysis and fab-metrics	87
4.5	Conclusion	91
5	A packaged, fiber-coupled waveguide-enhanced Raman spectroscopic sensor	93
5.1	Introduction	93
5.2	Chip design and fabrication	95
5.3	Measurements	99
5.4	Analysis of backscattered Raman signal	100
5.5	Conclusion	102
6	Conclusion & future directions	105
6.1	Broader challenges	105
6.2	Ultra high channel-count Fourier transform spectrometers	107
6.2.1	Perfect optical switching	108
6.2.2	Spectrally segmented optical switching	110
6.2.3	Arm-loss balancing	110

6.2.4	Fringe alignment	111
6.3	Volume-current method applied to platforms for Raman spectroscopy	111
6.4	Fully integrated spontaneous Raman spectroscopy systems	112
A	dFT spectrometer characterization and reconstruction methods	117
A.1	Elastic- D_1 spectral reconstruction method	117
A.2	Insertion loss measurements of the dFT spectrometers	122
A.3	Modulation efficiency estimates for thermo-optic and electro-optic phase shifters	123
A.4	Temperature dependence of the dFT spectrometer	124
A.5	Performance benchmarking	124
B	Roughness calculations	129
B.1	Figure of merit for absorption spectroscopy and refractometry	129
B.1.1	Absorption sensing	129
B.1.2	Mach-Zehnder refractometry	131
B.1.3	Ring-resonator refractometry	132
B.2	Spontaneous Raman spectroscopy figure of merit	133
B.3	Polarizability of rough surfaces	139
B.4	Volume-current method calculations	142
C	Software and measurement systems	145
C.1	PICwriter: A python module for generating GDSII masks for integrated photonics	145
C.1.1	Example usage	146
C.2	A semi-automated wafer-scale testbed for integrated photonics	147
C.3	A photonics data acquisition module for silicon nitride PICs with thermal tuners	150

List of Figures

1-1	Closeup camera image of a 2.5×5.0 mm wide Fourier-transform spectrometer photonic chip with optical fiber connections and metal wirebonds, mounted atop a thermo-electric cooler for temperature control. Information regarding the spectrometer’s operating principles is discussed in Chapter 2	27
1-2	Infrared absorption spectra of isopropyl alcohol, acetone, and methane. Data from NIST Chemistry WebBook [183].	30
1-3	Vibrational energy states with depictions of transitions for infrared absorption, Stokes Raman scattering, and Anti-Stokes Raman scattering.	31
1-4	Raman spectra of acetaminophen, acquired on a Chromex Sentinel portable Raman system [59].	32
1-5	Schematic of a simple dielectric waveguide with exposed top cladding for evanescent-field sensing. Light travels in the out-of-plane direction, and the evanescent portion of the electric field interacts with nearby chemicals to generate a measurable signal.	36
1-6	Schematic of an Echelle grating spectrometer with $N = 5$ outputs (not to scale), and below is a sample output spectrum for a device with $N = 11$ outputs, the response of which is given by Equation 1.17. . .	38
1-7	Schematic of an arrayed waveguide grating (AWG) with $M = 7$ optical delay lines and $N = 5$ outputs (not to scale).	40

1-8	(a) Schematic of a free-space Mach-Zehnder interferometer with phase delay $\Delta\phi$ between the two interferometer arms, made up of two beam splitters (BS), two mirrors, and two photodetectors (PD). (b) Waveguide integrated Mach-Zehnder interferometer, comprising of two 50:50 power couplers, a phase tuning element, and two output photodetectors. At bottom are the scattering matrices of the beamsplitter and phase delay elements.	42
2-1	(a) Block diagram illustrating the generic structure of a dFT spectrometer with j switches and $K = j/2 - 1$ repeated stages indexed by $k \in [1, K]$; (b) photo of the fully-packaged, plug-and-play dFT spectrometer with standard FC/PC fiber interface and a ribbon cable for control and signal read-out; (c) top-view optical micrograph of the 64-channel dFT spectrometer after front-end-of-line silicon fabrication, showing the interferometer layout, the thermo-optic switches and waveguide-integrated germanium photodetector.	49
2-2	Packaged dFT photonic integrated circuit (PIC) and spectral basis set. (a) Schematic diagram of the dFT spectrometer characterization setup; (b) an exemplary transmission spectrum of the dFT device corresponding to an arm length difference of 0.7 mm; (c) transmission spectra of the device for all 64 permutations of the switch on/off combinations: the ensemble of 64 spectra constitute the basis set for spectrum reconstruction.	51
2-3	Sparse signal reconstruction. (a) Spectra consisting of two laser lines with varying spacing measured using the 64-channel dFT spectrometer and reconstructed by applying the elastic- D_1 algorithm. Insets (b) and (c) show zoomed-in images of the narrow spectral features for input laser lines with 100 pm and 200 pm spacing, respectively.	52

2-4 Broadband signal reconstruction. Three unique light sources with broad spectral features were measured using the dFT spectrometer chip and elastic- D_1 method (top red curves) and compared to measurements by a benchtop optical spectrum analyzer (OSA) (bottom black curves). The three light sources were generated using amplified spontaneous emission from an erbium doped fiber passed through several Mach-Zehnder interferometers (additional information is provided in the Methods). 55

3-1 Top row: vertically symmetric surface roughness along a silicon strip waveguide on silicon dioxide substrate, a slot waveguide, and a SWG waveguide. The electric field magnitude $|\vec{E}|^2$ is overlaid at several cross-sections. Second (from top) to fourth rows: external (bulk) confinement factor Γ , surface confinement factor Γ (field integral over 8 nm thin region at air/solid interface), and the *normalized* Raman gain coefficient β' , respectively, for each single-mode waveguide geometry as a function of the relevant design parameters (total width, slot size, and duty cycle). Shaded regions denote the relative y-axis scaling between adjacent plots in each row. For slot waveguides, the total width is denoted as follows: $\triangle=450$ nm, $\square=550$ nm, and $\times=650$ nm. For SWG waveguides, the width and period are fixed to 550 nm and 250 nm, respectively. The surface Γ and bulk Γ are calculated via first-order perturbation theory (which is exactly equivalent to Eq. 3.3) with a resolution of 256 pixels/ μm and for SWG waveguides with a resolution of 128 pixels/ μm . The Raman gain coefficients are computed via Eq. 3.4 and 3.5 in 3-dimensions with a resolution of 128 pixels/ μm 63

3-2	Relative scattering loss $\alpha_s / \max(\alpha_{s, \text{TE-strip}})$ computed by FDTD simulations of vertical (y -direction) lines of dipole moments and averaged over all sidewall positions. Dipole moment amplitudes were computed via Eq. 3.6 with incident field strength and phase determined by numerically computed mode profiles. Results shown for TE (red) and TM (blue) strip (left), slot (middle), and SWG (right) waveguides. For slot waveguides, the total width is denoted as follows: $\triangle=450$ nm, $\square=550$ nm, and $\times=650$ nm.	67
3-3	Side-by-side performance comparison for strip (left column), slot (middle column), and SWG (right column) waveguides in the presence of slow-varying ($L_c > 10 \cdot \sigma$) Gaussian random roughness. Normalized absorption sensing figure of merit FOM_Γ and normalized Raman gain coefficient $\text{FOM}_{\beta'}$ calculated via Eq. 3.1 and 3.2, respectively, as a function of the relevant design parameters (total width, slot size, and duty cycle). For slot waveguides, the total width (as depicted in Fig 3-1) is denoted as follows: $\triangle=450$ nm, $\square=550$ nm, and $\times=650$ nm.	70
3-4	Comparison of the ratio of scattering losses between different experimentally realized waveguide systems. Red square markers denote loss ratios computed via the volume-current method described in this work and black circles denote reported loss ratios with associated error bars. Slot waveguides reported by Debnath <i>et al.</i> [41] and Baehr-Jones <i>et al.</i> [13] are labelled by the slot size, while slot waveguides by Ding <i>et al.</i> [52] are labelled by “slot1”, “slot2”, etc. corresponding to different slot sizes and strip-loading values. Bock <i>et al.</i> [25] and Gnan <i>et al.</i> [67] report losses for SWG and strip waveguides fabricated via electron beam lithography.	71
4-1	Cross-sectional schematic of the full layer stack after processing as outlined in Table 4.1.	78

4-2 Numerically computed mode cutoffs for the first two quasi-TE and quasi-TM waveguide modes of the partially etched 200 nm thick Si₃N₄ waveguides. Each line corresponds to a 5 dB/cm iso-loss contour, and is superimposed on top of the first TE mode effective index. Single-mode operation occurs for waveguide geometries between the solid and dashed lines. 83

4-3 Experimentally measured transmission for an all-pass resonator used to determine the silicon nitride waveguide propagation loss. 84

4-4 (a) Top-down SEM image of the inverse taper (spot size converter) used for expanding the waveguide mode at the chip edge. The anchor at top prevents the narrow resist from falling over and is completely etched away at process step 22. (b) Cross-sectional (side) SEM image of the oxide sidewall after deep reactive ion etching of the silicon dioxide and silicon. For this particular sample, the deposited TEOS oxide was 3 μm thick, and the sidewall angle is 76.3°. (c) 45°tilted SEM image of the etched edge of the chip, with a deep-etched trench for the optical fiber on the left. (d) Optical microscope image of a single-mode fiber coupling light into the waveguide mode via the spot size converter and bonded in place with UV curable epoxy. 85

4-5 (a) Top-down scanning-electron microscope image of a waveguide sensing region, where the top TEOS oxide has been selectively removed by both reactive ion-etching and then wet etching with hydrofluoric acid. (b) An optical microscope image of λ=808 nm light travelling through the waveguides from left to right. A small amount of far-field optical scattering is noticeable at the transition when the waveguide exits the region with top oxide cladding. Most optical loss occurs in the sensing region due to waveguide sidewall roughness or scattering from particulates that settle on the surface. 86

4-6	(a) Experimentally measured transmission through a balanced Mach-Zehnder modulator (MZM) as a function of heater power at a wavelength of 1550 nm. (b) Measured heater impedance as a function of drive power up until failure (marked by ‘X’) for two different heater widths.	88
4-7	Economy of scale (cost per unit area) for the MIT silicon nitride integrated photonics platform, as a function of the waveguide layer fill-fraction. We assume a chip size of $5 \times 5 \text{ mm}^2$ and 150 mm^2 wafers. The electron-beam lithography write speed [minutes/cm ²] was empirically found to obey $1672.9 \cdot \text{FF} + 3.08735$, where FF is the pattern fill-fraction. At sufficiently high chip volumes, cost from electron-beam lithography dominates. Discontinuities at increasing number of chips indicate incremental increases in the number of wafers required for fabrication, at which cost initially jumps up due to the sparse number of chips on the newly added wafer.	89
4-8	Probability of completing a full fabrication process as a function of workdays. The expected time for completion of a process with 1 wafer is 16.4 days with a 10% probability of finishing in 4.1 days and 90% in 33.1 days. For 5 wafers the expected completion time is 21.0 days with a 10% probability of finishing in 9.0 days and 90% in 37.3 days.	90
5-1	Rendering of the photonic chip design fabricated in this work. A 2×2 directional coupler splits light into two waveguide channels, a MMI converter transforms the strip to a slot mode, and then in an exposed sensing region Raman scattered light is coupled into the backward-propagating waveguide mode. Components are not to scale.	95

5-2	(a) Rendering of the chip enclosure with optical fibers affixed to the chip and a flow cell that lowers onto the surface of the chip. The top case and flow channels are machined from PTFE, a rubber Kalrez [®] O-ring separates the chip from the top case, and the bottom fixture is machined from aluminum. (b) Photograph of the fiber-coupled, packaged Raman sensing chip with fibers glued to the edge of the chip after being mounted in separate glass v-groove chips (for mounting purposes). (c) The packaged chip with the top PTFE cell secured above the chip.	96
5-3	(a) Measured Raman spectra of mixtures of isopropyl alcohol (IPA) and water at different weight fractions, post background subtraction and baseline correction. Each spectra is the result of 15× 60 second integration times. The standard deviation on each wavelength measurement is approximately 2.9 counts. (b) Full spectrum of the 100% IPA measurement.	98
5-4	Numerically computed values of (a) the relative Raman gain coefficients (normalized by the 50 nm TE slot value) computed via field integrals over the top clad (sensing) region, assuming water as the solvent, (b) the scattering loss α_s computed via the volume-current method, (c) the pump rejection ratio $10 \log_{10}(\eta)$, where η is given by Eq. (5.6), and (d) the Raman sensing figure of merit $\beta'_{\text{Raman}}/\alpha_s$ with data interpolated from (a) and (b). Slot waveguides are all 800 nm wide (from one outer edge to the other).	104
6-1	Overview of potential improvements to the reconfigurable Fourier-transform spectrometer concept. Figure reproduced with permission from Kita, <i>et al</i> [96]	108

6-2	(a) Image of a fiber bonded and electrically wirebonded silicon nitride dFT spectrometer PIC. Images (b) and (c) depict 12- and 10-switch dFT spectrometers, respectively, with 4096 and 1024 unique optical path length difference permutations.	109
6-3	Analysis of quasi-TE polarized, 100 nm thick, Si ₃ N ₄ strip and slot waveguides for Raman sensing. Numerically computed values of (a) the Raman gain factor in the cladding, (b) Raman gain factor in the waveguide, (c) scattering loss, (d) pump rejection ratio, and (f) Figure of Merit for 100 nm thick silicon nitride waveguides (strip and slot) clad in water with a pump wavelength of $\lambda = 808$ nm depicted in (e). Volume current method FDTD resolution used is 64 pixels/ μm , and eigenmode solver resolution is 256 pixels/ μm (used both for volume current method and field integrals for the Raman gain factor).	115
A-1	Comparison of reconstruction techniques. Images of reconstructed spectra for two different optical inputs: two CW laser lines with 15 nm wavelength detuning (a,c,e) (as depicted in Figure 2-3 bottom) and a broadband signal generated by EDFA amplified spontaneous emission (b,d,f) (Figure 2-4c). The reconstruction techniques shown are: pseudoinverse (a,b), ridge regression (c,d), and LASSO (e,f). The R^2 scores and associated hyperparameters (which were selected through cross-validation) are shown as insets.	120
A-2	Comparison of reconstruction techniques. Images of reconstructed spectra for two different optical inputs: two CW laser lines with 15 nm wavelength detuning (a,c,e) (as depicted in Figure 2-3 bottom) and a broadband signal generated by EDFA amplified spontaneous emission (b,d,f) (Figure 2-4c). The reconstruction techniques shown are: BPDN (a,b), RBF Network (c,d), and elastic net (e,f). The R^2 scores and associated hyperparameters (which were selected through cross-validation) are shown as insets.	121

A-3	Schematic of dFT spectrometers. Block diagram of the fabricated 1-stage (a), 2-stage (b), and 3-stage (c) dFT spectrometers fabricated all on a single chip. Orange denotes optical paths and passive optical components, while blue denotes active photonic components (heaters and photodetectors), and green denotes electrical wiring (metal traces).	122
A-4	Temperature dependence of narrowband dFT reconstructions. (a) Measured detuning of the center wavelength (given an input laser at constant wavelength of $\lambda = 1560.0$ nm) for different temperatures as measured by a thermistor near the photonic chip. Images at bottom show the reconstructed laser line for a number of different temperatures across the full 20 nm band (b) and a zoomed in image is provided to show the change in center wavelength (c).	125
B-1	Numerically computed Fourier components of the polarizability for a randomly generated surface with Gaussian correlation length and a unit-valued incident field parallel (left) and perpendicular (right) to the interface for different ratios of L_c/σ . Black dashed lines correspond to the analytical polarizabilities of $\alpha_{\parallel} = 11.1$ and $\gamma_{\perp} = 0.92$ for a flat shifted silicon/air interface. Gray shaded regions correspond to Fourier-components of the roughness that scatter light into the far-field and red shaded regions correspond to components that reflect light in the backwards direction (β_{wg} corresponds to the range of propagation coefficients for all waveguide-geometries considered in this text, and is scaled assuming a roughness correlation length of 75 nm and wavelength of $\lambda=1550$ nm). Colored errorbars denote the standard error of the mean for multiple computations.	138

B-2	Computed changes in the perturbed polarization density $\Delta P(\vec{r}) \cdot \hat{z}$ along a rough waveguide sidewall with short ($L_c/\sigma = 0.2$), medium ($L_c/\sigma = 1.0$), and long ($L_c/\sigma = 20$) correlation lengths with respect to the RMS roughness σ . Solid black line shows the perturbed sidewall, and dashed black line shows the straight, unperturbed sidewall. . . .	139
B-3	(a) Cross-sectional image of the electric field magnitude $ \vec{E} ^2$ for a dipole radiating along the surface of a strip waveguide. The blue solid line indicates the position of power flux monitors measuring the amount of radiation into the far-field. The green and red solid lines denote locations of power flux monitors that measure the radiation that couples back into the forward and backwards propagating waveguide mode. Simulation resolution shown above and in all calculations is 32 pixels/ μm . (b) Cross-sectional image in the $\hat{x} - \hat{y}$ plane for both strip (left) and slot (right) structure waveguides with $ \vec{E} ^2$ shown in red. For each FDTD simulation, a line of current sources are placed at each inequivalent sidewall position (only one for each strip waveguide geometry and two for each slot waveguide geometry), with the appropriate complex amplitude retrieved from the waveguide mode's electric field strength at each point.	140
C-1	CAD rendering of the wafer-scale automated wafer prober.	148
C-2	Photograph images of the measurement system with a wafer loaded and one of the fiber arrays lowered above the wafer for measurement.	148
C-3	Schematic overview of the photonics DAQ system.	152
C-4	Top-down CAD rendering (a) and photograph image (b) of the photonics DAQ assembly with PCB, mechanical enclosure, cables, and connectors. Front panel CAD rendering (c) and photograph image (d) of the module, showing the 16 FC/PC connectorized InGaAs detectors and electrical connectors for biasing up to 32 phase modulators.	152

List of Tables

2.1	Spectral reconstruction techniques/methods considered in this work, and the corresponding problem they solve. Depending on the nature of the problem and input vector, various techniques are such as convex optimization and gradient descent are available to solve the problem. The c coefficients for the RBF Network are computed via $c = (AK)^\dagger y$, where K is the kernel matrix $K_{\lambda, \lambda_d} = e^{-\beta \lambda - \lambda_d ^2}$ and λ_d are the centers of the radial basis functions.	54
2.2	Performance comparison of reconstruction methods. R^2 value of reconstruction on sparse spectra consisting of two laser lines at $\lambda = 1552.5$ nm and $\lambda = 1567.5$ nm and broadband spectra (black curve in Fig. 2-4c). For each reconstruction technique, I included the average time to solve the corresponding problem (shown in Table 2.1), the hyperparameter search space, and the dimensionality/size of the hyperparameter space. The results show that the elastic- D_1 algorithm significantly outperforms other techniques for both sparse and broadband input signals.	57
4.1	Silicon Nitride Photonics Process Flow at MIT's Microsystems Technology Laboratory. Assumes student rates (industry rate = $4 \times$ student rate)	80
4.2	Waveguide loss measurements extracted from ring resonators	84

A.1 Comparison of on-chip spectrometers. Side-by-side comparison of the demonstrated 64-channel dFT spectrometer along with previously reported MZI array FTIR, thermo-optic FTIR, arrayed waveguide grating, and random spectrometers. *Values in the “Insertion loss per channel” column account for the power loss per channel in dispersive spectrometers [34,155,160] when measuring broadband inputs and the loss from power-splitting in MZI array Fourier transform spectrometers [78,130,147,182]. †For Fourier transform spectrometers with continuously tunable arms, we define the effective spectral channel count as the bandwidth divided by the minimum spectral resolution. . . . 127

Chapter 1

Introduction

The truth is, most of us discover where we are heading when we arrive.

Bill Watterson

1.1 Background

Integrated photonics is a subfield of optics that focuses specifically on the design and fabrication of photonic integrated circuits (PICs), or devices that guide and manipulate light on semiconductor substrates such as silicon or indium phosphide. This area of study is particularly fascinating for several reasons. First, it builds upon the vast infrastructure and knowledge developed around integrated electronic circuits. The techniques used to make transistors at the nanometer-scale (10^{-9} meters) for digital and analog circuitry can be re-purposed to build structures that route and manipulate light, rather than electricity. These devices are also sometimes called ‘planar lightwave circuits’ since they guide light in waveguides (long rectangular blocks) along the surface of a semiconductor chip in small, tightly confined optical modes (allowed electromagnetic field distributions that satisfy Maxwell’s equations). These circuits require extra care to design, as they obey Maxwell’s equations, and many assumptions that the electronics community may take for granted do not apply when designing photonic circuits. As an example, sharp 90 degree corners in metal traces are acceptable for low-frequency electronics, but at higher electromagnetic frequencies rounded

bends must be used. There are many attractive reasons to integrate optical devices in silicon or other III/V semiconductor substrates: 1) compact devices with small (< 100 nm) features can be made with state-of-the-art lithography tools developed by the electronics industry, 2) the cost of chips decreases significantly if high-volumes are needed (also a byproduct of reusing tools for electronics), 3) many components (tens of thousands) can be made at once and physically ‘connected’ simultaneously by waveguides, and 4) unique semiconductor material properties can be leveraged for the modulation of light, generation of light, and detection of light. Historically, the vast majority of research and development in integrated photonics has centered on applications in data transportation [35,53,54,146,178]. As communication traffic has increased with telephones, computers, and the internet, copper cables (which experience significant losses at high-frequencies) have been almost completely replaced by optical fibers that shuttle data across the world. An ever increasing appetite for data has pushed optics to shorter and shorter distances.

Although the integrated photonics community has seen tremendous commercial success in the telecommunications space, light has potential spanning far beyond shuttling data in complex modulation formats. By combining fundamental optics with advanced manufacturing enabled by the silicon microelectronics industry, integrated photonics is beginning to revolutionize many fields such as quantum optics [167], microwave photonics [120,151,158], high-performance computing [22], hardware accelerators [166], LIDAR [76,148,174], chemical sensing [45,113,168,173], and spectroscopy. In particular, this thesis will focus almost exclusively on using integrated photonic devices for spectroscopic chemical sensing. Micro-chip sized devices that guide, manipulate, and detect light could be used to probe the composition of matter in the world around us. In the not-so-distant future, such devices might be used to analyze the food we eat before we eat it, detect dangerous gases or hazards in our surroundings, or even make health decisions based on the molecules present in a single exhale.

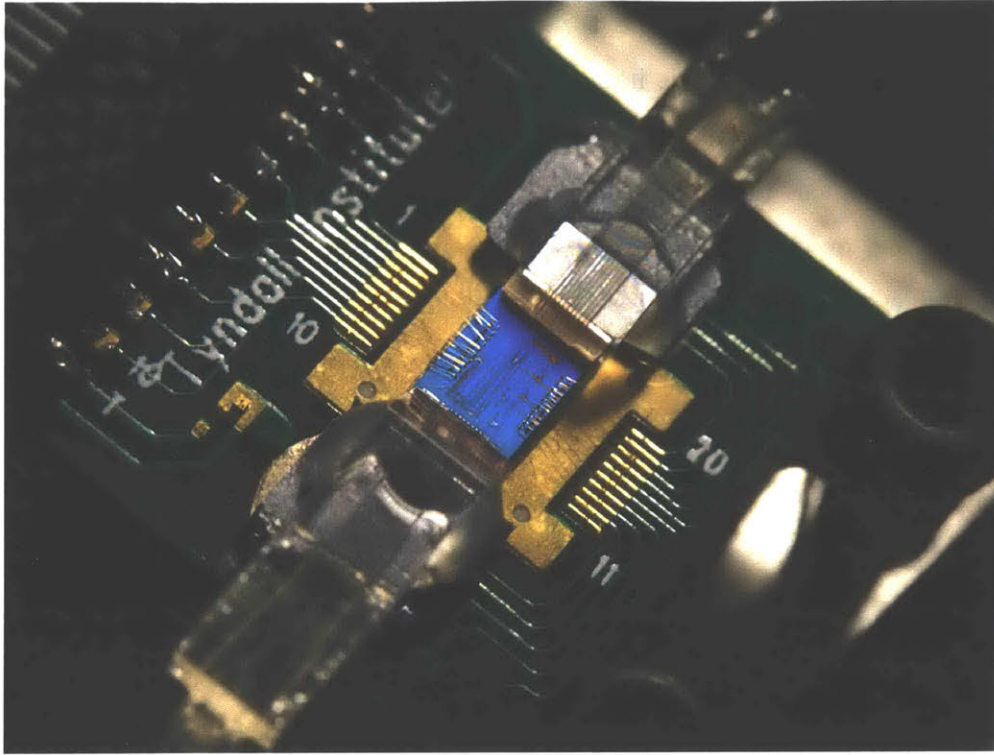


Figure 1-1: Closeup camera image of a 2.5×5.0 mm wide Fourier-transform spectrometer photonic chip with optical fiber connections and metal wirebonds, mounted atop a thermo-electric cooler for temperature control. Information regarding the spectrometer's operating principles is discussed in Chapter 2

1.2 On-chip spectroscopic chemical detection

The term 'spectroscopy' refers to the study of all types of interaction between electromagnetic radiation and physical matter. At the most basic level any spectroscopic sensor consists of three discrete elements: a source for generating light that will interact with the material of interest, a probe or mechanism for getting the light to interact with this matter, and a device for measuring the intensity of this light as a function of wavelength (i.e. a spectrometer). There are a wide variety of light sources, but the most frequently used for sensing applications are continuous-wave laser sources due to their spectral purity, low-cost, high-output powers, and spatial coherence (which is critical for coupling light to single mode dielectric waveguides). Other 'broadband' light sources (which have a distribution of power at many wavelengths of light) such as light-emitting diodes, pulsed lasers, optical frequency combs,

blackbody radiation sources, and super-luminescent diodes are commonly used for sensing, the choice of which is informed by the desired application. Curious readers are referred to a number of textbooks on the subject [36, 38, 161].

The work in this thesis will focus on mechanisms for enhancing light-matter interaction, and on-chip spectrometers for recording the signal of interest. As such, the next few sections are devoted to providing a background on common modes of chemical detection, evanescent-field sensing, and existing on-chip spectrometer implementations.

1.3 Chemical sensing methods

Three mechanisms of sensing will be outlined: absorption spectroscopy, Raman spectroscopy, and refractive index sensing. The following will serve as a brief introduction to the topics, to provide the reader with a sufficient understanding of the sensing mechanisms used in the main text.

1.3.1 Absorption spectroscopy

Absorption spectroscopy refers to the measurement of a material's absorption of light, as a function of wavelength. When you shine light on a material, the power of light absorbed at each wavelength makes up the absorption spectrum and tends to exhibit a series of unique 'dips'. The frequency position of each 'dip' corresponds to energy differences between electron energy levels of the material. The process of light absorption corresponds to the annihilation of one photon in return for the excitation of an electron from a low energy state to a higher energy state. Thus, observing the optical frequencies at which light is absorbed gives us information as to what the electron's energy levels are.

The transition rate for a photon being absorbed by an electron is given by Fermi's golden rule (which is derived using a stationary Hamiltonian perturbed by a time-dependent field):

$$W_{\text{abs}} = \frac{2\pi}{\hbar} |\langle b | H'(r) | a \rangle|^2 \delta(E_b - E_a - \hbar\omega) \quad (1.1)$$

where the middle term (the matrix element) quantifies the coupling between the two energy levels in the presence of the oscillating field. The transition rate R is a more useful quantity, as it describes the transition rate per unit volume of material ($\text{sec}^{-1} \text{cm}^{-3}$) and takes into account the occupation probabilities of the beginning and final states:

$$R = \frac{2}{V} \sum_{k_a} \sum_{k_b} W_{\text{abs}} f_a (1 - f_b) \quad (1.2)$$

where V is the volume, there is a summation over all initial and final states with energy E_a and E_b , f_a describes the occupation probability of state a , and $1 - f_b$ is the probability of state b not being occupied. Practically speaking the rate is integrated over some finite optical bandwidth and so the transition rate is proportional to a density of states and to the square of a transition matrix element. The absorption coefficient α characterizes the fraction of photons absorbed in a material per unit distance (cm^{-1}) and is typically the quantity of interest when performing an absorption spectroscopy experiment:

$$\alpha = \frac{R}{I/\hbar\omega} \quad (1.3)$$

where I is the optical intensity (W/cm^2). It is important to note that the matrix element $|\langle b|H'(r)|a\rangle|^2 = |\langle b|\hat{e} \cdot \vec{p}|a\rangle|^2$ (where \hat{e} is the unit polarization vector and \vec{p} is the electron momentum operator) is a function of the starting wavefunctions ψ_a and ψ_b . Depending on the symmetry properties of ψ_a and ψ_b , some transitions are forbidden (the matrix element is zero) and sets of ‘selection rules’ can be computed to determine allowed versus forbidden transitions. In particular, forbidden transitions include those between two states with the same dipole moment, and molecules with asymmetry tend to have stronger absorption coefficients. Although absorption can occur between various electronic, vibrational, or rotational energy levels, the energy differences between vibrational modes provide unique information about the bonds and structure of a material. For this reason, in the context of absorption spectroscopy the wavelength range from $\lambda = 2.5 - 20 \mu\text{m}$ ($\bar{\nu} = 500 - 4000 \text{cm}^{-1}$) is often referred to as the “fingerprint region”. One of the disadvantages of this technique is that it requires an extremely broadband light source, and all optical components (such as the

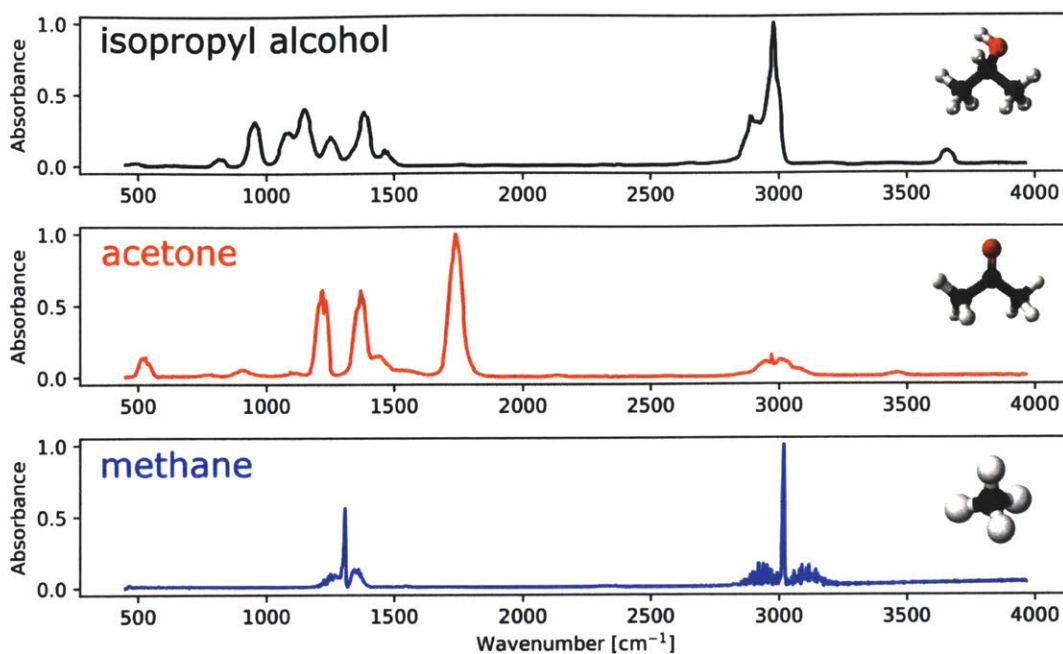


Figure 1-2: Infrared absorption spectra of isopropyl alcohol, acetone, and methane. Data from NIST Chemistry WebBook [183].

spectrometer) must operate across this large wavelength range. This is not a significant issue for free-space optical systems, but in integrated photonics the functional wavelength range is often a small fraction of the whole fingerprint region.

1.3.2 Raman spectroscopy

Raman scattering is an inelastic process by which a photon with energy $E = h\nu_0$ excites a molecule to a higher or lower energy level with energy difference $h\Delta\nu \ll h\nu_0$. The scattered photon is then observed to have a change in frequency $\nu = \nu_0 \pm \Delta\nu$. In Stokes Raman scattering the photon loses energy (red-shifts) and excites the molecule to a higher energy level, while in anti-Stokes Raman scattering the photon gains energy (blue-shifts) and the molecule transitions to a lower energy state. Since this scattering mechanism can only take place between discrete energy levels, the frequency of Raman scattered light provides highly selective information about the molecule under study. A visual depiction of the Raman scattering process is shown in Figure 1-

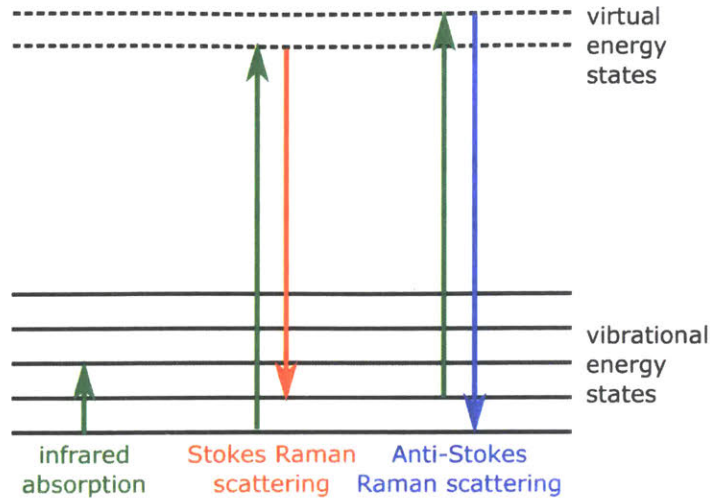


Figure 1-3: Vibrational energy states with depictions of transitions for infrared absorption, Stokes Raman scattering, and Anti-Stokes Raman scattering.

3. The Raman scattering cross section of most materials is very small, such that tens of millions of incident photons are often times required to generate a single Raman scattered photon. However, with high-power wavelength stabilized lasers (most commonly used lasers operate at wavelengths of 532 nm, 765 nm, & 1064 nm) and advances in detector technology (CCDs and CMOS arrays), Raman spectroscopy has become powerful technique for sensitively and selectively detecting various molecules.

When a time-varying electric field E is incident on a molecule, it induces an oscillating dipole with moment p ,

$$p = \alpha E \tag{1.4}$$

where α is the molecular polarizability. In a classical analysis of Raman scattering, the vibration of the molecules can be quantified by the displacement of a molecule about its equilibrium position, Q . The characteristic polarizability of a molecule turns out to be a function of this vibration, and the dependence can be approximated by a Taylor expansion:

$$\alpha = \alpha_0 + \alpha' Q_k \cos(\omega_k t) + O(Q^2) \tag{1.5}$$

where the displacement $Q(t) = Q_k \cos(\omega_k t)$ characterizes the molecular vibration and

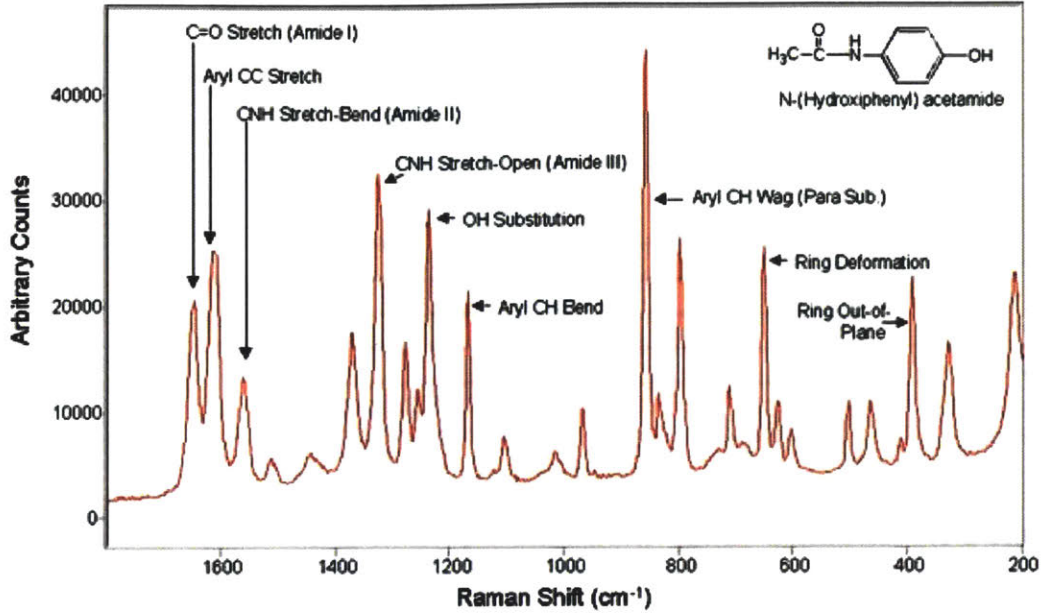


Figure 1-4: Raman spectra of acetaminophen, acquired on a Chromex Sentinel portable Raman system [59].

$\alpha' = \partial\alpha/\partial Q$ is the Raman polarizability tensor. Taking $E = E_0 \cos(\omega_0 t)$, the induced dipole moment p can be expressed as:

$$p = \alpha_0 E_0 \cos(\omega_0 t) + \alpha' E_0 Q_k \cos(\omega_0 t) \cos(\omega_k t) \quad (1.6)$$

$$+ \alpha_0 E_0 \cos(\omega_0 t) + \frac{\alpha' E_0 Q_k}{2} \left[\cos((\omega_0 + \omega_k)t) + \cos((\omega_0 - \omega_k)t) \right] \quad (1.7)$$

$$= p(\omega_0) + p(\omega_0 + \omega_k) + p(\omega_0 - \omega_k). \quad (1.8)$$

In the above equation, the dipole moment with frequency ω_0 corresponds to Rayleigh scattered light, and the terms proportional to $\omega_0 \pm \omega_k$ are the Stokes ($\omega_0 - \omega_k$) and anti-Stokes ($\omega_0 + \omega_k$) Raman scattered light, shown by Figure 1-3.

Similar to infrared absorption, Raman scattering (when given a proper quantum mechanical treatment) also exhibits selection rules depending on the transition polarizability matrix element $\langle \psi_a | \alpha | \psi_b \rangle$. If a transition has a non-zero matrix element, it is considered to be Raman active. As a rule of thumb, many transitions are either

Raman active or infrared (IR) absorption active, but not both. This is referred to as the mutual exclusion principle and as a result both Raman and IR absorption spectroscopy are widely used together to form a more complete picture of a material's characteristic vibrational energy levels.

Finally, it is worth noting that the Stokes and anti-Stokes shifted light in the 'fingerprint region' ($\bar{\nu}_k = 500\text{-}1500 \text{ cm}^{-1}$) exhibit small frequency detunings relative to the incident light at $\bar{\nu}_0$. Since the bandwidth of most planar photonic components is also relatively small (less than an octave), Raman spectroscopy is well suited for photonic integration. For example, with an excitation light source at 808 nm, a photonic chip with an operating bandwidth from $\lambda = 800 - 1200 \text{ nm}$ can collect, route, filter, and analyze Stokes shifted Raman light spanning the entire fingerprint region and up to 4000 cm^{-1} . This will be experimentally demonstrated in Chapter 5.

1.3.3 Refractive index sensing

The last method of chemical sensing to be discussed is refractive index sensing, by which the presence of a known material is determined by changes in the refractive index of some medium. Below, I will quickly review the connection between the refractive index n and the complex material susceptibility χ . This is important because the absorption of a material α , as discussed in Section 1.3.1, is intimately related to the wavelength dependence of the refractive index.

To begin, the electric susceptibility $\chi = \chi' + j\chi''$ is a complex material quantity that relates the polarization density P to an electric field E via $P = \epsilon_0\chi E$ (recall that $D = \epsilon_0 E + P = \epsilon E$, with D the electric displacement and $\epsilon = \epsilon_0(1 + \chi)$ the electric permittivity). By substituting into $k = \omega\sqrt{\epsilon\mu_0}$, we can arrive at an expression for both α the absorption/attenuation coefficient (with units cm^{-1}) and the index n :

$$n - j\frac{1}{2}\frac{\alpha}{k_0} = \sqrt{1 + \chi' + j\chi''}. \quad (1.9)$$

It is important to note that there exists an analytical relationship between the real

and imaginary susceptibility components as a result of the Kramers-Kronig relations:

$$\chi'(\nu) = \frac{2}{\pi} \int_0^{\infty} \frac{s\chi''(s)}{s^2 - \nu^2} ds \quad (1.10)$$

$$\chi''(\nu) = \frac{2}{\pi} \int_0^{\infty} \frac{\nu\chi'(s)}{\nu^2 - s^2} ds. \quad (1.11)$$

As a consequence, the wavelength dependent absorption (which is related to the vibrational energy levels of the medium) is fundamentally related to the refractive index via χ . For frequencies far from any resonances (i.e. optically transparent materials), the Sellmeier equation is commonly used to describe the refractive index of a material with multiple resonances:

$$n^2 - 1 = \sum_i \chi_{0,i} \frac{\nu_i^2}{\nu_i^2 - \nu^2} \quad (1.12)$$

where $\chi_{0,i}$ and ν_i are extracted from measured data. In practice, refractive index sensing is typically not performed over a wide range of wavelengths. Rather, a sensor is designed to detect a change in optical power when a change in the refractive index is observed. Although this technique lacks the specificity of Raman and IR absorption spectroscopy as information about the vibrational translations is not considered, it can be implemented to create very sensitive detectors in situations where only such specificity is not required. As an example, if a container is known to contain only liquid A and liquid B, and by default liquid A is present, then a refractive index measurement of $n = fn_A + (1 - f)n_B$ can be used to very accurately determine the fraction f .

Refractive index changes impart only a phase delay to the incident electric field rather than an amplitude change, and so this quantity is typically determined from interferometric measurements. As an example, if light is split into two modes and only one of these modes interacts with the analyte with index $n + \Delta n$, then interference between these two modes produces a measurable intensity on a photodetector:

$$I = |E_1|^2 + |E_2|^2 + (E_1^*E_2 + E_1E_2^*) \cos(\phi_1 - \phi_2) \quad (1.13)$$

where $I = |E|^2$ and each mode has electric field $E_i e^{j\phi_i}$. Thus, there is a clear cosine dependence on the transmitted signal for phase delays given by $\Delta\phi = \frac{2\pi}{\lambda} \Delta n L$. Analyses of several chemical sensing methods such as Mach-Zehnder refractometry and ring resonator refractometry are provided in Appendix B.1.

1.4 Evanescent-field waveguide sensing

Having reviewed three common chemical sensing schemes, we can now consider how to make an integrated photonic device that can let light interact with nearby chemicals. Typical spectroscopic sensors involve free-space optics and focus light onto a sample of interest. In single-mode integrated photonic devices, light is already propagating within a small dielectric slab of material and the distribution of the electric and magnetic field is on the order of half the wavelength of light. To confine and guide light, the core material n_{core} must be greater than the index of the cladding on the top and bottom. For practical waveguide geometries with asymmetric top and bottom clad, these electromagnetic modes are easily solved for with numerical methods. In the clad, the cross-sectional field distribution decays exponentially with distance from the core (since the effective index of the guided mode must be greater than the index of the clad). In evanescent-field sensing, it is this portion of the electric field that is allowed to interact with a chemical of interest and produce some signal that correlates to the presence or absence of some molecules. In evanescent-field refractive index sensing, we will measure just the change in the effective index of the waveguide mode n_{eff} for some index change in the cladding. Since only part of the light interacts with the analyte (the rest is confined in the core or bottom cladding) the change in the two indices are not equal ($\Delta n_{\text{eff}} \neq \Delta n_{\text{clad}}$). The external confinement factor Γ_{clad} is a quantity that is used to measure how sensitive a waveguide is to changes in analyte with respect to a free-space beam:

$$\Gamma_{\text{clad}} = \frac{dn_{\text{eff}}}{n_{\text{clad}}} = \frac{n_g}{n_{\text{clad}}} \frac{\int_{\text{clad}} \epsilon |\vec{E}|^2 d^2x}{\int \epsilon |\vec{E}|^2 d^2x}. \quad (1.14)$$

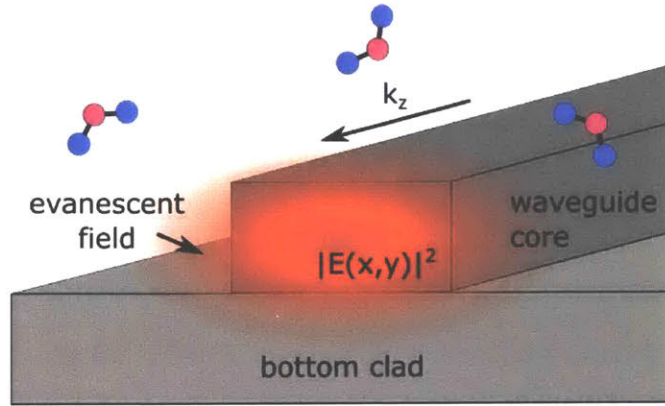


Figure 1-5: Schematic of a simple dielectric waveguide with exposed top cladding for evanescent-field sensing. Light travels in the out-of-plane direction, and the evanescent portion of the electric field interacts with nearby chemicals to generate a measurable signal.

This quantity can be calculated by either integrating over the fields produced from a simple eigenmode calculation, or by computing the change in effective index from a small perturbation to the cladding index. Γ_{clad} from Equation 1.14 is also used to determine the sensitivity of a waveguide when used for evanescent-field absorption spectroscopy. This quantity is useful when deciding upon an optimal waveguide geometry, as it is desirable to have a significant portion of the electric field overlapping with the analyte.

For evanescent-field Raman spectroscopy (also called “waveguide-enhanced Raman spectroscopy”, or WERS), the evanescent field of laser light propagating in the waveguide scatters with analyte in the cladding. The portion of this Raman scattered light that couples back into the waveguide is routed to a spectrometer for analysis. In this case, a large overlap of the electric field with the analyte is desirable both for enhancing the amplitude of the induced Raman dipole moment and also for enhancing the coupling efficiency of this light into the waveguide mode of interest. In Chapter 5, the Raman gain coefficient for evanescent waveguide sensing is presented (and derived in Appendix B.2) and is shown to have a fourth-power dependence on the electric field. Thus, large sensitivity enhancements are possible for gap-structures that have large electric field amplitudes in the sensing region.

1.5 On-chip spectroscopy

After light interacts with the molecule of interest, a spectrometer is often required to measure the intensity of light at each wavelength. This section will attempt to provide a brief overview of various on-chip spectrometers and their operating principles. The spectrometers are roughly grouped into two categories: grating spectrometers and Fourier-transform spectrometers. In grating spectrometers, light is split into N channels, one for each unique wavelength band, using some type of dispersive element such as a prism or grating. Fourier transform spectrometers, on the other hand, split light in two paths with two different optical path lengths L_1 and $L_1 + \Delta L(t)$, recombine the two signals, and collect the light on a single photodetector. As will be shown, the intensity of light on the single photodetector is a function of the path length difference $\tilde{I}(\Delta L)$ is an inverse Fourier transform of the input spectrum $I(\bar{\nu})$ (where $\bar{\nu}$ is the wavenumber $1/\lambda$).

1.5.1 Echelle gratings

An ideal grating spectrometer takes an input signal $I(\lambda)$ and passively splits this into N channels each containing only a subset of the input frequency components. The transfer function from the input to one of the output channels should look like a rectangular pass-band with a flat transmission and a sharp roll-off at the edge of this pass-band with high-extinction (zero cross-talk). One method of achieving this is by designing an Echelle grating spectrometer, sometimes known as a planar concave grating. This device consists of a waveguide incident on a wide slab region where light diffracts in-plane, scatters off of many periodic grating teeth with period Λ , and then refocuses onto a set of N waveguides as shown in Figure 1-6. The angle between the incident diffracted beam and the normal to the sidewall is given by θ_i , and the angle of the reflected light (from the sidewall normal) θ_q at which constructive interference occurs is given by the grating equation:

$$n_{\text{eff, slab}} \sin(\theta_q) = n_{\text{eff, slab}} \sin(\theta_i) + q \frac{\lambda}{\Lambda} \quad (1.15)$$

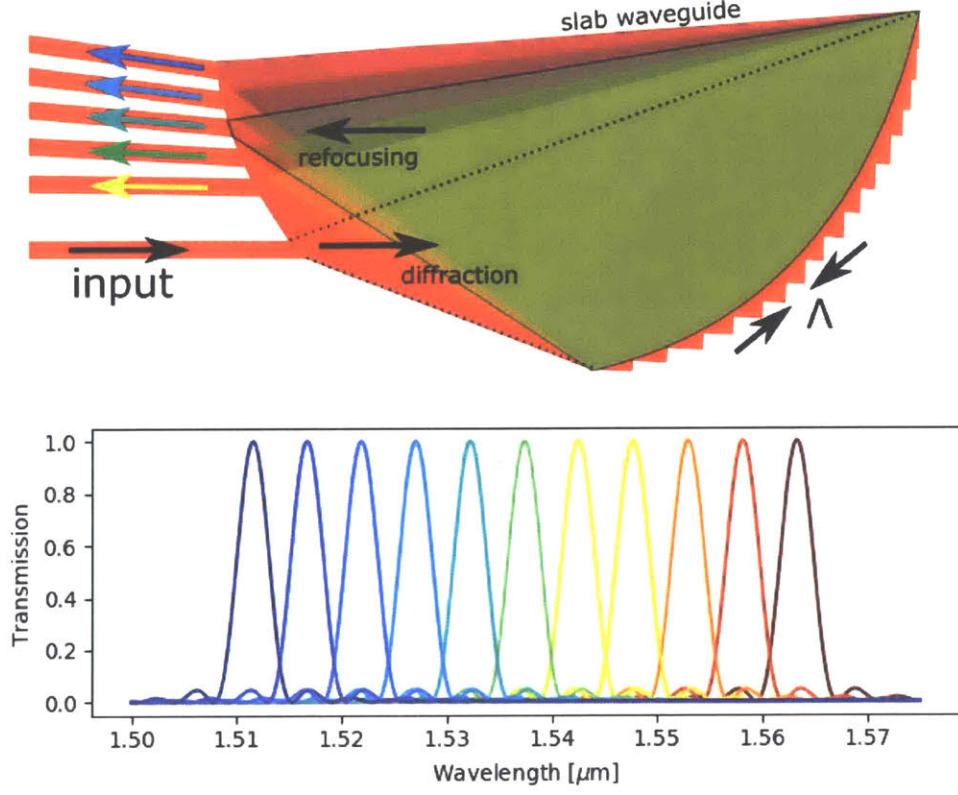


Figure 1-6: Schematic of an Echelle grating spectrometer with $N = 5$ outputs (not to scale), and below is a sample output spectrum for a device with $N = 11$ outputs, the response of which is given by Equation 1.17.

where the diffraction order q is an integer. This expression is derived by considering conditions for constructive interference between light scattered at all places along the grating. Compared to the free-space grating equation, we must consider the optical path length in a slab structure which is determined by the effective waveguide index $n_{\text{eff, slab}}$. An important quantity is the free-spectral range (FSR) λ_{FSR} or $\nu_{\text{FSR}} \simeq \frac{c_0 \lambda_{\text{FSR}}}{\lambda^2}$, which determines the change in wavelength or frequency required to make an adjacent diffraction order scatter into the same port (same angle θ_q). Since the effective index n_{eff} is a function of wavelength, we can expand it to first-order via $n_{\text{eff}}(\lambda + \lambda_{\text{FSR}}) = n_{\text{eff}}(\lambda) + \lambda_{\text{FSR}} \frac{dn_{\text{eff}}}{d\lambda}$, which simplifies Equation 1.15:

$$n_g \frac{\nu_{\text{FSR}}}{c_0} \Lambda (\sin(\theta_i) - \sin(\theta_q)) = 1 \quad (1.16)$$

where the group index $n_g = n_{\text{eff}} - \lambda_0 \frac{dn_{\text{eff}}}{d\lambda_0}$ is a geometry- and material-dependent term that characterizes the wavelength dependence of the effective index to first-order. While the FSR sets the maximum bandwidth of the spectrometer, the channel bandwidth $\delta\nu$ determines the spectrometer's channel width. This can be analyzed by considering the interference intensity of M waves scattering from M grating teeth, each with a fixed phase difference $\phi = 2\pi n_{\text{eff}} \Delta l / \lambda$ with $\Delta l = \Lambda(\sin(\theta_i) + \sin(\theta_f))$:

$$I = I_0 \frac{\sin^2(M\phi/2)}{\sin^2(\phi/2)} = I_0 \frac{\sin^2(M \frac{\pi}{\lambda} n_{\text{eff}}(\lambda) \Delta l)}{\sin^2(\frac{\pi}{\lambda} n_{\text{eff}}(\lambda) \Delta l)} \quad (1.17)$$

and in the above, the first null occurs when $\phi = 2\pi/M$. From this, the channel width of the grating spectrometer can be derived:

$$\delta\nu = 2c_0 / (M n_g \Lambda(\sin \theta_i + \sin \theta_f)). \quad (1.18)$$

From these relationships between the system parameters, it is important to note that the channel width (spectral resolution) scales inversely with the *size of the spectrometer*, which is related to the number of grating teeth M .

1.5.2 Arrayed waveguide gratings

Arrayed waveguide gratings are functionally similar to reflection-based grating spectrometers (Echelle gratings) in that they decompose an input with many frequency components to N output channels each containing only a narrow frequency band of the input signal. These devices consist of a set of dispersive optical delay lines (waveguides with varying lengths), as shown by the schematic in Figure 1-7, connected by star couplers on the input and output. The first star-coupler splits light evenly amongst the M optical delay lines, which then wrap around to a second star coupler where the M beams combine and interfere in such a way that light within a specific frequency band will only couple to one output.

The derivation for the response of an arrayed waveguide grating is similar to that

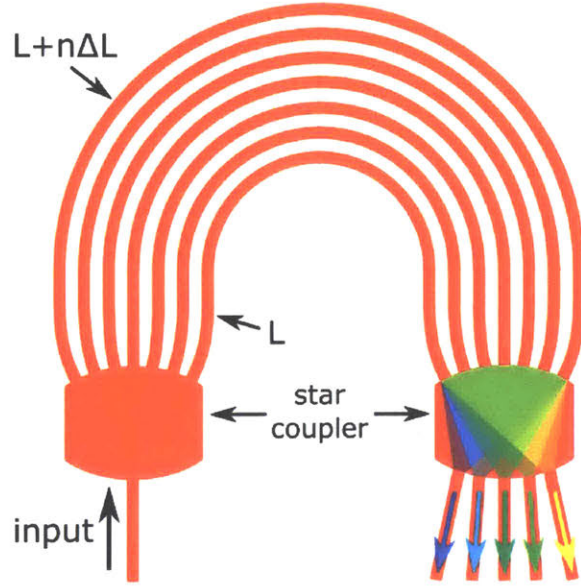


Figure 1-7: Schematic of an arrayed waveguide grating (AWG) with $M = 7$ optical delay lines and $N = 5$ outputs (not to scale).

for Echelle gratings, and the condition for constructive interference at the output is:

$$n_{\text{eff,slab}}d_a + n_{\text{eff, wg}}\Delta L - n_{\text{eff, slab}}d_a = q\lambda \quad (1.19)$$

where $n_{\text{eff, slab}}$ is the effective index of the slab mode in the star coupler, d_a is the length from input to output for each star coupler, $n_{\text{eff, wg}}$ is the effective index of the waveguide delay lines, and ΔL is the length difference between two adjacent waveguides in the array [140]. Similar to the Echelle grating, the arrayed waveguide grating transmission has a periodic frequency response, and this period is given by the FSR:

$$n_g \frac{\nu_{\text{FSR}}}{c_0} \Delta L = 1. \quad (1.20)$$

The output of the final star coupler behaves similar to an optical phased array, and the channel spacing can be determined from a multipath interference equation similar to that of Equation 1.17. The spectral resolution of the device (which determines the number of non-overlapping channels that can fit within the FSR) is ultimately determined by the number of dispersive waveguides.

Both Echelle gratings and arrayed waveguide gratings have found widespread use for wavelength division multiplexing (WDM) and demultiplexing. However, chemical sensing applications often have specific requirements in total channel count, the minimum wavelength resolution, and the sensitivity of the measurement. The wavelength resolution scales inversely with the size of the device for Echelle gratings and arrayed waveguide gratings, which makes such spectrometers large for applications that demand high-resolution, such as optical coherence tomography [55]. For applications that require analysis of broadband light sources, such as absorption spectroscopy, the minimum sensitivity and limit of detection are related to the wavelength resolution, since the optical power is divided amongst the N spectral channels. In low-light applications where the optical throughput is critical, time-domain modulation techniques like Fourier-transform spectroscopy allow for measurement signals that do not adversely scale with the wavelength resolution.

1.5.3 Fourier transform spectrometers

Another technique for measuring the optical spectrum of an arbitrary input light source is by using a two-arm interferometer such as a free-space Michelson interferometer or an on-chip Mach-Zehnder interferometer, as shown in Figure 1-8. The intensity of light after recombining at the output is a function of $\Delta\phi$, the difference in phase accumulated by light in the two interferometer arms:

$$I(z) = I(\bar{\nu}) \cos\left(\frac{\Delta\phi}{2}\right)^2 = 0.5I(\bar{\nu}) \left[\cos(2\pi n_{\text{eff}}\bar{\nu}z) + 1 \right] \quad (1.21)$$

where $\bar{\nu} = 1/\lambda$ and Equation 1.21 assumes a monochromatic input light source. Typically the DC component is ignored and the ‘interferogram’ consists of the AC component as a function of the optical path length difference $\delta = n_{\text{eff}}z$:

$$I(\delta) = 0.5I(\bar{\nu}) \cos(2\pi\bar{\nu}\delta). \quad (1.22)$$

In practice, a single instrument-dependent prefactor $B(\bar{\nu})$ is used to characterize the

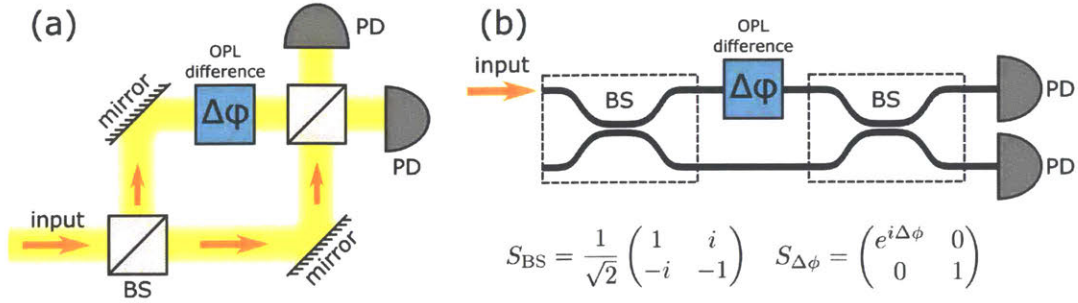


Figure 1-8: (a) Schematic of a free-space Mach-Zehnder interferometer with phase delay $\Delta\phi$ between the two interferometer arms, made up of two beam splitters (BS), two mirrors, and two photodetectors (PD). (b) Waveguide integrated Mach-Zehnder interferometer, comprising of two 50:50 power couplers, a phase tuning element, and two output photodetectors. At bottom are the scattering matrices of the beamsplitter and phase delay elements.

frequency-dependent response of the detector, the amplifier, and the beam-splitter non-uniformity [68]. Given a continuum of frequency components, the relationship between $B(\bar{\nu})$ (from which the input signal can be readily derived) and the interferogram signal from the amplifier $S(\delta)$ is a cosine Fourier transform:

$$S(\delta) = \int_{-\infty}^{\infty} B(\bar{\nu}) \cos(2\pi\bar{\nu}\delta) d\bar{\nu} \quad (1.23)$$

$$B(\bar{\nu}) = \int_{-\infty}^{\infty} S(\delta) \cos(2\pi\bar{\nu}\delta) d\delta = 2 \int_0^{\infty} S(\delta) \cos(2\pi\bar{\nu}\delta) d\delta. \quad (1.24)$$

$$(1.25)$$

Since the recorded interferogram and the input signal are related via Fourier-transforms, the total bandwidth $\Delta\bar{\nu}$ is related to the *minimum* incremental optical path length difference $n_g\delta L$ and the minimum spectral resolution $\delta\bar{\nu}$ is inversely related to the *largest* optical path length difference $n_g\Delta L$:

$$\Delta\bar{\nu} = \frac{1}{n_g\delta L} \quad (1.26)$$

$$\delta\bar{\nu} = \frac{1}{n_g\Delta L} \quad (1.27)$$

and similarly in terms of wavelength bandwidth $\Delta\lambda$ and resolution $\delta\lambda$:

$$\Delta\lambda = \frac{\lambda^2}{n_g\delta L + \lambda} \quad (1.28)$$

$$\delta\lambda = \frac{\lambda^2}{n_g\Delta L + \lambda} \approx \frac{\lambda^2}{n_g\Delta L} \quad (1.29)$$

where it is assumed the maximum path length difference is much greater than the optical wavelength $n_g\Delta L \gg \lambda$. From Equations 1.26 and 1.27, it is clear that the spectral performance of the Fourier transform spectrometer is determined by the minimum achievable path length difference steps between the two arms and the maximum path length difference. In order to achieve narrow spectral resolutions, it is important to consider tuning mechanisms that maximize the phase without unreasonable performance penalties in terms of loss, size, or power consumption.

Free-space Fourier transform spectrometers offer a signal-to-noise ratio (SNR) advantage over grating based spectrometers. This arises because all wavelengths of light are collected on a single photodetector rather than split among N channels. As a result, the total intensity at the detector is enhanced by a factor of N . If the dominant source of noise is from the photodetector, then the noise level is given by $\text{NEP}/t^{1/2}$ [W/ $\sqrt{\text{Hz}}$] where NEP is the noise-equivalent power of the photodetector and t is the total measurement time. Since Fourier transform spectroscopy is a time-domain measurement technique, all N interferometer lengths must be sequentially measured and so $t_{\text{grating}} = Nt_{\text{FT}}$. Thus, the signal-to-noise ratio is enhanced by a factor of \sqrt{N} , which is often called the multiplex advantage, or ‘Fellgett’s Advantage’:

$$\text{SNR} = \frac{\text{signal}}{\text{noise}} = NI_{\text{grating}} \frac{\sqrt{t_{\text{grating}}/N}}{\text{NEP}} = \sqrt{N}\text{SNR}_{\text{grating}}. \quad (1.30)$$

It’s worth noting that when the signal itself becomes the dominant source of noise (such as in shot-noise-limited measurements), the noise level becomes proportional to \sqrt{N} and the multiplex advantage is canceled.

For on-chip sensing applications, Fourier-transform spectroscopy can offer unique advantages in SNR as well as spectral resolution if large optical path length modula-

tion can be achieved.

1.6 Thesis overview

The following chapters of this thesis will describe my contributions to the fields of integrated photonic chemical sensing and integrated spectrometers. Chapter 2 describes a new technique for performing on-chip Fourier transform spectroscopy with a dynamically reconfigurable Mach-Zehnder interferometer. The method is theoretically analyzed and a system prototype, fabricated on a mature active silicon photonics process, is demonstrated. Chapter 3 analyzes the evanescent-field sensing performance of dielectric optical waveguides when sidewall-induced roughness scattering is the dominant loss mechanism. This work is motivated by recent interest in slot and sub-wavelength grating waveguides with higher external confinement factors than traditional strip waveguides. Since these structures inevitably have larger scattering loss (due to high field magnitudes at waveguide interfaces), I derive appropriate sensing figures of merit and develop a quantitative method for computing the scattering loss. In Chapter 4 I discuss a quick-turn high-performance process that I developed for making silicon nitride integrated photonic circuits with heaters. These low-loss (0.36 ± 0.11 dB/cm) devices can be manufactured in just 16 days, cost under 1 \$/mm², and feature etched edge couplers, exposed sensing windows, and thermal phase tuners. Chapter 5 describes a successful demonstration of a robust, fiber-packaged waveguide-enhanced Raman sensor which is used to detect mixtures of organic solvents. Finally, Chapter 6 discusses future directions of research that could build upon and improve on-chip spectrometer demonstrations and packaged waveguide enhanced Raman chemical sensors. Appendices A and B provide necessary derivations and analyses to support the work presented in Chapters 2 and 3. Appendix C.1 introduces PICwriter, an open-source python library I developed to streamline the process of designing complex GDSII masks for integrated photonics (which I used extensively for device design). Appendix C.2 provides details of an automated wafer probing system that was developed to test and measure passive in-

tegrated photonic devices. Finally, Appendix C.3 provides details of a photonic data acquisition system I designed to control up to 32 integrated phase tuners and measure optical signals from up to 16 optical channels.

The work that follows in this thesis has resulted in contributions to the following journal publications:

- Z. Han, V. Singh, **D. M. Kita**, C. Monmeyran, P. Becla, P. Su, J. Li, X. Huang, L. C. Kimerling, J. Hu, K. Richardson, D. T. H. Tan, A. Agarwal “*On-chip chalcogenide glass waveguide-integrated mid-infrared PbTe detectors,*” Applied Physics Letters 109, 071111 (2016).
- Q. Du, Y. Huang, J. Li, **D. M. Kita**, J. Michon, H. Lin, L. Li, S. Novak, K. Richardson, W. Zhang, J. Hu, “*Low-loss photonic device in Ge-Sb-S chalcogenide glass,*” Optics Letters 41, 3090-3093 (2016).
- **D. M. Kita**, H. Lin, A. Agarwal, K. Richardson, I. Luzinov, T. Gu, J. Hu “*On-Chip Infrared Spectroscopic Sensing: Redefining the Benefits of Scaling,*” in IEEE Journal of Selected Topics in Quantum Electronics, vol. 23, no. 2, pp. 340-349, March-April (2017).
- H. Lin, Y. Song, Y. Huang, **D. M. Kita**, S. Deckoff-Jones, K. Wang, L. Li, J. Li, H. Zheng, Z. Luo, H. Wang, S. Novak, A. Yadav, C. Huang, R. Shiue, D. Englund, T. Gu, D. Hewak, K. Richardson, J. Kong, J. Hu “*Chalcogenide glass-on-graphene photonics,*” Nature Photonics 11, 798-805 (2017).
- **D. M. Kita**, B. Miranda, D. Favela, D. Bono, J. Michon, H. Lin, T. Gu, J. Hu “*High-performance and scalable on-chip digital Fourier transform spectroscopy,*” Nature Communications 9, 4405 (2018).
- **D. M. Kita**, J. Michon, S. G. Johnson, and J. Hu, “*Are slot and sub-wavelength grating waveguides better than strip waveguides for sensing?,*” Optica 5, 1046-1054 (2018).

- P. Su, Z. Han, **D. M. Kita**, P. Becla, H. Lin, S. Deckoff-Jones, K. Richardson, L. C. Kimerling, J. Hu, A. Agarwal, “*Monolithic on-chip mid-IR methane gas sensor with waveguide-integrated detector*,” Applied Physics Letters 114, 051103 (2019).
- **D. M. Kita**, J. Scholvin, C. Rios, J. Hu, “*A Quick-Turn Fabrication Process for Si_3N_4 Integrated Circuits with Heaters*,” (2019) (*in review*).
- **D. M. Kita**, J. Michon, J. Hu, “*A fully packaged, fiber-coupled waveguide-enhanced Raman spectroscopic sensor*,” (2019) (*in review*).

Chapter 2

A reconfigurable waveguide integrated Fourier-transform spectrometer^{*}

Overview

On-chip spectrometers have the potential to offer dramatic size, weight, and power advantages over conventional benchtop instruments for many applications such as spectroscopic sensing, optical network performance monitoring, hyperspectral imaging, and radio-frequency spectrum analysis. Existing on-chip spectrometer designs, however, are limited in spectral channel count and signal-to-noise ratio. This chapter presents an experimental demonstration of an on-chip digital Fourier transform spectrometer that acquires high-resolution spectra via time-domain modulation of a reconfigurable Mach-Zehnder interferometer. The device, fabricated and packaged using industry-standard silicon photonics technology, claims the multiplex advantage to dramatically boost the signal-to-noise ratio and unprecedented scalability capable of addressing exponentially increasing numbers of spectral channels. Relevant machine learning regularization techniques are explored and applied to spectrum reconstruction. Using a new ‘elastic- D_1 ’ regularized regression method, significant noise suppression is achieved for both broad (> 600 GHz) and narrow (< 25 GHz) spectral features, as well as spectral resolution enhancement beyond the classical Rayleigh criterion.

2.1 Introduction

Optical spectrometers are extensively applied to sensing, materials analysis, and optical network monitoring. Conventional spectrometers are bulky instruments often involving mechanical moving parts, which severely compromises their deployment versatility and increases cost. Photonic integration offers a solution to miniatur-

^{*}This chapter is based on: D. M. Kita, B. Miranda, D. Favela, D. Bono, J. Michon, H. Lin, T. Gu, J. Hu, “High-performance and scalable on-chip digital Fourier transform spectroscopy” *Nature Communications* 9, 4405 (2018).

ize spectrometers into a chip-scale platform, albeit often at the cost of performance and scalability. Existing on-chip spectrometers mostly rely on dispersive elements such as gratings [26, 34, 100, 118, 126, 160, 173], holograms [12, 29], and microresonators [65, 110, 196]. These devices suffer serious signal-to-noise ratio (SNR) penalties when designed for high spectral resolution, as a result of spreading input light over many spectral channels. Moreover, the device footprint and complexity scale linearly with the spectral channel number N , as each channel requires an individually addressed receiver (photodetector) and the spectral resolution is inversely proportional to the optical path length (OPL). The SNR degradation and linear scaling behavior preclude high-performance on-chip spectrometers with channel counts rivaling their benchtop counterparts, which typically have hundreds to thousands of spectral channels. These constraints also apply to spectrometers based on the wavelength multiplexing principle, where each receiver captures an ensemble of monochromatic light rather than one single wavelength [25, 102, 130, 145, 154, 155, 182] (for multiple-scattering-based spectrometers, the device dimension scales with spectral resolution quadratically).

Unlike dispersive spectrometers, Fourier transform infrared (FTIR) spectrometers overcome the trade-off between SNR and spectral resolution benefiting from the multiplex advantage, also known as the Fellgett's advantage [75]. Traditional benchtop FTIR spectrometers use moving mirrors to generate a tunable OPL, a design not readily amenable to planar photonic integration. On-chip FTIR spectrometers instead rely on thermo-optic or electro-optic modulation to change the OPL in a waveguide [33, 108, 172, 204]. The miniscule refractive index modifications produced by these effects, however, result in a large device footprint and constrain the practically attainable spectral resolution to tens of cm^{-1} in wave number, far inferior compared to their benchtop counterparts. Furthermore, prior work has demonstrated Fourier-transform spectrometers using arrays of discrete Mach-Zehnder interferometers (MZIs) [78, 130, 147, 182], although these approaches are not practical for large spectral channel counts (due to excessive chip footprints). The compressive sensing methods proposed and demonstrated for reconstructing optical spectra using the lim-

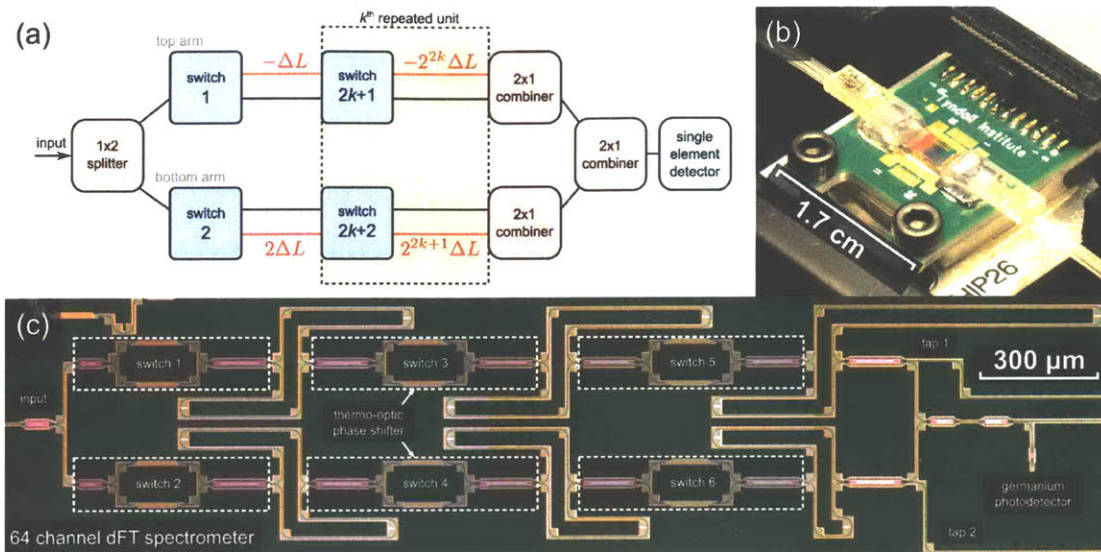


Figure 2-1: (a) Block diagram illustrating the generic structure of a dFT spectrometer with j switches and $K = j/2 - 1$ repeated stages indexed by $k \in [1, K]$; (b) photo of the fully-packaged, plug-and-play dFT spectrometer with standard FC/PC fiber interface and a ribbon cable for control and signal read-out; (c) top-view optical micrograph of the 64-channel dFT spectrometer after front-end-of-line silicon fabrication, showing the interferometer layout, the thermo-optic switches and waveguide-integrated germanium photodetector.

ited measurements from these MZI arrays are also only practical for sparse spectra such as laser lines (as shown in later sections). Prior theoretical work has suggested optical switches can be used to physically alter interferometer arm lengths [7], but these embodiments would all suffer in practice from poor scaling laws, as the number of spectral channels is equal to the number of switches and photodetectors.

In the following, a novel digital Fourier transform (dFT) spectrometer architecture that resolves the performance and scalability challenges of these prior approaches is proposed and experimentally realized. This device consists of a Mach-Zehnder interferometer with optical switches on each arm that direct light to waveguides of different path lengths. This approach claims three key advantages over state-of-the-art. First, both the spectral channel count and resolution scale exponentially with the number of cascaded switch stages. This unique exponential scaling behavior allows high-resolution spectroscopy with a radically simplified device architecture. Second, direct modification of the waveguide path offers over 2 orders of magnitude larger OPL

modulation per unit waveguide length compared to thermo-optic or electro-optic-based index modulation (see Appendix A.3 for further details), enabling superior spectral resolution within a compact device. Third, the device benefits from the multiplex advantage to ensure significantly enhanced SNR over the dispersive devices. Moreover, the spectrometer only requires a single-element photodetector rather than a linear array, which further reduces system complexity and cost.

2.2 dFT Architecture and Scaling Laws

The centerpiece of the dFT spectrometer is a reconfigurable Mach-Zehnder interferometer (MZI) illustrated in Fig 2-1a. Each arm consists of $j/2$ cascaded sets of optical switches connected by waveguides of varying lengths, where j is an even integer. When light propagates through the reference paths (marked with black color) in both MZI arms, the MZI is balanced with zero OPL difference between the two arms. Lengths of the waveguide paths in red differ from the reference paths by powers of two times ΔL . Each permutation of the switches thus corresponds to a unique OPL difference between the arms, covering 0 to $(2^j - 1)n_g\Delta L$ with a step size of $n_g \cdot \Delta L$, where n_g represents the waveguide group index. Unlike traditional FTIR spectrometers where the OPL is continuously tuned, resembling an analog signal, this dFT spectrometer derives its name from the set of “digitized” binary optical switches, with the state of each corresponding to a unique permutation of the spectrometer and a unique OPL difference. The number of spectral channels, defined by the distinctive optical states the device furnishes, is:

$$N = 2^j \tag{2.1}$$

and the spectral resolution is given following the Rayleigh criterion [68, 94, 113]:

$$\delta\lambda = \frac{\lambda^2}{(2^j - 1) \cdot n_g\Delta L} \approx \frac{1}{2^j} \cdot \frac{\lambda^2}{n_g\Delta L} \tag{2.2}$$

where δ denotes the center wavelength.

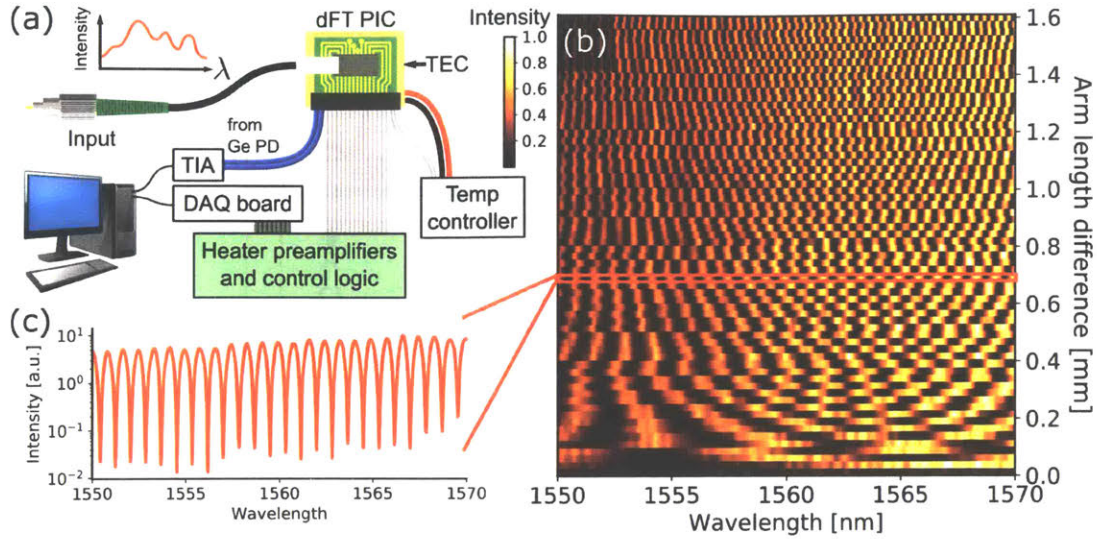


Figure 2-2: Packaged dFT photonic integrated circuit (PIC) and spectral basis set. (a) Schematic diagram of the dFT spectrometer characterization setup; (b) an exemplary transmission spectrum of the dFT device corresponding to an arm length difference of 0.7 mm; (c) transmission spectra of the device for all 64 permutations of the switch on/off combinations: the ensemble of 64 spectra constitute the basis set for spectrum reconstruction.

2.3 Experimental demonstration

The dFT spectrometer concept was experimentally validated by demonstrating a 64-channel device ($j = 6$) operating at the telecommunication C-band. The device was fabricated leveraging a commercial silicon photonics foundry process, where the optical switches employ a custom compact thermo-optic phase shifter design (89.5 μm long, with 33 mW/ π phase shifting efficiency and 30.8 μs 10%-to-90% rise time, both evaluated through my own experimental measurements) [74]. The insertion loss of the spectrometer was found to be 9.1 ± 1.7 dB, with a loss of 1.7 ± 0.4 dB for each switching stage (averaged across the full 20 nm band considered in this text). Figure 2-1b presents a micrograph of the spectrometer after front-end-of-line silicon fabrication. The chip was subsequently packaged with bonded fiber arrays and electrical connections. Details of the fabrication and packaging processes are elaborated in the Methods section. The spectrometer also integrates an on-chip germanium photodetector and a standard FC/PC fiber connector interface, making it a standalone

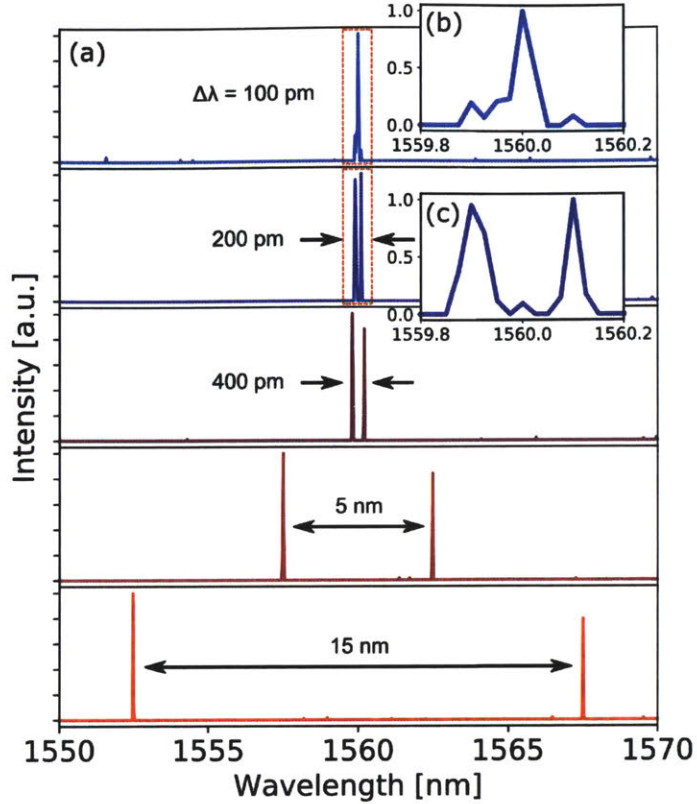


Figure 2-3: Sparse signal reconstruction. (a) Spectra consisting of two laser lines with varying spacing measured using the 64-channel dFT spectrometer and reconstructed by applying the elastic- D_1 algorithm. Insets (b) and (c) show zoomed-in images of the narrow spectral features for input laser lines with 100 pm and 200 pm spacing, respectively.

“plug-and-play” device for optical spectrum analysis (Fig. 2-1c). The spectrometer dissipates 99 mW of power during operation, regardless of the switch state.

The spectrometer was characterized using a setup depicted in Fig. 2-2a. High-resolution transmittance spectra of the device were first recorded by wavelength sweeping a tunable laser between 1550 nm and 1570 nm, for all 64 permutations of the switch on/off combinations. The 64 spectra (which show an average extinction ratio of $21 \pm 3 \text{ dB}$) are plotted in Fig. 2-2c, each associated with a unique OPL difference between the MZI arms. The ensemble of spectra forms an $m \times n$ calibration matrix A . Each row of A represents a transmittance spectrum and contains $n = 801$ elements, the number of wavelength points in the scan. Each column corresponds to

a discretely sampled interferogram of the narrow-band laser and contains $m = 64$ elements. The intensity measured by the detector for an arbitrary input polychromatic signal (represented by a column vector x with 801 elements) is:

$$y = Ax \tag{2.3}$$

where the interferogram y is a column vector with 64 elements, each gives the detector output at a particular switch permutation. The vector y was measured by recording the detector output at all 64 permutation states. Since y was measured with size 64 to infer x with size 801, the system is underconstrained and therefore regularization techniques are required to specify a unique solution.

2.4 Spectrum reconstruction

To determine the correct solution vector, I first explored a number of standard regularized regression and compressive-sensing techniques such as basis pursuit denoising (BPDN), least absolute shrinkage and selection operator (LASSO), and elastic-net – the corresponding metrics they optimize are listed in Table 2.1. For each of these regularized regression methods, a weight (hyperparameter) is applied to the L_1 -norm (and for elastic-net a separate weight for the L_2 -norm) of the spectrum. To determine the appropriate value(s) of the hyperparameter(s) I used a standard holdout cross-validation technique [163], through which I took two consecutive measurements of the interferogram (y_1 and y_2) and choose hyperparameters that maximize the coefficient of determination $R_2(A_2x, y_2)$ (see Appendix A.1), where A_1 and A_2 are two separate measurements of the basis (performed once as a calibration step), and x is the computed spectrum from y_1 and A_1 . I note that the basis measurements A_1 and A_2 do not change significantly over time: in fact, for all results reported in this work the calibration matrices A_1 and A_2 are measured more than two weeks prior to the actual interferogram measurements y_1 and y_2 . The validated device stability is critical to practical applications, as it ensures that the calibration step only need

Method	Problem
Pseudoinverse	$y = Ax$ (Moore-Penrose)
Ridge regression	$\min_x \left\{ \ y - Ax\ _2^2 + \alpha_2 \ x\ _2^2 \right\}$
LASSO	$\min_x \left\{ \ y - Ax\ _2^2 + \alpha_1 \ x\ _1 \right\}$
BPDN	$\min_x \left\{ (1/2) \ y - Ax\ _2^2 + \alpha_1 \ x\ _1 \right\}$
RBF Network	$\min_c \left\{ \ y - Ah_c\ _2^2 \right\}$ with $h_c = Kc = \sum_{d=1}^D c_d e^{-\beta \lambda - \lambda_d ^2}$
Elastic-Net	$\min_{x, x > 0} \left\{ \ y - Ax\ _2^2 + \alpha_1 \ x\ _1 + \alpha_2 \ x\ _2^2 \right\}$
Elastic- D_1	$\min_{x, x > 0} \left\{ \ y - Ax\ _2^2 + \alpha_1 \ x\ _1 + \alpha_2 \ x\ _2^2 + \alpha_3 \ D_1 x\ _2^2 \right\}$

Table 2.1: Spectral reconstruction techniques/methods considered in this work, and the corresponding problem they solve. Depending on the nature of the problem and input vector, various techniques are such as convex optimization and gradient descent are available to solve the problem. The c coefficients for the RBF Network are computed via $c = (AK)^\dagger y$, where K is the kernel matrix $K_{\lambda, \lambda_d} = e^{-\beta|\lambda - \lambda_d|^2}$ and λ_d are the centers of the radial basis functions.

to be performed once for each spectrometer module. I found that these methods (BPDN, LASSO, elastic-net) tend to perform reasonably well for sparse spectra such as a few input laser lines. However, BPDN and LASSO (which only weight the L_1 -norm) fail to faithfully reproduce broad spectral features where the input spectrum contains few (if any) zeros, as illustrated by the low R_2 values in Table A.1 as well as examples of the reconstructed spectra presented in Figures A-1 & A-2. Other techniques I considered, such as Ridge Regression (which only weights the L_2 -norm), pseudo-inverse (Penrose-Moore), and radial-basis function (RBF) networks, exhibit significant reconstruction errors on both broad and narrow spectral features. The latter method (RBF Network) is the analytical solution to a regression model that bounds all derivatives of the solution vector [6].

To properly account for both the sparsity and ‘smoothness’ of the spectra, a regularized regression model that accounts for both L_1 - and L_2 -norms as well as the first-derivative of the spectrum was implemented. This method, that is called “elastic- D_1 ” from here on, is a non-negative elastic-net method with an additional smoothing

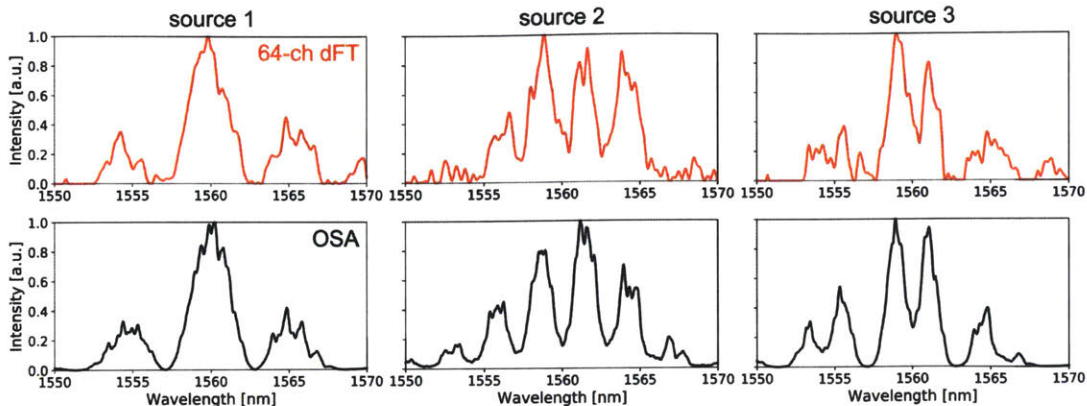


Figure 2-4: Broadband signal reconstruction. Three unique light sources with broad spectral features were measured using the dFT spectrometer chip and elastic- D_1 method (top red curves) and compared to measurements by a benchtop optical spectrum analyzer (OSA) (bottom black curves). The three light sources were generated using amplified spontaneous emission from an erbium doped fiber passed through several Mach-Zehnder interferometers (additional information is provided in the Methods).

prior. It solves the regularization problem:

$$\min_{x, x > 0} \left\{ \|y - Ax\|_2^2 + \alpha_1 \|x\|_1 + \alpha_2 \|x\|_2^2 + \alpha_3 \|D_1 x\|_2^2 \right\} \quad (2.4)$$

where α_1 , α_2 , and α_3 are hyperparameters that weight the corresponding L_1 - and L_2 -norms on x , and the L_2 -norm on the first derivative specified by the matrix D_1 . The combination of bounds on the L_1 -norm (that induces sparsity on the spectrum), L_2 -norm (that bounds magnitude of the spectrum), and first derivative of the spectrum (that sets the desired smoothing) produce significantly better reconstructions (compared to other known methods) on both broad and narrow spectral features without requiring knowledge of the true input spectrum. Since Eq. 4 is a non-negative quadratic program, it is readily solvable with standard convex optimization tools [10]. Details of the elastic- D_1 algorithm, its implementation, and performance benchmarking compared to several existing reconstruction techniques are presented in Table 2.2 and Appendix A. The comparison in Table 2.2 suggests that the elastic- D_1 algorithm significantly outperforms other techniques for both sparse and broadband input sig-

nals.

To demonstrate the versatility of the elastic- D_1 method, I applied the technique to experimentally measured interferograms for two types of polychromatic inputs, sparse signals consisting of discrete laser lines and broadband signals with complex spectral features (see Methods). Figure 2-3 plots the reconstructed spectra comprising two laser lines with slightly different amplitudes and varying wavelength spacing. The elastic- D_1 technique precisely reproduces the laser wavelengths with ± 0.025 nm accuracy, only limited by the finite wavelength step size of the calibration matrix (0.025 nm). The spectral resolution of this device, determined here by the minimum resolvable wavelength detuning between two laser lines, significantly outperforms the Rayleigh criterion of 0.4 nm with an experimentally determined value of 0.2 nm. The enhanced reconstruction quality is a result of the elastic- D_1 method's automatic consideration of the tradeoffs between spectral sparsity, magnitude, and smoothness (see Appendix A. Figure 2-4 compares the spectra of three unique broadband inputs recorded using a benchtop optical spectrum analyzer as a reference and reconstructed spectra using the same 64-channel dFT device and elastic- D_1 algorithm. The high reconstruction quality on arbitrary input spectra with characteristic spectral features ranging from several nanometers to well below the Rayleigh limit validates dFT spectroscopy as a generic, powerful tool for quantitative spectroscopy.

2.5 Discussion

Optical spectrum analysis using a Mach-Zehnder interferometer with physical path differences enables high-resolution spectroscopy with limited interferogram measurements. By utilizing a reconfigurable interferometer, a working dFT spectrometer device was demonstrated that both recovers the multiplex advantage (as seen by the low-insertion loss per channel in Table A.1), and is capable of high-resolution spectrum acquisition with a compact form factor. For input spectra with slowly varying (broad) spectral features, the elastic- D_1 spectral reconstruction technique provides

Method	R^2 value (sparse)	R^2 value (broad)	Average fixed- parameter compute time [msec]	Hyper- parameter search time [sec]	Hyper- parameter search space
Pseudoinverse	-12.365	0.636	<0.01	N/A	1
Ridge regression	-11.453	0.717	1.08	0.5	500
LASSO	0.897	-0.247	29.08	14.5	500
BPDN	0.810	-0.388	155.0	77.5	500
RBF Network	-12.296	0.650	47.63	9.5	200
Elastic-Net	0.845	0.632	22.6	904	200 \times 200
Elastic-D_1	0.987	0.834	291.0	502.8	12 \times 12 \times 12

Table 2.2: Performance comparison of reconstruction methods. R^2 value of reconstruction on sparse spectra consisting of two laser lines at $\lambda = 1552.5$ nm and $\lambda = 1567.5$ nm and broadband spectra (black curve in Fig. 2-4c). For each reconstruction technique, I included the average time to solve the corresponding problem (shown in Table 2.1), the hyperparameter search space, and the dimensionality/size of the hyperparameter space. The results show that the elastic- D_1 algorithm significantly outperforms other techniques for both sparse and broadband input signals.

a superior reconstruction accuracy than other regularization or compressive sensing techniques at the expense of increased computation time to determine suitable hyperparameters. A thorough comparison of the elastic- D_1 technique compared to other common reconstruction methods is shown in Table A.1 and graphically depicted in Figure A-1 & A-2. Note that errors tend to occur at the edges of broad spectra after reconstruction since the signal (interferogram) is bandlimited in the spatial domain. However, these errors are expected to become negligible as the number of unique OPL differences (determined by the number of switching stages via Eq. 2.1) and spectral channels increases. As channel count increases, the system also becomes less underconstrained and reconstruction errors are expected to decrease significantly. Increasing channel count is simple and inexpensive in terms of chip-space – a dFT spectrometer with 2 additional (5 total) switching stages (i.e. a total of $j = 10$ switches) would access 1,024 unique spectral channels while occupying only 40% more chip area than the 64-channel device demonstrated here. This device architecture will hopefully pave the way towards future on-chip spectrometers with significantly larger spectral

channel counts, higher-resolution, and dramatically increased optical throughput with respect to prior on-chip spectrometer demonstrations.

In conclusion, this work pioneers dFT spectroscopy as a high-performance, scalable solution for on-chip optical spectrum analysis. Its unique exponential scalability in performance, superior SNR leveraging the multiplex advantage, as well as compact and remarkably simplified device design are among the key advantages of the technology. Moreover, its proven compatibility with industry-standard foundry processes enables scalable manufacturing and drastic cost reduction. Furthermore, an elastic- D_1 machine learning regularization technique was developed to achieve significant noise suppression and resolution enhancement. The powerful combination of dFT spectroscopy and machine learning techniques will empower future applications of spectroscopy such as chemical and biological sensors-on-a-chip, space-borne spectroscopy, optical network monitoring, and radio-frequency spectrum analysis.

Chapter 3

Optimized waveguide geometries for evanescent field sensing in the presence of sidewall roughness^{*}

God made the bulk; surfaces were
invented by the devil

Wolfgang Pauli

Overview

The unique ability of slot and sub-wavelength grating (SWG) waveguides to confine light outside of the waveguide core material has attracted significant interest in their application to chemical and biological sensing. However, a high sensitivity to sidewall-roughness-induced scattering loss in these structures compared with strip waveguides casts doubt on their efficacy. In this chapter, we seek to settle the controversy for silicon-on-insulator (SOI) photonic devices by quantitatively comparing the sensing performance of various waveguide geometries through figures of merit that we derive for each mode of sensing. These methods (which may be readily applied to other material systems) take into account both modal confinement and roughness scattering loss, the latter of which is computed using a volume-current (Green's function) method with a first Born approximation. For devices based on the standard 220 nm SOI platform at telecommunication wavelengths ($\lambda = 1550$ nm), whose propagation loss is predominantly limited by random line-edge sidewall roughness scattering, our model predicts that properly engineered TM-polarized strip waveguides claim the best performance for refractometry and absorption spectroscopy, whereas optimized slot waveguides demonstrate $> 5\times$ performance enhancement over the other waveguide geometries for waveguide-enhanced Raman spectroscopy.

^{*}This chapter is based on: D. M. Kita, J. Michon, S. G. Johnson, and J. Hu, "Are slot and sub-wavelength grating waveguides better than strip waveguides for sensing?" *Optica* 5, 1046-1054 (2018).

3.1 Introduction

Waveguide based chemical and biological sensing is rapidly advancing as a prime application area for integrated photonics. However, there is currently no universally agreed-upon waveguide geometry that optimally enhances detected signals in the presence of fabrication-induced scattering losses. In classical strip waveguide sensors (Fig. 3-1), molecules of interest interact with the relatively weak evanescent electric field outside the waveguide core. To boost light-molecule interactions, slot waveguides [16,17,31,37,42,115] and SWG waveguides [64,188,197] have been proposed and demonstrated as alternative sensing platforms. In these waveguides, a larger fraction of the mode resides in the low-index cladding (usually the sensing medium, such as air or water) where the molecules are located. Indeed, improved refractive-index sensitivity (defined as the induced wavelength detuning per unit refractive-index change in the surrounding media) has been experimentally validated in resonator refractometry sensors based on both slot and SWG waveguides [17,37,64], and enhanced Raman conversion efficiency per unit device length has also been measured in slot waveguides [47]. Nevertheless, the benefits may be offset by their increased susceptibility to optical loss induced by sidewall-roughness scattering. Many authors have studied roughness loss in dielectric waveguides both theoretically (through coupled-mode theory and the volume-current / Green's-function methods [87,119,142,170]) and experimentally [104,106,107,125], but these analyses focused only on minimizing the power scattered into the far field. This tradeoff between mode confinement and attenuation is typically reported for plasmonic waveguide structures [15,21,84,133,200,201] and some resonant sensor devices [81,83,132,173], but differences in fabrication conditions often make it difficult to perform side-by-side comparisons. Efficiently quantifying the tradeoff between mode delocalization and scattering loss is critically important for the rational design of chip-scale photonic sensors (as well as electro-optic modulators [97] and light sources [69]) and to date there seems to be no work that quantifies these two effects with a single figure of merit (FOM) for strip, slot, and SWG waveguides.

In this paper, we develop easily computed figures of merit (Sec. 3.2) that capture

the precise trade-off between field confinement and roughness-induced scattering loss for waveguide-based sensing applications. The key to efficiently evaluating our figures of merit is perturbation theory [88,170], both to evaluate the impact of mode confinement on sensing (see Section 3.2 and Appendix B) and also to evaluate roughness scattering by computing the power radiated by equivalent current sources along the surface [71, 87] (Sec. 3.3). The latter approach circumvents costly and roughness-dependent direct simulation of disordered waveguides, giving us a figure of merit comparison independent of the precise roughness statistics as long as the roughness correlation length is sub-wavelength. Although computation of the “effective” sources to represent roughness scattering is in general quite complicated [87], we both propose a powerful general approach and we demonstrate that, for typical experimental roughness, a simple “locally flat perturbation” approximation is accurate (Sec. 3.3 and SI). The results of this work indicate that larger modal overlap with the sensing medium does not always correspond to better performance (due to increased scattering losses). By evaluating our figures of merit for strip, slot, and sub-wavelength grating (SWG) designs for bulk/surface/Raman sensing (Sec. 3.4), we obtain the results that for typical SOI waveguides at a wavelength of $\lambda=1550$ nm (1) the simple TM-polarized strip waveguide is $> 3\times$ better than other geometries considered here for bulk absorption sensing and refractometry, (2) the TM-polarized strip waveguide and TE-polarized slot waveguide are both $> 3\times$ better than other geometries for surface-sensitive refractometry and absorption sensing, and (3) the TE-polarized slot waveguide is $> 5\times$ better than other geometries for Raman sensing. Furthermore, we provide an extensive comparison (Sec. 3.5) to published experimental results, in which we applied our numerical method to compute the ratio of losses for pairs of waveguide geometries that were fabricated and reported in the literature, and our predictions exhibit good agreement to within experimental accuracy. As discussed in our concluding remarks (Sec. 3.6), we believe that these comparisons and figures of merit will drive future experimental and theoretical exploration of new waveguide geometries for the purpose of sensing.

3.2 Sensing Figures of Merit

Here we consider three sensing techniques: 1) surface-sensitive refractometry and absorption sensing, where a sensor surface is coated with a binding agent (e.g. antibody) that specifically attaches to the target molecule and the device monitors the change in index or optical absorption caused by monolayer or few-layer molecular binding on the surface; 2) bulk index/absorption sensing, where the sensor detects the change in bulk index/absorption in the adjacent sensing medium; and 3) waveguide-enhanced Raman spectroscopy (WERS) [48,62,79], where the excitation light and spontaneous Raman emission signal from molecules in the surroundings co-propagate in a waveguide. In all cases, the sensor performance is related to the external confinement factor and divided by the attenuation coefficient. This “benefit-to-cost” ratio is described in [173] for absorption spectroscopy in silicon and silicon nitride waveguides and in [21] for plasmonic waveguides, where there is a similar drive to maximize waveguide confinement and minimize the strong attenuation coefficients of surface plasmon polaritons [15]. Equivalently, for optical resonator refractometers the appropriate figure of merit is often stated as the ratio of the refractive-index sensitivity to the resonance full-width at half maximum (FWHM) (which is proportional to the attenuation coefficient) [81,83,84,132,133,200,201]. For most prior literature that analyzes sensing in non-resonant waveguide devices (and also some resonant devices [37,72,139]), the quantity of interest typically reported is the fractional power change for a small increase in analyte (i.e. the numerator of our FOM) [19,57,77,98,115,116,168]. This is likely due to the difficulty in precisely measuring the attenuation coefficient or scattering loss for a single evanescent waveguide sensor or Mach–Zehnder refractometer [27,107] (in contrast, for resonant devices this information is immediately available in the resonance FWHM) [159].

The general goal in the first two sensing modes is to maximize the device sensitivity, which is the change in fractional optical power ($\Delta P/P_{\text{input}}$) induced by a small change in the number of analyte molecules that alter the cladding absorption coefficient or index of refraction. Thus, the relevant metric is the sensitivity in units of

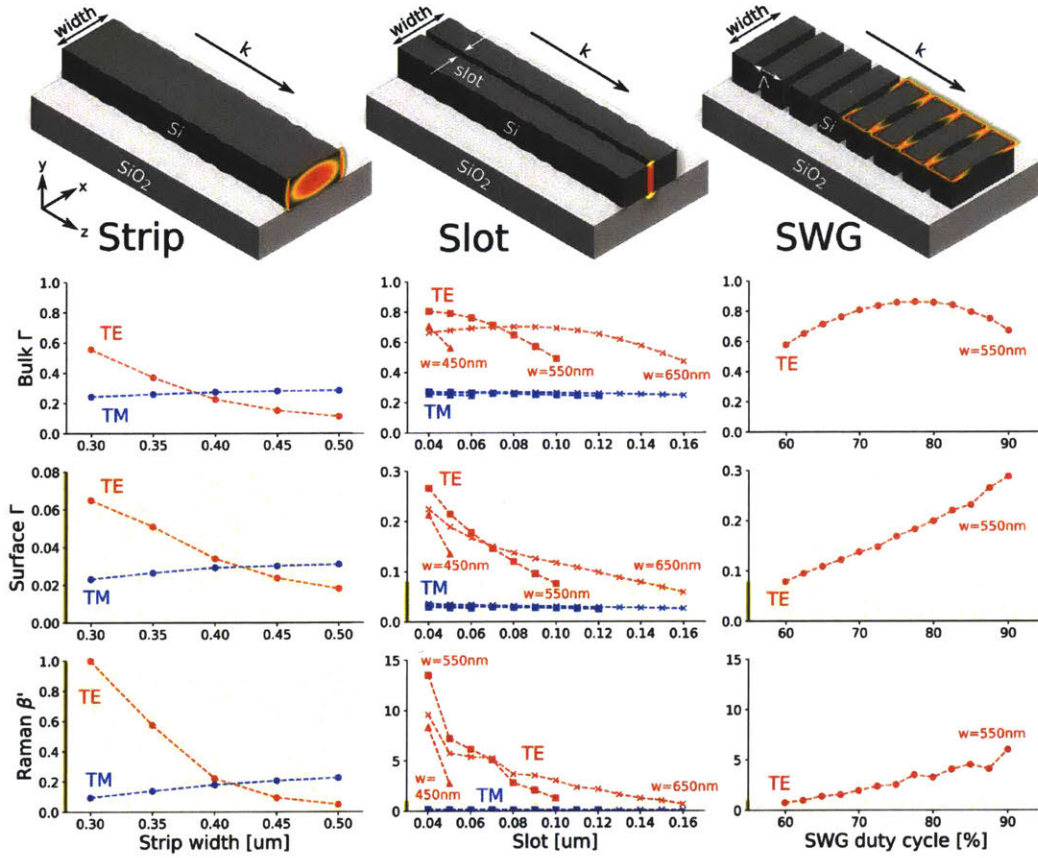


Figure 3-1: Top row: vertically symmetric surface roughness along a silicon strip waveguide on silicon dioxide substrate, a slot waveguide, and a SWG waveguide. The electric field magnitude $|\vec{E}|^2$ is overlaid at several cross-sections. Second (from top) to fourth rows: external (bulk) confinement factor Γ , surface confinement factor Γ (field integral over 8 nm thin region at air/solid interface), and the *normalized* Raman gain coefficient β' , respectively, for each single-mode waveguide geometry as a function of the relevant design parameters (total width, slot size, and duty cycle). Shaded regions denote the relative y-axis scaling between adjacent plots in each row. For slot waveguides, the total width is denoted as follows: $\triangle=450$ nm, $\square=550$ nm, and $\times=650$ nm. For SWG waveguides, the width and period are fixed to 550 nm and 250 nm, respectively. The surface Γ and bulk Γ are calculated via first-order perturbation theory (which is exactly equivalent to Eq. 3.3) with a resolution of 256 pixels/ μm and for SWG waveguides with a resolution of 128 pixels/ μm . The Raman gain coefficients are computed via Eq. 3.4 and 3.5 in 3-dimensions with a resolution of 128 pixels/ μm .

inverse number density. For example, as described in the SI, the absorption sensitivity is proportional to $\Gamma_{\text{clad}}\alpha_0/\alpha_s$, where Γ_{clad} is either the external confinement factor of the entire cladding region for bulk sensing or the surface region (approximated by

a thin volume next to the interface), α_s is the scattering loss per unit length, and α_0 is the molecular absorption coefficient (related to the bulk absorption coefficient via $\alpha_{\text{abs}} = m\alpha_0$, where m is the number density of analyte molecules). In general, we find that the only geometry dependence occurs in a factor $\Gamma_{\text{clad}}/\alpha_s$, leading us to the dimensionless figure of merit for surface sensitive and bulk absorption/index sensing:

$$\text{FOM}_\Gamma = \frac{\Gamma_{\text{clad}}}{\alpha_s \lambda} \quad (3.1)$$

where λ is the vacuum wavelength of light. In the third sensing mode (Raman sensing), the goal is to maximize the power of Raman scattered light collected at the output of a waveguide for a given input laser power. As such, the corresponding figure of merit is the dimensionless quantity derived in the SI:

$$\text{FOM}_\beta = \frac{\beta}{\alpha_s} \quad (3.2)$$

where β is the Raman gain coefficient (with units of 1/length) defined as the power of evanescently scattered Raman light collected back into the waveguide per unit length and normalized by the input power. The external confinement factor [70, 90, 99, 138, 157, 165, 177, 189] as well as the Raman gain coefficient are quantified via perturbation theory (see SI):

$$\Gamma_{\text{clad}} = \frac{dn_{\text{eff}}}{dn_{\text{clad}}} = \frac{n_g}{n_{\text{clad}}} \frac{\int_{\text{clad}} \epsilon |\vec{E}|^2 d^2x}{\int \epsilon |\vec{E}|^2 d^2x} \quad (3.3)$$

$$\beta = \frac{\alpha_{\text{ram}}^2 \omega_n^2 m}{4c^2} \cdot \frac{n_g^2(\omega)}{n_{\text{clad}}^2} \frac{\int_{\text{clad}} |\vec{E}(x, \omega)|^4 d^2x}{(\int \epsilon(x) |\vec{E}(x, \omega)|^2 d^2x)^2} \quad (3.4)$$

where n_{clad} , n_{eff} , and n_g are the cladding material, effective, and waveguide group indices, ϵ is the permittivity, E is the electric field of the waveguide mode, ω is the input angular frequency, integration is over the cross section of the waveguide, restricted in the numerator to the cladding/sensing region, and c is the speed of light. We also assume that the Raman shift is relatively small so that $|\Delta\omega| \ll \omega$. For periodic structures such as SWG waveguides, integration is performed over the

volume of a unit cell with period Λ :

$$\beta_{\text{SWG}} = \frac{\alpha_{\text{ram}}^2 \omega_n^2 m}{4c^2} \cdot \frac{n_g^2(\omega) \Lambda \cdot \int_{\text{clad}} |\vec{E}(x, \omega)|^4 d^3x}{n_{\text{clad}}^2 (\int \epsilon(x) |\vec{E}(x, \omega)|^2 d^3x)^2} \quad (3.5)$$

We note here that the optimized length of the waveguide for FOM_Γ is $z = 1/(\alpha_s + \Gamma_{\text{clad}}\alpha_{\text{abs}}) \sim 1/\alpha_s$ and for FOM_β is $z = 1/\alpha_s$. In this work we assume that sidewall roughness scattering constitutes the dominant source of optical loss in waveguides, which is typically the case in high-index-contrast waveguide systems at moderate optical powers such as SOI [28, 105, 122], silicon nitride on insulator [20, 193], chalcogenide glass on oxide [82], and TiO_2 on oxide [61]. We also note that each FOM is generic to many different sensing device configurations, such as serpentine/spiral waveguides, ring resonators, and Mach-Zehnder interferometers.

In all three cases, the sensor limit of detection (LOD) is determined by the modal overlap with the sensing region as well as the optical path length, the latter of which is limited by the waveguide propagation loss. The surface or bulk modal confinement factors and the Raman gain coefficient are readily computed from standard frequency-domain eigenmode solvers and the results are plotted in Fig. 3-1, which clearly show that slot and SWG structures indeed significantly enhance modal overlap with the sensing medium.

3.3 Scattering-loss calculations

In the volume-current method, waveguide perturbations can be described to first order (neglecting multiple-scattering effects) by dipole moments (polarizations) induced in the perturbation by the original (unperturbed) waveguide field \vec{E}_0 . These perturbations act as current sources that create the scattered field. For example, a small perturbation $\Delta\epsilon$ in the permittivity acts like a current source $\vec{J} = \Delta\epsilon\vec{E}_0$ [101, 119]. However, for perturbations in high-index-contrast waveguide interfaces, calculating the induced polarization (and hence the effective current source) is in general much more complicated [87], and requires solving a quasistatics problem (Poisson's equa-

tion) [86]. For a given statistical distribution of the surface roughness, we show in Appendix B how we can solve a set of quasistatics problems to compute the corresponding statistical distribution of the polarization currents. Fortunately, however, there is a simplification that applies to typical experimental regimes ($L_c > 10\sigma$, where L_c is the correlation length of the surface roughness and σ the root mean square roughness amplitude). If L_c (typically 50–100 nm for SOI waveguides) is much larger than the amplitude of the roughness (0.5–2 nm in state-of-the-art devices [104, 185, 192, 195]), then one can approximate the surface perturbation as locally flat. In this case, there is an analytical formula for the induced current from a locally flat interface shifted by a distance Δh [86]:

$$\vec{J} = -i\omega\Delta h(\Delta\epsilon E_{\parallel} - \epsilon\Delta(\epsilon^{-1})D_{\perp})\delta(\vec{x}) \quad (3.6)$$

(Note that the currents depend on the orientation of \vec{E}_0 relative to the interface: E_{\parallel} is the component of E_0 parallel to the surface and D_{\perp} is the component of ϵE_0 perpendicular to the surface.) In this case, the correlation function of the current J is simply proportional to the correlation function of the surface profile. We verify in Appendix B that the full quasistatic calculation reproduces this locally flat interface approximation in typical experimental regimes.

Given these currents and their statistical distribution (from the statistics of h), one can then perform a set of Maxwell simulations on the unperturbed waveguide geometry (hence, at moderate spatial resolution) to find the corresponding radiated power. Again, there is a somewhat complicated procedure in general to compute the effect of currents with an arbitrary correlation function. But, in the case where the correlation length (~ 100 nm) is much less than the wavelength ($\sim 1 - 2 \mu\text{m}$), we can approximate this “colored” noise distribution by uncorrelated “white” noise [71], effectively treating the currents as uncorrelated point sources with the same mean-squared amplitude $\langle J^2 \rangle$. Since the power radiated by uncorrelated point sources is additive, we can then simply average the power radiated from different points on the surface to find the scattering loss per unit length α_s [87]. Finally, the computation simplifies

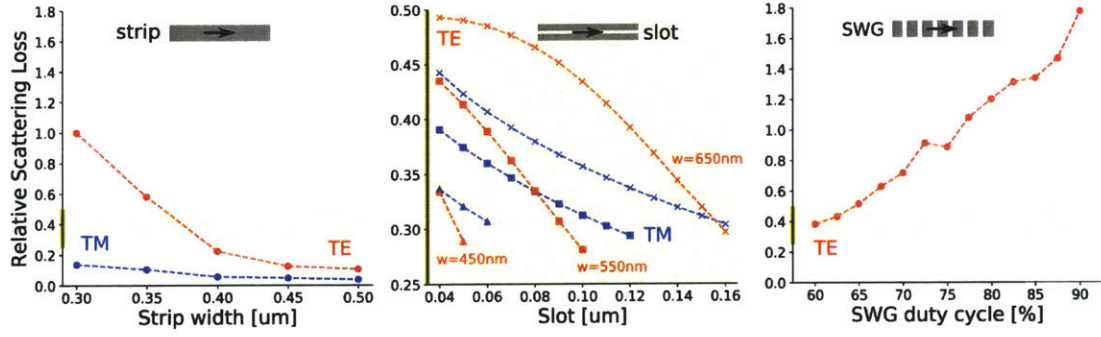


Figure 3-2: Relative scattering loss $\alpha_s / \max(\alpha_{s, \text{TE-strip}})$ computed by FDTD simulations of vertical (y -direction) lines of dipole moments and averaged over all sidewall positions. Dipole moment amplitudes were computed via Eq. 3.6 with incident field strength and phase determined by numerically computed mode profiles. Results shown for TE (red) and TM (blue) strip (left), slot (middle), and SWG (right) waveguides. For slot waveguides, the total width is denoted as follows: $\triangle=450$ nm, $\square=550$ nm, and $\times=650$ nm.

even further because we only compute the ratio of the FOMs for different waveguides, in which case all overall scaling factors and units (including all dependence on the roughness statistics L_c and σ) cancel out.

3.4 Comparison of Waveguide Geometries

Using the aforementioned volume-current method, we quantified the relative scattering losses (α_s) for a large set of strip, slot, and SWG waveguide geometries for various design parameters such as width, slot size, and duty-cycle. All waveguide geometries (Fig. 3-1) are assumed to be fabricated from SOI wafers with 220 nm Si layer thickness, negligible scattering losses at the top and bottom flat surfaces, and for a target wavelength of 1550 nm. The calculations, described in detail in SI, consist of only two computationally inexpensive steps. First, we compute the electric (\vec{E}) and displacement (\vec{D}) field profiles using a frequency-domain eigenmode solver [88], which is used to determine the confinement factors, Raman gain coefficient, and the strength of the induced dipole moments via Eq. 3.6. For each unique sidewall position and for each waveguide geometry, we use a single three-dimensional finite-difference time-domain (FDTD) simulation with a vertical line of dipole moments (correspond-

ing to vertically symmetric sidewall roughness, i.e. line-edge roughness [18, 39, 141]) to compute the scattered power from both far-field radiation and reflection. Finally, the scattered power is averaged over all inequivalent sidewall positions and computed per unit length along the direction of propagation. The relative scattering loss per unit length for the considered geometries is shown in Fig. 3-2.

For strip waveguides, we analyzed the TE-like and TM-like polarized modes for various waveguide widths. Results for slot waveguides of TE and TM polarization are computed for various total waveguide widths and air-slot gaps. For SWG waveguides, the width and period are fixed at 550 nm and 250 nm respectively, and only TE (x -antisymmetric) modes are considered as a function of the duty cycle, which is defined by $DC = (\Lambda - s)/\Lambda$ where Λ is the grating period and s is the size of the air gap along the z direction. The particular width of 550 nm and polarization was chosen for this analysis since the corresponding waveguide geometries exhibit single-mode behavior for a relatively large range of duty cycles, as confirmed by numerically computed dispersion diagrams. All waveguide dimensions are chosen such that no more than one TE and one TM mode exists.

Our results indicate that slot and SWG waveguides do in fact greatly increase scattering losses relative to standard 450 nm wide TE and TM strip waveguides [58]. The scattering loss computed by the volume-current method considers both the incident field strength at the location of the perturbation and the local density of states (LDOS) [136], which is determined by the surrounding geometry. (As such, current sources at the outer edges of a strip waveguide will radiate different amounts of power than current sources in the air-gap region of a slot waveguide.) Our comparison of scattering losses for different geometries, as shown in Fig. 3-2, is largely consistent with prior experimentally measured values of surface roughness in SOI waveguides [8, 41, 162]. However, a direct comparison between experiment and theoretically/numerically computed values is difficult since experimental uncertainties are typically on the order of a few dB/cm. In addition, an accurate comparison of scattering losses for different geometries requires side-by-side fabrication of waveguides on the same process and material platform, since different processes introduce dramat-

ically different roughness statistics. As such, literature for this is relatively scarce, and numerical methods provide a means for quickly evaluating and comparing new waveguide structures.

With the computed scattering losses, confinement factors, and Raman gain coefficients, we then computed the relevant FOM for each mode of sensing (via Eq. 3.1 and 3.2), which is presented in Fig. 3-3. Our results indicate the TE slot and SWG structures do in fact provide modest improvements in sensing performance over traditional TE-polarized strip waveguides. However, TM-polarized strip waveguides (which are here assumed to have negligible roughness on the top and bottom interfaces) exhibit significantly higher performance owing to their reduced propagation loss and longer accessible optical-path length. For bulk and surface absorption sensing, the performance of the SWG waveguides gradually decrease with increase in duty cycle (as the air-slot region becomes smaller), indicating that the increase in scattering loss in small SWG gap-regions outweighs the benefits provided by field localization in the air gap. On the other hand, slot-waveguide structures demonstrate improved performance as the slot size decreases (narrow-slot waveguides show $2\times$ improvement over large-slot waveguides for surface sensing and $5\times$ improvement for Raman sensing), with the exception of bulk absorption sensing in the air region. For bulk absorption sensing, there appears to be a critical slot size (70 nm slot for the 550 nm wide waveguides, and 130 nm slot for the 650 nm wide waveguides) below which scattering losses dominate the FOM and above which the confinement factor is suboptimal.

For Raman spectroscopy, the gain coefficient is related to the fourth power of electric field rather than the square of the electric field, so regions of high electric field exhibit significant performance enhancements, as shown by the numerically computed values of the relative Raman gain coefficient β' in Fig. 3-1. In our computations, we find that waveguides with narrow slots do in fact tend to produce sufficiently more Raman signal than what is lost due to sidewall scattering at the silicon/air interface. Wide (550 nm) silicon waveguides with narrow (40 nm) air slots yield the highest bulk Raman FOM by a factor of $8\times$ over SWG waveguides and $5\times$ over TM strip waveguide

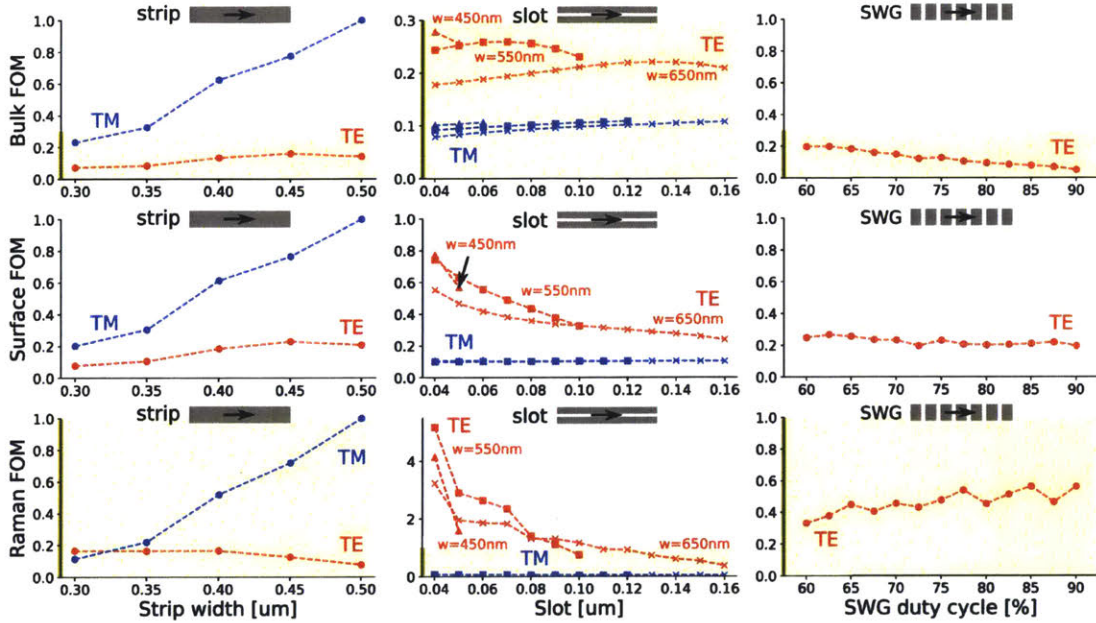


Figure 3-3: Side-by-side performance comparison for strip (left column), slot (middle column), and SWG (right column) waveguides in the presence of slow-varying ($L_c > 10 \cdot \sigma$) Gaussian random roughness. Normalized absorption sensing figure of merit FOM_Γ and normalized Raman gain coefficient $FOM_{\beta'}$ calculated via Eq. 3.1 and 3.2, respectively, as a function of the relevant design parameters (total width, slot size, and duty cycle). For slot waveguides, the total width (as depicted in Fig 3-1) is denoted as follows: $\triangle=450$ nm, $\square=550$ nm, and $\times=650$ nm.

modes. Despite having an improved Raman gain coefficient, the SWG structures suffer from significantly higher scattering losses due to the increased sidewall surface area.

3.5 Comparison with experiment

In order to demonstrate the utility and accuracy of this approach, we searched the literature for reports of fabricated strip, slot, and sub-wavelength grating silicon waveguides and their associated propagation losses [13, 25, 41, 52, 67]. We then applied the volume-current method to compute the relative scattering losses for each of 14 reported waveguide geometries. Since the waveguides of different geometries reported within each manuscript are fabricated using identical processing protocols which pre-

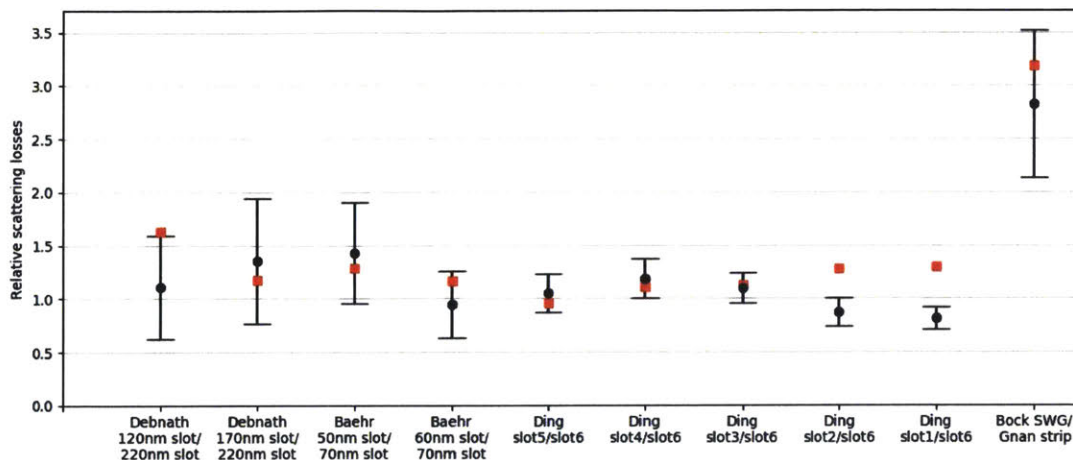


Figure 3-4: Comparison of the ratio of scattering losses between different experimentally realized waveguide systems. Red square markers denote loss ratios computed via the volume-current method described in this work and black circles denote reported loss ratios with associated error bars. Slot waveguides reported by Debnath *et al.* [41] and Baehr-Jones *et al.* [13] are labelled by the slot size, while slot waveguides by Ding *et al.* [52] are labelled by “slot1”, “slot2”, etc. corresponding to different slot sizes and strip-loading values. Bock *et al.* [25] and Gnan *et al.* [67] report losses for SWG and strip waveguides fabricated via electron beam lithography.

sumably result in identical or similar roughness characteristics, the reported losses are expected to accurately correspond to the different waveguide geometries. The authors in Bock *et al.* [25] only report the loss for a single SWG structure and reference Gnan *et al.* [67] to compare with strip waveguide losses. Both reported devices were fabricated using similar fabrication protocols (electron-beam lithography with hydrogen silsesquioxane resist and reactive-ion etching), and so we show in Fig. 3-4 the ratio of the reported propagation losses and our own numerically computed values using the reported waveguide geometries.

It is worth drawing attention to several features of Figure 3-4. First and foremost, the experimental error bars associated with measured values of propagation loss are quite large, on the order of several dB/cm. Accurately comparing the propagation loss of different waveguides requires the fabrication of all considered geometries on one single substrate and in close proximity with each other (to avoid cross-wafer variations). The waveguide losses can be characterized through either the cut-back

method (many waveguides of different lengths) or resonator devices [198]. The cut-back approach is susceptible to large variability in device-to-device coupling efficiency, whereas loss measurement using resonators only compute the loss for a small waveguide length [109]. For these reasons, it is critical to measure a statistically significant number of devices. Often, information on the sample size and measurement errors are omitted in the literature.

Ding *et al.* [52] reported the striking result that two waveguide geometries (denoted by “slot1” and “slot2” in their work) have lower loss despite a larger modal overlap with the vertical sidewall interface. As a result of the higher modal overlap, our model predicts that “slot1” and “slot2” should actually perform worse. This inconsistency may originate from other experimental sources of loss (mask defects, scattering at the top surfaces of the partially etched silicon, absorption, etc.) that were modified by the change in waveguide geometry. Otherwise, the values reported in literature are consistent with values that our volume-current method predicts, which validates our approach as a fast, powerful technique for precisely comparing the relative performance of arbitrary waveguide systems *before* investing time and resources towards fabricating real devices.

3.6 Concluding Remarks

In this work, we numerically computed the relative performance enhancement of slot and SWG waveguides over traditional strip waveguides for on-chip sensing applications. By explicitly computing the polarization statistics of randomly generated surface-roughness profiles (SI), we confirmed that a simple flat shifted-boundary approximation is accurate for most commonly encountered surface roughness (correlation length greater than roughly 10 times the RMS roughness amplitude). As a result, analytical formulas are available for the induced dipole moments from sidewall roughness. For situations where the roughness correlation length is significantly shorter than the wavelength of light, the volume-current method allows the far-field and reflected radiation loss from this roughness to be determined with good accuracy

using inexpensive numerical methods. In particular, our approach benefits from significantly reduced simulation resolution requirements compared to brute-force simulation of waveguide structures with small perturbations, as the critical resolvable dimension is the waveguide geometry rather than the perturbation amplitude at the waveguide interface [85]. In addition, these brute-force techniques require many (or long) simulations to obtain statistically averaged effects of the randomly rough surfaces.

Our approach can be readily extended to efficiently determine optimal waveguide geometries for other sensing modes, such as stimulated Raman spectroscopy [202], with a suitably defined sensing metric. There are also a number of other material platforms to which this work can be extended, such as silicon nitride on silicon dioxide [46, 48, 56, 79], titanium dioxide on silicon dioxide [62], chalcogenide glass on insulator [60, 80], germanium or germanium-silicon on silicon [32, 114], silicon on sapphire [14], and more that are of great interest to the waveguide-integrated chemical sensing community. Because the waveguide geometries, materials, and figures of merit can change for different sensing processes and wavelengths, the conclusions about which geometries are better may also change. Lastly, there is interest in extending this work to quantify the sensing performance of additional waveguide geometries, such as photonic crystal waveguides [123] and horizontal slot waveguides [175], to name just a few.

We believe this work and the methods presented will aid in the rational design of new waveguide geometries for photonic sensing applications. Without figures of merit and efficient methods for computing the loss and sensing tradeoffs, it was difficult to predict whether waveguide geometries like slot and SWG waveguides will enhance sensing performance (due to increased field overlap with the sensing medium) or decrease sensing performance (from increased scattering losses). With the techniques presented, it is possible to quantify the precise trade-off between these two competing factors for arbitrary waveguide geometries and material platforms. This will drive future research in the area of on-chip sensing and other areas where propagation loss in waveguides plays an important role.

Chapter 4

A quick-turn fabrication process for Si_3N_4 photonic integrated circuits with heaters^{*}

Overview

This chapter discusses recent trends towards the fabrication of photonic integrated circuits using fast direct-write lithography techniques in university cleanroom environments, and the inherent strengths and disadvantages when choosing to use university facilities versus taping out designs in dedicated high-volume commercial foundries. For small-volume or proof-of-concept applications, in-house fabrication of photonic integrated circuits can offer significant cost and time savings while enabling process customization that would be prohibitively expensive or unfeasible in larger commercial foundries. To illustrate this, I present a completely maskless, quick-turn process flow for fabricating low-loss silicon nitride integrated photonic devices operating from visible to infrared wavelengths. This process offers low-loss (0.36 ± 0.11 dB/cm) passive photonic devices and special fabrication steps are described for defining thermo-optic modulators, etched edge couplers, and top oxide openings (for evanescent chemical sensing or backend material deposition) which may be readily implemented in any cleanroom with a full CMOS toolset. This silicon nitride photonics process flow can be completed in an average of 16 days, with a chip cost under $1\$/\text{mm}^2$ for volumes well below 1,000 chips per run.

4.1 Introduction

The field of integrated silicon photonics has grown and matured rapidly over the last several decades, with far-reaching impacts on many fields such as telecommunications [53, 54], datacommunications [35, 146], high-performance computing [22], quantum optics [167], compact sensors [173], LIDAR [76, 148, 174], and microwave

^{*}This chapter is based on: D. M. Kita, J. Scholvin, C. Rios, J. Hu, “A Quick-Turn Fabrication Process for Si_3N_4 Photonic Integrated Circuits with Heaters” (*manuscript currently in review*).

photonics [158] to name just a few. Among the many different material platforms used to fabricate photonic integrated circuits, silicon nitride (SiN_x) has become a popular platform for prototyping passive devices with thermal phase tuners [150]. Despite having larger waveguide bends and lacking electro-optic modulators, light detectors, integrated optical amplifiers or lasers, silicon nitride has many desirable attributes that make it an excellent candidate for specialized applications. First, silicon nitride has a broad transparency range that covers visible to infrared wavelengths, and high power-handling capabilities which are necessary for nonlinear and sensing applications [144, 150, 171, 184]. Second, the low-index contrast suppresses scattering losses due to waveguide sidewall roughness and allows for better waveguide-to-fiber mode matching for high-efficiency edge couplers [24, 144, 149, 179, 186]. While integrated photonics as a whole benefits from the reuse of mature semiconductor fabrication equipment and facilities (albeit at significantly lower volumes than traditional electronics [111, 112]), silicon nitride photonic devices in particular have not yet found the consolidated, high-volume markets needed to fully leverage the advanced CMOS infrastructure (silicon nitride photonic chips made up $<5\%$ of the global market shares of all photonic circuits in 2016 [66]). As a result, fabrication runs for photonics often involve partial wafer lots and many users opt for multi-project wafer runs to share the high manufacturing costs [112]. In addition, fabrication from start to finish can take several months [2, 3, 5], which limits development turnaround times for prototypes and new systems. When the objective is to develop a successful system prototype quickly and efficiently, a relevant quantity of interest is the cost per unit area weighted by the turnaround time and number of chips manufactured:

$$\text{FOM} = \frac{\text{cost} \times \text{turnaround time}}{\# \text{ chips} \times \text{chip area}}. \quad (4.1)$$

In this context, inexpensive and quick-turn processes are well-suited for validating component and system-level concepts. The quantity of unique chip area provided by the lithography process determines the number and size of designs, and chip quantity is crucial even at prototyping stages to gauge reliability and yield.

In this paper we describe a low-cost (<1 \$/mm²), high-performance (0.36 dB/cm propagation loss), and quick-turn (16.4 day turnaround time) silicon nitride photonics process flow that we use to fabricate integrated optical devices in a university cleanroom. Furthermore, we provide complete and detailed information about the fabrication so that this process may be readily implemented in any fabrication environment with a sufficiently complete CMOS toolset. In Section 4.2, we discuss direct-write lithography as an enabling technology for fast prototyping of small-volumes of photonic devices. We then discuss details of the fabrication process, which includes process steps for etching trenches for fiber edge-coupling, top-oxide removal for chemical sensing or back-end deposition of CMOS-incompatible materials, and patterning of thermal phase tuners. In Section 4.3 we present measurement results of various photonic devices and components that were prototyped on this silicon nitride platform. Finally, in Section 4.4 we quantitatively analyze the economics of fabricating these devices in a university cleanroom environment, where we have used data on tool history and down-time to predict the probability of completing a process within a given time.

4.2 A quick-turn silicon nitride photonics process

Table 4.1 outlines the complete process flow that we performed in the MIT Microsystems Technology Laboratory cleanroom facilities. The process begins with 3 μm thermal SiO₂ and 200 nm stoichiometric Si₃N₄ deposited on both sides of a single-side polished silicon wafer, provided by an external vendor (WaferPro, LLC). A single electron-beam lithography step and reactive ion etch step is used to pattern waveguides and passive photonics structures into the silicon nitride film. The etch is timed and monitored so that a thin, 30 nm film of silicon nitride remains, which will serve as an etch-stop in subsequent removal steps for the top oxide. After resist removal and cleaning, a 2 μm thick film of TEOS oxide is deposited and subsequently annealed under nitrogen at 950° C to remove hydrogen and densify the film [164, 191]. A second patterning and etch step is used to remove 1.6 – 1.75 μm of top oxide above

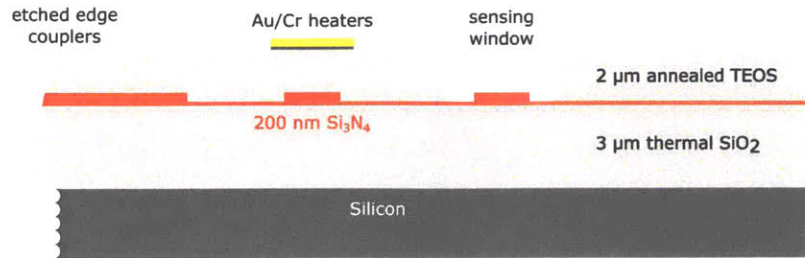


Figure 4-1: Cross-sectional schematic of the full layer stack after processing as outlined in Table 4.1.

the photonics layer (the last couple hundred nanometers of oxide is removed at the very end to protect the waveguide level from contamination). In this lithography step (and all subsequent steps), a Heidelberg MLA150 maskless aligner tool is used directly write patterns as small as 600 nm [1]. The tool takes anywhere between 10 – 45 minutes to write patterns on a full 150 mm diameter wafer, depending on the type of pattern and write mode used. Next, a lithography step and 5 μm oxide etch step is used to form the vertical facet where the fibers will be aligned. Next, gold heaters are fabricated on the wafer by a third lithography step, using electron beam evaporation of Cr (adhesion layer) and 100 nm Au, then subsequent liftoff of AZ5214E image reversal photoresist. A fourth lithography step is used to pattern the areas where 150 μm of silicon is removed via deep reactive ion etching. The final step is to pattern photoresist that will protect the top oxide and gold heaters during a wet etch of buffered oxide etchant (BOE). At this stage the wafer is diced, sonicated in water to remove silicon particulates, and then dipped in BOE until the top oxide above the waveguides is fully removed. The photoresist is sonicated in acetone, and the chips surfaces are cleaned in oxygen plasma. The finished device cross-section is represented schematically in Figure 4-1. The regions with removed top cladding are useful for evanescent chemical sensing applications and for deposition of exotic materials, such as phase change materials [156] or liquid crystals [30].

A unique aspect about this process is that it leverages only direct-write lithography techniques to define high-quality (50 nm critical dimension) waveguides and sufficiently high-resolution features that make up the heaters, edge couplers, and

window openings. While stepper lithography tools are sufficient for patterning devices, the usable area is limited to a single reticle and there is a cost in time and money to acquiring masks. Furthermore, access to state of the art 193nm deep-UV lithography tools for patterning low loss waveguides is often times prohibitively expensive or limited in university environments. Direct-write maskless aligners and electron beam lithography tools are significantly less expensive for shared cleanroom facilities to purchase and offer comparable levels of performance at the expense of throughput. These tools can write a full wafer with entirely unique structures, which is useful for large scale parameter sweeps or multi-project wafer runs [27, 149]. There is also no penalty for making edits or corrections to mask files immediately prior to exposure. In Table 4.1, we provide values for typical write-times and step costs for a process running on the MIT Microsystem Technology Laboratory toolset.

Table 4.1: Silicon Nitride Photonics Process Flow at MIT's Microsystems Technology Laboratory. Assumes student rates (industry rate = 4 × student rate)

Step	Machine / tool	Process details	First wafer cost [\$]	First wafer step time	Marginal cost [\$]	Marginal step time
1	(external)	150 mm prime Si wafers arrive from vendor with 3 μm wet thermal oxide and 200 nm LPCVD Si ₃ N ₄ on both sides	72.6	0	72.6	0
2	acid hood	Wafer clean in piranha solution	212.5	1 hr	0	0
3	O ₂ asher	Ash in O ₂ plasma to improve adhesion of the resist for ebeam lithography	17	5 min	17.0	5 min
4	solvent hood	Immerse wafers in SurPass 4000 (adhesion promoter) for 60 seconds, then rinse in DI water for 30 seconds, followed by spin dryer, and 5 minute dehydration bake at 120° C	0	20 min	0	0
5	Solitec 5110 coater	Spin on 350 nm ma-N 2403 negative-tone electron beam lithography resist, then bake on hotplate for 60 seconds at 90° C	17	5 min	17	5 min
6	Elionix ELS-F125	Expose photonics layer, using 800 uC/cm ² dose, 500 μm×500 μm fields, 200,000×200,000 dots/field, and 2 nA beam current with interleaving fields	884	8 hr	884	8 hr
7	PicoTrack	Spray develop ma-N 2403 resist using MF CD-26, then 90° C bake for 60 seconds	17	5 min	17	3 min
8	Applied Precision 5000	Reactive-ion etching of 165 nm Si ₃ N ₄ (8 sccm CF ₄ , 6 sccm O ₂)	60.9	10 min	60.9	2 min
9	Tencor UV-1280	Measure the etch depth from prior step (halfway through)	7	10 min	2.1	3 min
10	O ₂ asher	Strip resist, clean Si ₃ N ₄ surface	17.5	5 min	0	5 min
11	acid hood	Piranha clean wafers	212.5	1 hr	0	0
12	Novellus Concept 1	Deposit 2 μm PECVD TEOS oxide	76.5	40 min	76.5	5 min
13	MRL 718 Tube	Tube anneal of top oxide for 1 hour at 950° C under N ₂ flow	212.5	3.5 hr	0	0
14	PicoTrack	Coat SPR700 1.0 μm thick	17	5 min	17	3 min
15	MLA150 Maskless Aligner	Expose sensing regions of the wafer	39.7	20 min	39.7	20 min
16	PicoTrack	Spray develop in CD-26 for 45 seconds	17	5 min	17	3 min
17	Applied Precision 5000	Reactive-ion etching of 1.6–1.75 μm TEOS top oxide	73.1	20 min	73.1	8 min
18	O ₂ asher	Strip resist in O ₂ plasma for 5 minutes	17.5	5 min	0	5 min
19	PicoTrack	Coat SPR700 2.0 μm thick	17	5 min	17	3 min

Table 4.1 continued from previous page

Step	Machine / tool	Process details	First wafer cost [\$]	First wafer step time	Marginal cost [\$]	Marginal step time
20	MLA150 Maskless	Expose deep-etched regions for the optical fiber	39.7	20 min	39.7	20 min
	Aligner					
21	PicoTrack	Spray develop in CD-26 for 45 seconds	17	5 min	17	3 min
22	Applied Precision 5000	Reactive-ion etching of 2.0 μm TEOS top oxide, the Si_3N_4 layer, and 3 μm bottom thermal oxide (45 sccm CHF_3 , 15 sccm CF_4)	102	50 min	102	42 min
23	O_2 asher	Strip resist in O_2 plasma for 5 minutes	17.5	5 min	0	5 min
24	Solitec 5110 coater	Coat 1.6 μm AZ 5214E image reversal photoresist (60 seconds, 3 krpm)	17	5 min	17	5 min
25	MLA150 Maskless	Exposure of heaters/traces with 18 mJ/cm ² , followed by a 2 minute	39.7	20 min	39.7	20 min
	Aligner	bake at 120° C				
26	OAI UV flood exposure system	Flood exposure of resist with UV light for 35 seconds	0	1 min	0	1 min
27	developer hood	Develop in MIF 422 for 120 seconds or until pattern clears	0	2 min	0	2 min
28	Temescal VES2550	Electron beam evaporation of 30 nm Cr, then 100 nm Au	258.4	4 hr	64.6	1 hr
29	solvent hood	Liftoff resist in NMP or acetone with sonication	0	1 hr	0	0
30	PicoTrack	Coat SPR700 2.0 μm thick	17	5 min	17	3 min
31	MLA150 Maskless	Expose deep silicon etch regions of the wafer	39.7	20 min	39.7	20 min
	Aligner					
32	PicoTrack	Spray develop in CD-26 for 45 seconds	17	5 min	17	3 min
33	STS Pegasus DRIE	Deep reactive-ion etch of 150 μm silicon (Bosch process)	110.5	30 min	110.5	20 min
34	O_2 asher	Strip resist in O_2 plasma for 5 minutes	17.5	5 min	0	5 min
35	PicoTrack	Coat SPR700 2.0 μm	17	5 min	17	3 min
36	MLA150 Maskless	Expose sensing regions (again)	39.7	20 min	39.7	20 min
	Aligner					
37	PicoTrack	Spray develop in CD-26 for 45 seconds	17	5 min	17	3 min
38	Disco DAD-3240	Dice wafer	59.5	30 min	59.5	30 min
39	photo hood	Manually apply a drop of photoresist over etched edge coupler regions	0	30 min	0	30 min
		for protection during the subsequent oxide etch				
40	acid hood	Dip in buffered oxide etchant (7:1 $\text{NH}_4\text{F}:\text{HF}$) for ~6-7 minutes to remove the 250-400 μm of oxide above the sensing regions	68	1 hr	0	0
41	solvent hood	Strip resist off surface in acetone	0	15 min	0	15 min
42	O_2 asher	Clean surface in O_2 plasma (optional)	17.5	10 min	0	10 min
Full process:			2909.0	27.0 hr	1908.3	14.5 hr

4.3 Device performance

The specific silicon nitride layer height (200 nm) and etch depth (~ 165 nm) were chosen such that for reasonable widths a well-confined quasi-TE and -TM mode is supported at both C-band wavelengths ($\lambda \sim 1550$ nm) and near-visible wavelengths ($\lambda \sim 808$ nm). The mode cutoffs as a function of wavelength and waveguide width are shown in Figure 4-2, overlaid with the effective index of the fundamental TE₁ mode. At $\lambda=1550$ nm, the waveguide width is chosen to be $1.3 \mu\text{m}$. To measure the propagation loss of light in the waveguides, all-pass ring resonators with radii between $40 \mu\text{m}$ and $160 \mu\text{m}$ and coupling gaps between $0.6 \mu\text{m}$ and $1.6 \mu\text{m}$ were fabricated with vertical grating couplers for input and output coupling to single mode fibers. Optical spectra obtained using a commercial optical vector analyzer (Luna OVA 5000), such as that shown in Figure 4-3, were subsequently analyzed using a linear-regression-based approach to determine the round-trip propagation loss (a) and self-coupling coefficient (r) [43]. As shown in Table 4.2, ring radii above $100 \mu\text{m}$ had measured loss values of 0.35-0.37 dB/cm with standard deviations of ~ 0.1 dB/cm. We do note that actual losses across an entire chip (rather than isolated measurements of single rings) are likely to be larger, since stitching errors between adjacent write-fields on the electron beam lithography tool can introduce significant offsets. For example, the Elionix ELS-F125 tool used in this work has $500 \mu\text{m} \times 500 \mu\text{m}$ large write fields, which must all be stitched together with waveguides that can cross all four field edges. If there is a slow drift in the stage position, then adjacent fields that are not written sequentially can be offset by small but non-negligible amounts on the order of 10's of nm. However, methods exist for compensating this, such as ensuring that the sample stage inside the chamber has sufficient time to thermally equilibrate with the tool after loading. We also pre-process the write files such that adjacent fields edges consist of 200 nm long and 20 nm wide interdigitated fingers to prevent small offsets from introducing gaps in the waveguides.

Inverse taper spot-size converteres, for coupling light from a fiber at the edge of the chip into the waveguides, were designed for 500 nm wide single mode waveguides

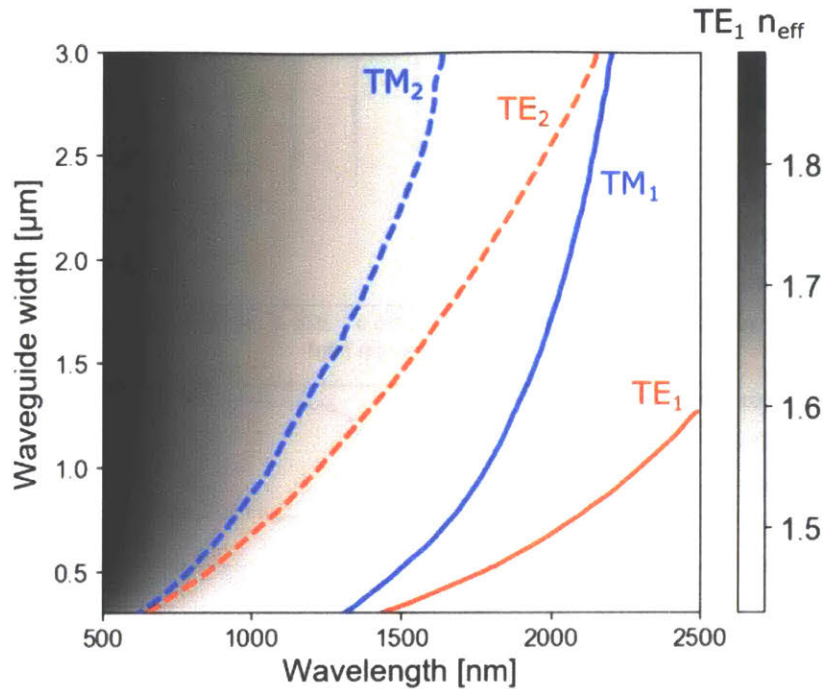


Figure 4-2: Numerically computed mode cutoffs for the first two quasi-TE and quasi-TM waveguide modes of the partially etched 200 nm thick Si_3N_4 waveguides. Each line corresponds to a 5 dB/cm iso-loss contour, and is superimposed on top of the first TE mode effective index. Single-mode operation occurs for waveguide geometries between the solid and dashed lines.

operating at $\lambda = 808$ nm for chemical and biological sensing applications. The tapers were $100\ \mu\text{m}$ long and taper down to a width of 70 nm for an estimated 50.6% (-2.96 dB) coupling efficiency from modal overlap calculations. With additional lithography steps, it is possible to significantly increase the edge coupling efficiency via removing the 35 nm thick partially etched silicon nitride using thinner silicon nitride at the edge for a larger optical mode. Similarly, thicker top and bottom oxide would allow for larger optical modes to better couple light to fibers at the edge of the chip. Microscope and scanning electron microscope (SEM) images of the inverse spot size converter are shown in Figure 4-4. The electron-beam resist (ma-N 2403, *micro resist technology, GmbH*) is spun on at a thickness of ~ 350 nm, and to prevent the resist at the 70 nm wide region from detaching or falling over, we write larger ‘anchor’ structures that mechanically hold the tip in place (Figure 4-4a). These anchors are completely etched away during the subsequent deep oxide etch, which produces

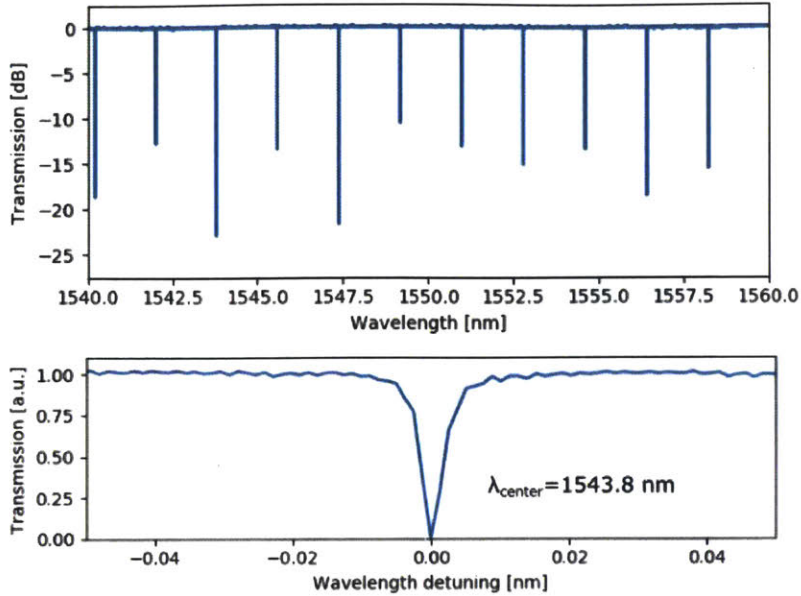


Figure 4-3: Experimentally measured transmission for an all-pass resonator used to determine the silicon nitride waveguide propagation loss.

a smooth oxide sidewall with a 76.3° angle (Figure 4-4b). Trenches with both oxide and $150 \mu\text{m}$ of silicon are etched at the spot size converter to allow access for a single mode optical fiber. Optical fibers were aligned to the chip edge and glued in place using UV-curable epoxy.

Exposed windows for evanescent field chemical sensing are formed by first a reactive ion etch through most of the top oxide cladding, and then a second timed wet etch using the silicon nitride film as an etch stop. A top down SEM image of this type of sensing region is shown in Figure 4-5. Due to the increased index contrast between

Table 4.2: Waveguide loss measurements extracted from ring resonators

R [μm]	Quality Factor	Loss [dB/cm]	# peaks
60	23300 ± 6800 max=33200	2.74 ± 1.4	19
80	225400 ± 30800 max=275500	0.39 ± 0.15	25
100	281300 ± 67300 max=411800	0.35 ± 0.12	30
120	286400 ± 63700 max=401700	0.35 ± 0.09	37
140	282600 ± 53100 max=389300	0.37 ± 0.12	43
160	280900 ± 50600 max=402900	0.36 ± 0.11	49

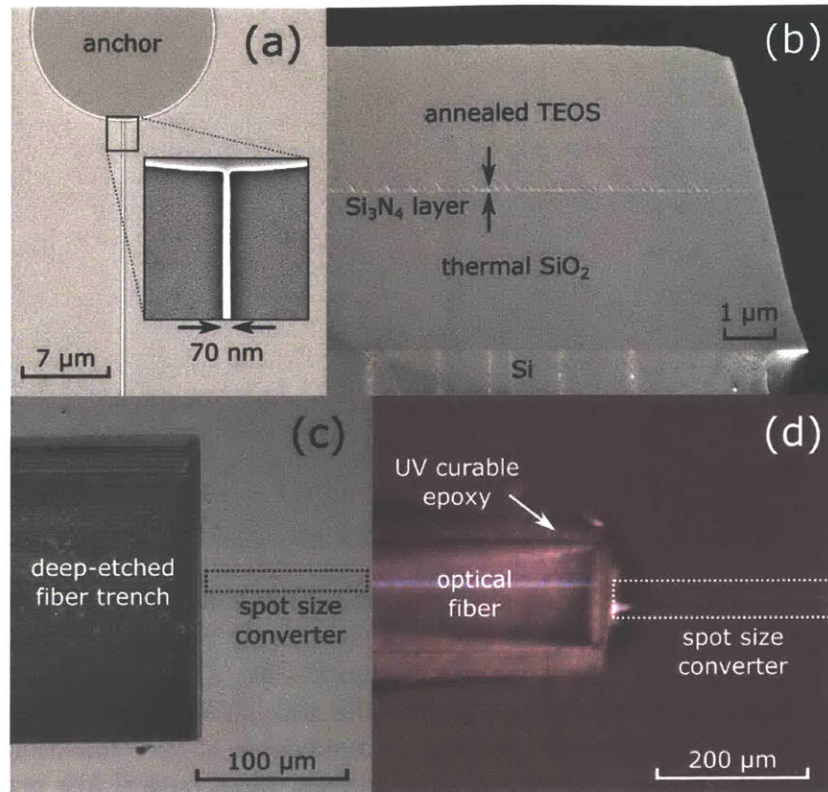


Figure 4-4: (a) Top-down SEM image of the inverse taper (spot size converter) used for expanding the waveguide mode at the chip edge. The anchor at top prevents the narrow resist from falling over and is completely etched away at process step 22. (b) Cross-sectional (side) SEM image of the oxide sidewall after deep reactive ion etching of the silicon dioxide and silicon. For this particular sample, the deposited TEOS oxide was $3\ \mu\text{m}$ thick, and the sidewall angle is 76.3° . (c) 45° -tilted SEM image of the etched edge of the chip, with a deep-etched trench for the optical fiber on the left. (d) Optical microscope image of a single-mode fiber coupling light into the waveguide mode via the spot size converter and bonded in place with UV curable epoxy.

the waveguide core and top air cladding (versus SiO_2 cladding), propagation losses in this region are noticeably higher, as seen visually by the amount of out-of-plane scattering in Figure 4-5. Contamination from discrete particulates chemical sensing environments constitute significant sources of loss for these unclad waveguides.

Finally, we experimentally characterized the performance of thermo-optic heaters deposited and patterned on top of the top oxide cladding (shown in Figure 4-1). Using a set of balanced Mach-Zehnder modulators with 2×2 directional couplers at the input and output, the optical intensity as a function of heater power was recorded,

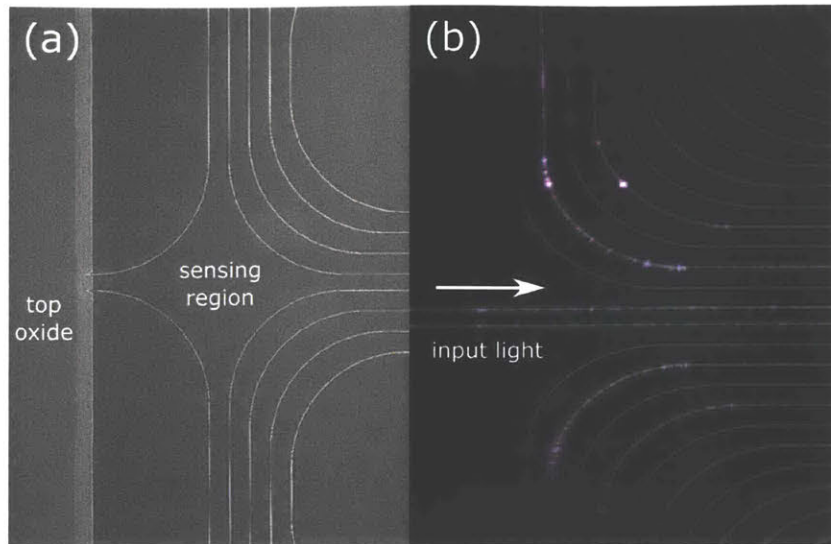


Figure 4-5: (a) Top-down scanning-electron microscope image of a waveguide sensing region, where the top TEOS oxide has been selectively removed by both reactive ion-etching and then wet etching with hydrofluoric acid. (b) An optical microscope image of $\lambda=808\text{nm}$ light travelling through the waveguides from left to right. A small amount of far-field optical scattering is noticeable at the transition when the waveguide exits the region with top oxide cladding. Most optical loss occurs in the sensing region due to waveguide sidewall roughness or scattering from particulates that settle on the surface.

as shown in Figure 4-6(a). A nonlinear least squares method was used to fit the expected sine^2 function to the measured data and extract parameters such as the extinction ratio and the heater efficiency. A heater efficiency of $322 \pm 32 \text{ mW}/\pi$ and extinction ratio of $23.3 \pm 5.5 \text{ dB}$ was observed for $8 \mu\text{m}$ wide and $270 \mu\text{m}$ long gold heaters that are 100 nm thick. For several heaters with widths of $6 \mu\text{m}$ and $8 \mu\text{m}$, the impedance as a function of power was measured until the heater failed from thermal stress. The $6 \mu\text{m}$ wide heaters failed at an average of 313 mW (minimum observed power of 288 mW and maximum of 326 mW) and the $8 \mu\text{m}$ wide heaters failed at 386 mW (minimum power of 380 mW and maximum of 394 mW). Data from 5 devices is plotted in Figure 4-6(b). The measured impedance increased linearly with heater power, with slopes of $27.95 \pm 1.91 \Omega/\text{W}$ and $26.01 \pm 1.96 \Omega/\text{W}$ for two devices with $6 \mu\text{m}$ width and $17.70 \pm 2.15 \Omega/\text{W}$ and $18.21 \pm 2.11 \Omega/\text{W}$ for two devices with $8 \mu\text{m}$ width. This data is consistent with results from prior studies of thermal tuners on

silicon nitride platforms [143].

Owing to the direct-write nature of this process, we were able to optimize many passive photonic components by writing large arrays of devices that would have exceeded typical area restrictions imposed by standard photolithography reticles. For example, a 13×13 grid of grating coupler structures with different periods and dutycycles were fabricated simultaneously, then measured on a custom-built automated test stage. Values of the period and dutycycle were chosen that simultaneously minimized the insertion loss and maximized the 3 dB bandwidth at 1550 nm wavelength. Other passive structures, such as arrays of directional couplers, multimode interferometers, 1×2 power splitters, 99:1 taps, and strip-to-slot waveguide mode converters were fabricated, measured, and put into an internal library of validated components.

4.4 Economic analysis and fab-metrics

In recent years, a large number of commercial foundry services (> 25 services) have emerged with multi-project wafer offerings for silicon, silicon nitride, and indium phosphide integrated photonics [93,169]. These services offer access to mature fabrication process flows and allow members of the community to focus on new markets and the design of novel products using these platforms. Despite this, many people and companies continue to implement custom processes for reasons related to intellectual property reasons, process flexibility (adding/removing specific fabrication steps), and cost. To evaluate the merits of implementing a custom process in a university environment, such as the one described in this work, we analyzed the cost per unit chip area as a function of volume. The sum cost of implementing the process for a single wafer and a default 8 hour electron beam lithography write is shown in Table 4.1. Using tool access rates [4], a single wafer costs \$2909 (\$11636 for non-academic users) and each additional wafer after this costs \$1908.3 (\$7633.2 for non-academic users). As the number of desired chips increases, the cost decreases linearly since more of the wafer is being used at the same fixed fabrication rate, as shown in Figure 4-7. At approximately 100 chips (assuming 5×5 mm² area) the price becomes dominated by the

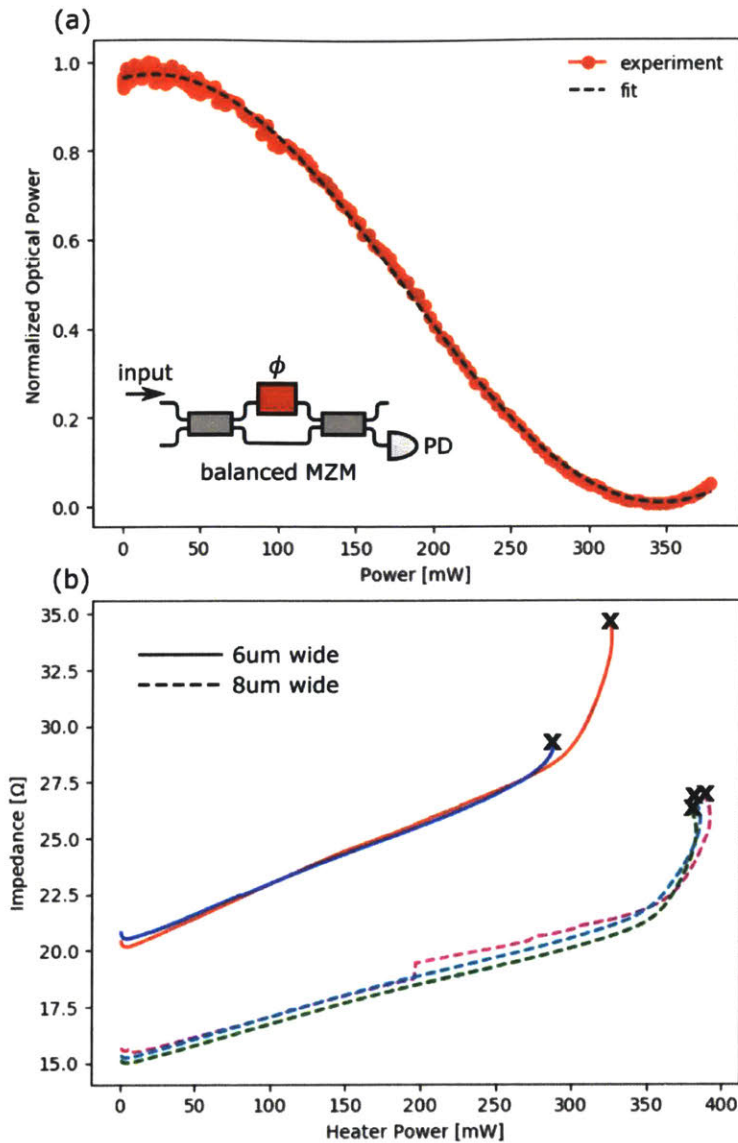


Figure 4-6: (a) Experimentally measured transmission through a balanced Mach-Zehnder modulator (MZM) as a function of heater power at a wavelength of 1550 nm. (b) Measured heater impedance as a function of drive power up until failure (marked by 'X') for two different heater widths.

fill fraction of the photonics layer written via ebeam lithography. The discontinuities seen in Figure 4-7 are a result of adding an additional wafer to the fabrication lot. From this chart, in house fabrication of chips at volumes of 10 – 100 are accessible at 1 – 10 $\$/\text{mm}^2$ cost per area, depending on the amount of ebeam lithography used and neglecting human labor costs.

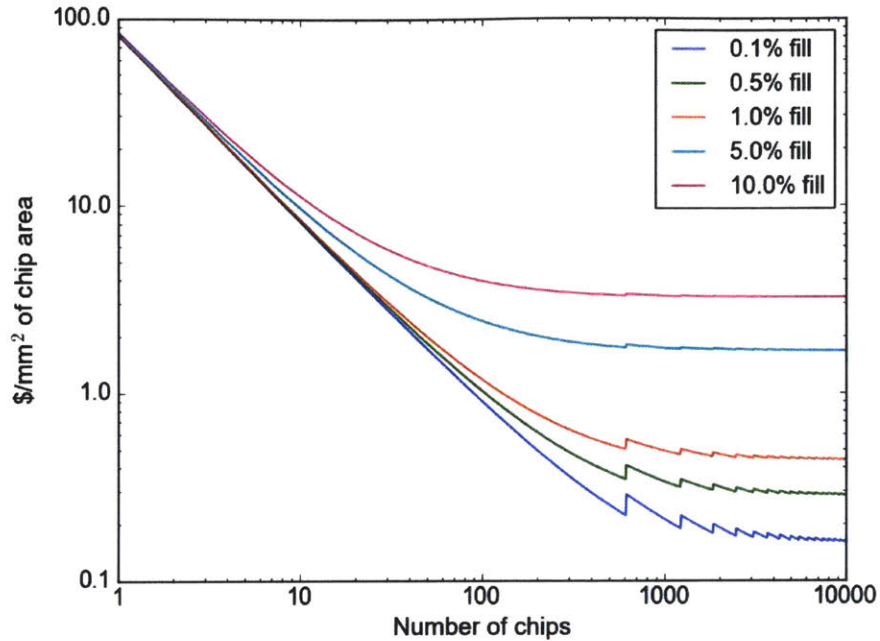


Figure 4-7: Economy of scale (cost per unit area) for the MIT silicon nitride integrated photonics platform, as a function of the waveguide layer fill-fraction. We assume a chip size of $5 \times 5 \text{ mm}^2$ and 150 mm^2 wafers. The electron-beam lithography write speed [minutes/cm²] was empirically found to obey $1672.9 \cdot \text{FF} + 3.08735$, where FF is the pattern fill-fraction. At sufficiently high chip volumes, cost from electron-beam lithography dominates. Discontinuities at increasing number of chips indicate incremental increases in the number of wafers required for fabrication, at which cost initially jumps up due to the sparse number of chips on the newly added wafer.

Another aspect that is critical to prototype development is the fabrication turnaround time, which directly correlates to productivity. In a university environment, significant delays to ideal processing times can occur for a variety of reasons: (1) operator error, where an incorrect step is executed or an accident occurs, (2) tool malfunction, where the tool is operational but performs the process step incorrectly or executes the task in a sub-optimal way, and (3) tool downtime, when the tool is taken offline for repairs, upgrades, or maintenance. We consider only the third type of processing delay since this is logged via reporting data from Coral, the MTL lab management system. Tool data was extracted from a time period of January 2011 through October 2015 and cleaned up so durations that the tools are unusable are properly marked.

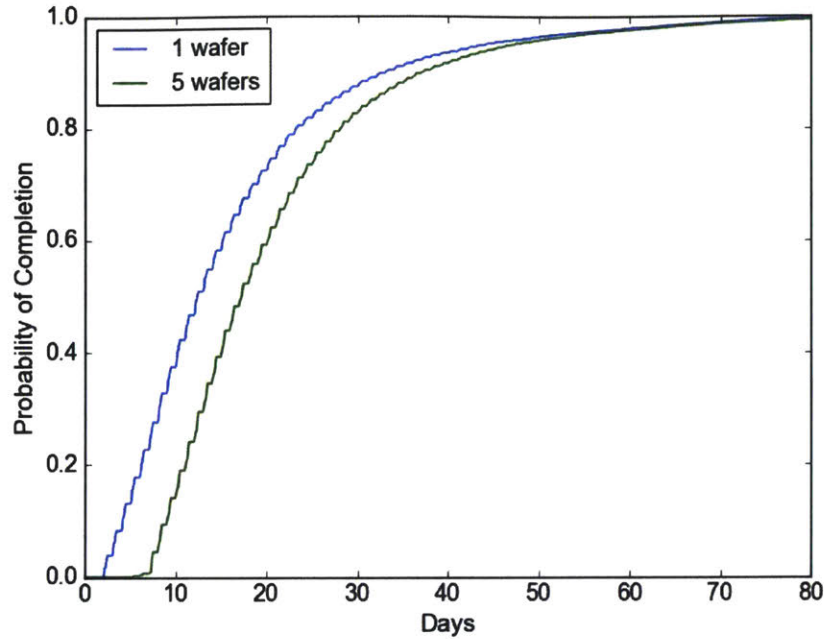


Figure 4-8: Probability of completing a full fabrication process as a function of work-days. The expected time for completion of a process with 1 wafer is 16.4 days with a 10% probability of finishing in 4.1 days and 90% in 33.1 days. For 5 wafers the expected completion time is 21.0 days with a 10% probability of finishing in 9.0 days and 90% in 37.3 days.

We then perform a simulation that steps through the process flow depicted in Table 4.1 and randomly chooses a weekday and time to see if the tool is available. If not, the number of days this tool is down for is added to the processing time. A large number of simulations (2000) are performed to determine better statistical averages of the expected time to completion. We do note several assumptions of this approach: we assume there is no scheduling conflicts with other tool users (i.e. the tools are reserved sufficiently far in advance), we don't consider broken or lost wafers as a result of tool failure (which would necessitate restarting a process from the beginning), and the approach does not account for correlated events like power outages across the building. The results of this analysis are shown in Figure 4-8 and indicate an expected completion time for 1 wafer of 16.4 days, and 21.0 days for 5 wafers.

4.5 Conclusion

In this work, we describe a complete process flow using direct-write lithography for quickly and inexpensively fabricating silicon nitride integrated photonic devices. Utilizing a single process flow, low loss (0.36 ± 0.11 dB/cm) waveguides and passive components were developed for applications at both traditional telecommunication wavelengths and near-visible wavelengths for sensing and spectroscopy. With opened sensing windows, thermal phase tuners, and etched edge couplers, it is possible to realize fully-packaged photonic devices for a large range of applications. We outline specific details of the process necessary for reproducing the entire fabrication process and perform an economic analysis that suggests this approach is cost competitive with commercial multi-project wafer services (in the context of prototype development). We hope this work will enable future researchers to rapidly develop new and exciting photonic devices and systems.

Chapter 5

A packaged, fiber-coupled waveguide-enhanced Raman spectroscopic sensor^{*}

Overview

Waveguide-enhanced Raman spectroscopy (WERS) is a promising technique for sensitive and selective detection of chemicals in a compact chip-scale platform. Coupling light on and off the sensor chip with fibers however presents challenges because of the fluorescence and Raman background generated by the pump light in the fibers, and as a result all WERS demonstrations to date have used free-space coupling via lenses. We report a packaged, fiber-bonded WERS chip that filters the background on-chip through collection of the backscattered Raman light. The packaged sensor is integrated in a ruggedized flow cell for easy measurement over arbitrary integration times. We also derive the figures of merit for WERS sensing with the backscattered Raman signal and compare waveguide geometries with respect to their filtering performance and signal collection efficiency.

5.1 Introduction

Integrated waveguide Raman sensors have attracted significant interest notably for their compact size and large interaction volume that scales with the waveguide length. High-index contrast, dielectric waveguides enable efficient excitation via evanescent modal fields. Raman scattered light is coupled back into these waveguides and sent to a spectrometer for chemical analysis. Prior work has demonstrated the validity and promise of this sensing technique using various waveguide material platforms including silicon nitride (Si_3N_4), alumina (Al_2O_3), Ta_2O_5 , and TiO_2 [40, 48, 50, 62, 79, 152,

^{*}This chapter is based on: D. M. Kita, J. Michon, J. Hu, “A fully packaged, fiber-coupled waveguide-enhanced Raman spectroscopic sensor” (*manuscript currently in review*).

153, 180, 203]. Unfortunately, not all system components can be easily integrated on a single chip, since WERS requires high-power monochromatic light sources at visible or near-infrared wavelengths, high-extinction ratio filters, and sensitive detectors. As a result, waveguide-enhanced Raman sensors are currently only functional when coupled with off-chip components. Demonstrations of WERS to date have all utilized free-space, high-numerical-aperture (high-NA) objectives to couple light on and off chip. While this technique provides good coupling efficiencies, the need for expensive alignment stages and vibration sensitivity of these setups prevents them from being practical for field testing. Coupling light to Raman chips with optical fibers is the straightforward solution to this problem, yet the Raman pump signal generates unwanted fluorescence and Raman background in the input and output fibers [181].

In this work, we describe a scheme for collecting backscattered light using a simple on-chip beamsplitter and two long spiral waveguide sections. This method has two advantages over prior demonstrations that involve sensing from forward-scattered Raman light (despite imposing additional 3 dB loss from the beam splitter): (1) the pump and fiber Raman/fluorescence background predominantly propagate in the forward direction whereas half of the Raman signal coupled into the waveguide is backward-propagating (with the same intensity as the forward-propagating signal), giving rise to an improved signal-to-noise ratio; and (2) there is no optimal waveguide length proportional to $1/\alpha_s$ (the scattering losses) – rather the waveguide sensing region should be as long as possible to maximize the signal.

In the following, we first present a silicon nitride photonic integrated circuit with exposed sensing windows that operates based on this technique. Fibers are bonded to both input and output of the chip and a custom, ruggedized enclosure is machined to allow in-line measurements of arbitrary liquid or gaseous chemicals. We then analyze the efficiency of this technique for filtering out pump signal and fiber background, which is directly related to the ratio of reflected light and the light scattered into the far-field, as described in Section 5.4. Finally, in Section 5.5 we describe several techniques for improving the performance of future Raman sensors.

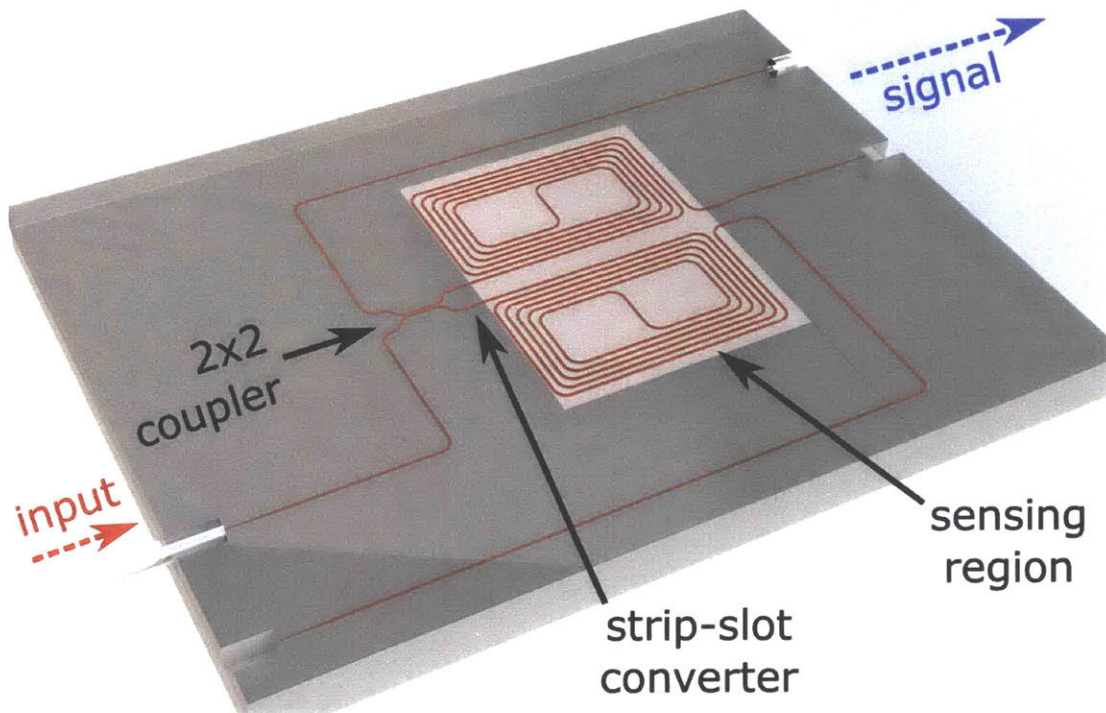


Figure 5-1: Rendering of the photonic chip design fabricated in this work. A 2×2 directional coupler splits light into two waveguide channels, a MMI converter transforms the strip to a slot mode, and then in an exposed sensing region Raman scattered light is coupled into the backward-propagating waveguide mode. Components are not to scale.

5.2 Chip design and fabrication

The silicon nitride photonic sensor was made using a custom fabrication process at the MIT Microsystems Technology Laboratory. The final layer stack of the device consists of a $3 \mu\text{m}$ bottom thermal oxide, a 200 nm thick LPCVD silicon nitride waveguide layer, and a $2 \mu\text{m}$ TEOS SiO_2 top cladding. The ridge waveguide is partially etched such that $\sim 35 \text{ nm}$ of silicon nitride remains. This thin layer acts as a wet etch stop when opening sensing windows with buffered oxide etch. A deep oxide etch step ($5 \mu\text{m}$ depth) defines facets for edge coupling a flat cleaved single mode fiber (Nufern 780-HP) to the waveguides, and a deep reactive ion etch step ($150 \mu\text{m}$ depth) removes enough substrate so the fiber can access the facet.

On the chip (see Fig. 5-1), $100 \mu\text{m}$ long inverse spot-size converters with 75 nm wide tips expand the waveguide mode to allow for more efficient fiber coupling (with a

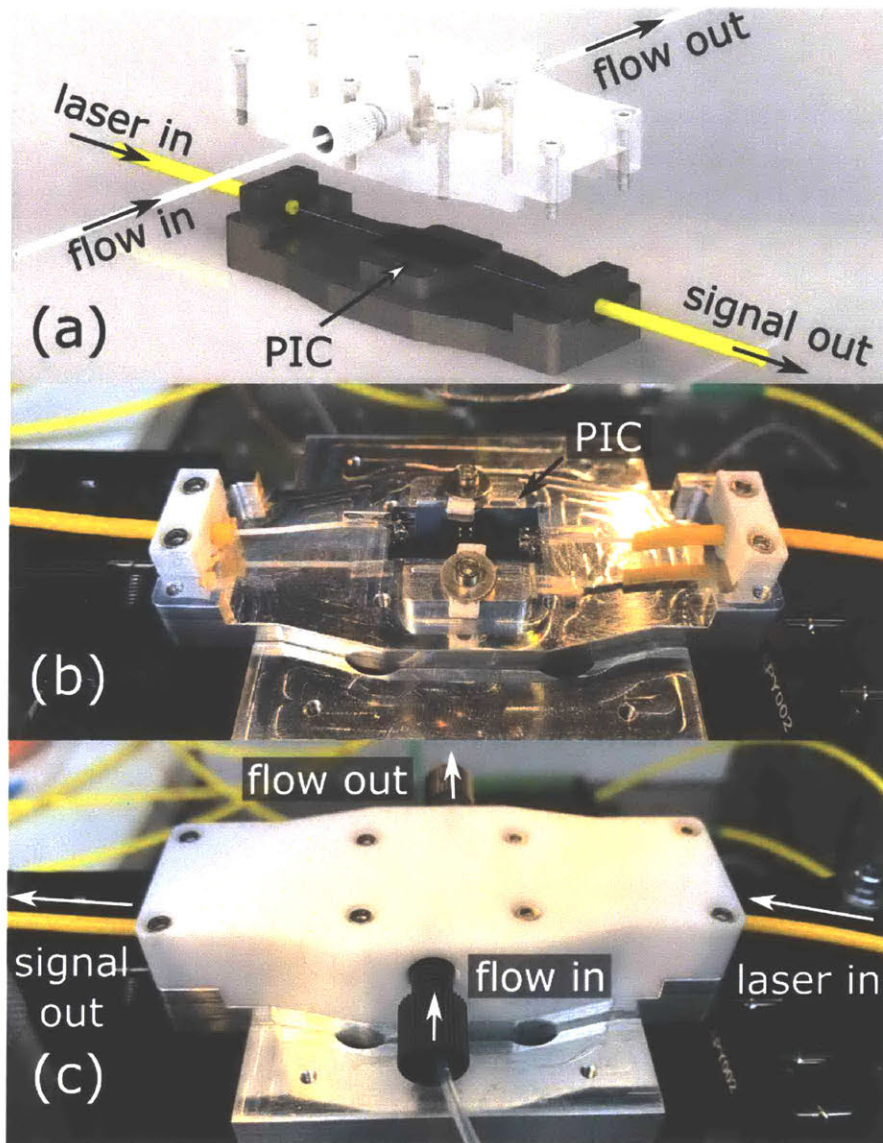


Figure 5-2: (a) Rendering of the chip enclosure with optical fibers affixed to the chip and a flow cell that lowers onto the surface of the chip. The top case and flow channels are machined from PTFE, a rubber Kalrez[®] O-ring separates the chip from the top case, and the bottom fixture is machined from aluminum. (b) Photograph of the fiber-coupled, packaged Raman sensing chip with fibers glued to the edge of the chip after being mounted in separate glass v-groove chips (for mounting purposes). (c) The packaged chip with the top PTFE cell secured above the chip.

theoretical -3.0 dB/facet insertion loss, and a measured loss of -7.2 dB/facet). The single mode waveguides are 500 nm wide, and a 2×2 coupler (20 μ m long, 0.4 μ m gap) is used to split light into two arms. A multi-mode interferometer (MMI) with 2.7 μ m

$\times 1.5 \mu\text{m}$ dimensions is used to convert the TE polarized strip mode to a TE polarized slot mode [44]. The slot waveguide consists of two 350 nm rails and a 100 nm slot gap. These waveguides then enter the spiral waveguide sensing region which is 8 cm long and consists of 100 μm radius bends. Backward-propagating Raman generated light travels back to the 2×2 coupler where approximately half of the light is carried to an output port at the opposite edge of the chip as the input.

In order to bond optical fibers to the edge of the chip, we first begin by mounting each fiber into a glass V-groove block (OZ Optics) such that the fiber tip extends ~ 0.5 mm beyond the glass block and then we bond the fiber and V-groove block with UV curable epoxy. Next, the fibers and the chip are each mounted in custom 3D-printed arms that attach to 5-axis positioning stages for both input and output alignment. Our process for applying epoxy to each fiber consists of first touching the tip of each fiber to a small droplet of epoxy under a microscope and then gently retracting the fiber so that only a very small amount of transparent UV-curable epoxy wets the flat fiber tip area. This process ensures that a minimal volume of epoxy is used during fiber-to-chip bonding, since volume changes during curing (resulting in sub-micron level displacements) can have dramatic, detrimental effects on the coupling efficiency. Once the fibers on both ends are aligned and the power transmitted through the waveguides is optimized, the epoxy is cured. Next, larger volumes of epoxy are applied between the glass block and the silicon nitride photonic chip for mechanical stability.

In order to use the chip for sensing a variety of compounds, including organic solvents like isopropanol or acetone that would readily dissolve the epoxy at the edge of chips, we designed a ruggedized flow cell as shown in Fig. 5-2. The cell consists of a machined aluminum bottom component that the photonic sensor chip sits on top of, a polytetrafluoroethylene (PTFE) top component with drilled holes that form the flow-cell, and a rubber Kalrez[®] O-ring that separates the chip from the top PTFE component. The top and bottom pieces screw tightly together to put pressure on the O-ring and seal off the sensing region. The PTFE top component and rubber O-ring are both chemically resistant to a wide range of organic solvents

and acids and can withstand high temperatures, enabling sensing of liquids in harsh environments (e.g. in flow-chemistry reactions). Using this ruggedized flow cell with our fiber-packaged waveguide-enhanced Raman sensors, we are able to measure a variety of chemical species with arbitrary integration times and without the need for any optical alignment.

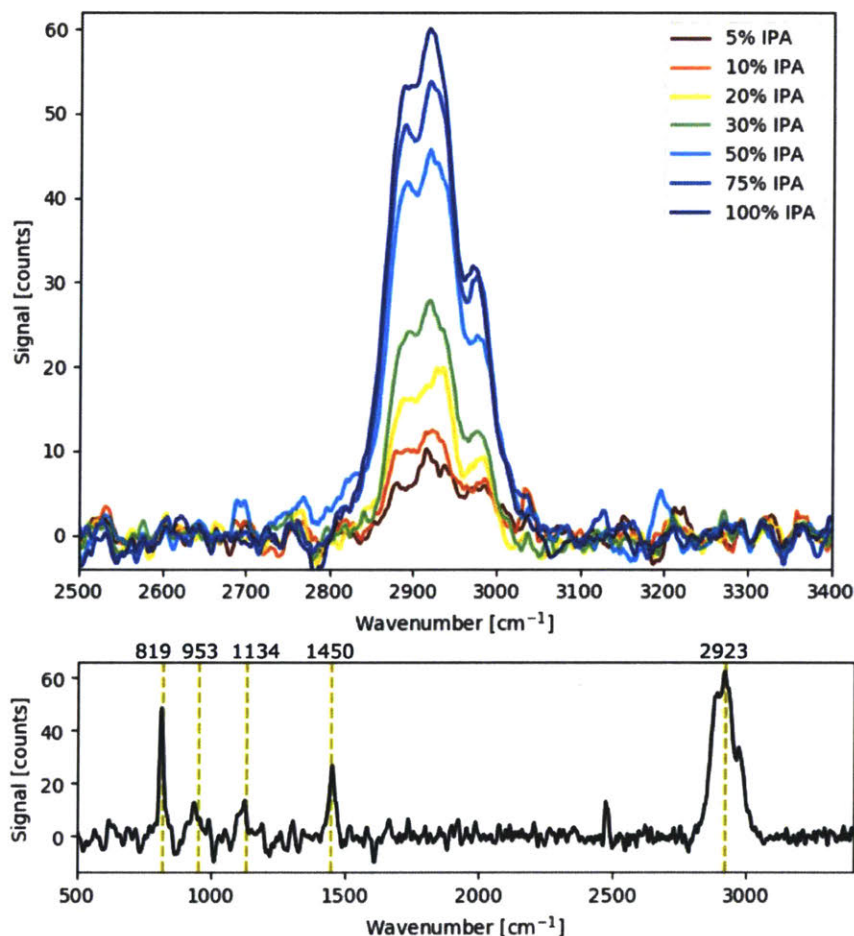


Figure 5-3: (a) Measured Raman spectra of mixtures of isopropyl alcohol (IPA) and water at different weight fractions, post background subtraction and baseline correction. Each spectra is the result of 15×60 second integration times. The standard deviation on each wavelength measurement is approximately 2.9 counts. (b) Full spectrum of the 100% IPA measurement.

5.3 Measurements

The optical measurement setup consists of a wavelength stabilized single mode fiber coupled laser operating at $\lambda = 808 \text{ nm}$ (QFBGLD-808-250, QPhotonics, LLC). A fiber-integrated narrow bandpass filter centered at $\sim 810 \text{ nm}$ is used to remove amplified spontaneous emission from the signal, and polarization control paddles before the chip are used to couple light into either the TE or TM waveguide modes. After the chip, light travels to a fiber bench with a notch filter to prevent any remaining pump light at 808 nm from continuing to the spectrometer. The Raman signal is sent via fiber to a compact commercial spectrometer with a cooled CCD (AvaSpec-HERO, Avantes BV). Although most of the pump light is removed on-chip by the forward-propagating waveguide mode, finite reflections on the chip necessitate the additional notch filter. The optical components that contribute the most reflection are the strip-to-slot waveguide mode converter, the transition from the waveguide being top clad with oxide to top clad with analyte, and the backscattered light from waveguide roughness in the sensing region.

Using a packaged chip with 800 nm wide slot waveguides with 100 nm gap, Raman spectra were obtained for varying concentrations of isopropyl alcohol (IPA) in water, as shown in Fig. 5-3. A separate measurement with only deionized water above the chip was used to subtract any background fluorescence and wavelength dependence of light coming off the chip since reflection at several on-chip components generated weak Fabry-Perot fringes. Due to the wavelength dependence of the directional coupler, we also saw greater signal collection for Raman light at the 2923 cm^{-1} peaks than at peaks between $819\text{-}1450 \text{ cm}^{-1}$. For this device, the ratio of Raman signal from pure IPA above the chip to background fluorescence at 2923 cm^{-1} was $58 \pm 4 : 62 \pm 4$ (counts) without any baseline subtraction. In order to extract the additional pump light rejection when collecting backscattered Raman signal, we measured the forward-scattered Raman signal from a separate 5 mm long straight slot waveguide. In this configuration, the strong background fluorescence and Raman generated in the fiber (with an amplitude of 898 ± 73 counts) prevented direct identification of the IPA peaks.

Only when subtracting a baseline measurement performed with no analyte could the Raman peaks at 2923 cm^{-1} be identified, with an amplitude of 143 ± 31 counts. The difference in signal-to-background ratio between the forward- and backward-collection configurations indicates an effective on-chip background rejection ratio of 7.7 ± 1.1 dB as a result of collecting the backreflected light. This agrees well with our calculations as it is slightly lower than the theoretical maximum presented in Fig. 5-4(c).

5.4 Analysis of backscattered Raman signal

The signal of interest in this sensing scheme is the power of backward-propagating Raman light collected at the start of the sensing region ($x = 0$) normalized by the input forward-propagating pump light (also at $x = 0$). Assuming the vast majority of Raman scattered light comes from the forward-propagating pump with power P_f (compared to the backward-reflected pump signal power), and the magnitude of the Raman scattered light is significantly less than the pump light, the rate equations describing the Raman power P_{Raman} are:

$$\frac{dP_f(x)}{dx} = -\alpha_s P_f(x) \quad (5.1)$$

$$\frac{dP_{\text{Raman}}(x)}{dx} = -\beta_{\text{Raman}} P_f(x) + \alpha_s P_{\text{Raman}}(x) \quad (5.2)$$

where β_{Raman} is the generation rate of the Raman signal and α_s is the scattering loss per unit length. Solving these coupled differential equations and setting the powers to zero as $x \rightarrow \infty$, the ratio of Raman power to input power is:

$$P_{\text{Raman}} = \frac{\beta_{\text{Raman}}}{2\alpha_s} P_f(0). \quad (5.3)$$

The optimized Raman signal is similar to that derived for the forward-scattered light collection scheme, which yields $P_{\text{Raman}}(z_{\text{max}}) = (\beta_{\text{Raman}}/\alpha_s)e^{-1}P_f(0)$ where $z_{\text{max}} = 1/\alpha_s$ [95].

An advantage of collecting backscattered Raman light is that the fiber fluorescence

generated by the input fiber and the pump light (that would generate fiber fluorescence in the output fiber) should couple only weakly to the backward-propagating mode. The corresponding rejection ratio is thus determined by the amount of reflected light on the chip. Assuming very low-loss components with adiabatic mode transformations, the dominant source of back reflection is scattering from sidewall roughness α_r . This, along with the scattering loss (power scattered only into the far field) α_l determines the distance that light propagates into the sensing region. The rate equations determining the pump power in the forward-propagating mode P_f and the pump power in the backward-propagating mode P_b are given by:

$$\frac{dP_f(x)}{dx} = -\alpha_l P_f(x) - \alpha_r P_f(x) + \alpha_r P_b(x) \quad (5.4)$$

$$\frac{dP_b(x)}{dx} = \alpha_l P_b(x) + \alpha_r P_b(x) - \alpha_r P_f(x) \quad (5.5)$$

Similar to Eqs. (5.1)–(5.2), solving these coupled equations with the boundary conditions

$\lim_{x \rightarrow \infty} P_f(x) = 0$ and $\lim_{x \rightarrow \infty} P_b(x) = 0$ yields a relationship between the input power $P_f(0)$ and the output reflected power $P_b(0)$:

$$P_b(0) = \left[1 + f - \sqrt{2f + f^2} \right] P_f(0) \equiv \eta P_f(0) \quad (5.6)$$

where $f = \alpha_l/\alpha_r$ is the ratio of scattered power loss to reflected power, and η quantifies the rejection ratio. Since η depends only on the ratio f , and α_r and α_l are both proportional to the net waveguide scattering loss α_s , the rejection ratio is a function of the local density of states at the scattering center [136]. Assuming that waveguide sidewall roughness is the dominant scattering mechanism and the roughness correlation length is significantly larger than the RMS roughness amplitude, we use the volume-current method [95] to numerically compute α_l , α_r , and f for a variety of TE and TM strip waveguide modes and 800 nm wide slot waveguides with varying slot gaps at $\lambda = 808$ nm. The results of this analysis are shown in Fig. 5-4, and suggest that TM strip waveguides offer the best tradeoff between Raman gain and scattering

loss ($\beta_{\text{Raman}}/\alpha_s$). Despite enhanced field confinement in the top cladding for narrow gap slot waveguides, the field enhancement in the relatively low index contrast structure ($n_{\text{clad}} = 1.329$, $n_{\text{Si}_3\text{N}_4} = 2.02$) is not enough to overcome the higher losses as a result of the additional sidewall interface. In addition, TM strip waveguides were observed to have nearly 10 \times better pump rejection ratios than TE structures because scattered power is more likely to couple back into the fundamental TE mode than the TM mode.

5.5 Conclusion

Using a fiber-coupled silicon nitride WERS sensor designed to collect only the backreflected Raman light, we demonstrate a functional, robust sensing device that circumvents the issue of fiber fluorescence/Raman background. The machined enclosure with integrated flow cell enabled measurements of IPA in water down to single-digit weight percentages. A key advantage of this technique is that it allows for up to ~ 20 dB of fiber background suppression and there is no fabrication-dependent optimal waveguide length for the spiral waveguide sensor. Furthermore, our volume-current method analysis suggests that narrow gap structures (like slot waveguides) may not yield better waveguide sensors, although a more complete analysis that includes the background fluorescence generated from the waveguide core is required [49, 103].

A number of improvements to future device designs can significantly improve the signal-to-noise ratio for high-performance Raman sensing applications. First, improving the coupling efficiency to the waveguides with better inverse taper couplers and better packaging techniques will yield higher Raman signals. Second, eliminating all components that contribute to back-reflection will reduce the transmitted pump light and fiber background. This can be accomplished by replacing the MMI-based strip to slot waveguide converter with an adiabatic mode converter. Also, reflections at the interface between the buried waveguide and the exposed sensing waveguide can be reduced by letting the waveguide enter the sensing region at a shallow angle (rather than at a normal angle). Third, replacing the directional coupler with either a broadband

adiabatic coupler or wavelength-selective filters [131, 135, 181] would both improve the flatness of the received Raman signal and could eliminate the 3 dB insertion loss penalty. Finally, careful design of the waveguide geometry in the sensing region can improve the output signal, decrease losses (thereby increasing the interaction volume), and more efficiently filter out the pump source.

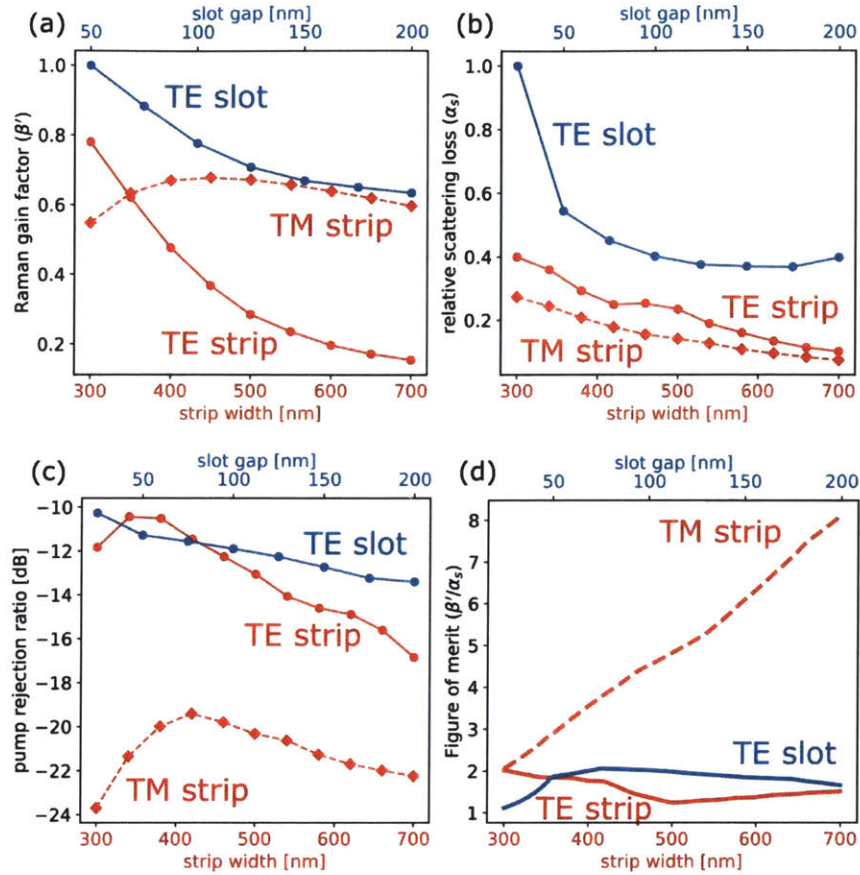


Figure 5-4: Numerically computed values of (a) the relative Raman gain coefficients (normalized by the 50 nm TE slot value) computed via field integrals over the top clad (sensing) region, assuming water as the solvent, (b) the scattering loss α_s computed via the volume-current method, (c) the pump rejection ratio $10 \log_{10}(\eta)$, where η is given by Eq. (5.6), and (d) the Raman sensing figure of merit $\beta'_{\text{Raman}}/\alpha_s$ with data interpolated from (a) and (b). Slot waveguides are all 800 nm wide (from one outer edge to the other).

Chapter 6

Conclusion & future directions

The only reason for time is so that everything doesn't happen at once.

Albert Einstein

The previous chapters discussed advances in on-chip spectroscopy, roughness scattering loss calculations for sensing performance estimation, a silicon nitride photonics platform for fabricating photonic sensors, and a demonstration of a fully packaged waveguide enhanced Raman spectroscopic sensor. Each of these individual chapters aims to advance on-chip spectroscopic sensing so that the community might ultimately realize a compact, highly integrated photonic sensing system.

There is still much work to be done before photonic sensors are to be commercialized at high volumes. The following sections are devoted to my perspectives on future areas of research in the field of photonic sensors and spectrometers. First, Section 6.1 describes outstanding challenges in photonic sensing, and then the sections following this outline a variety of future directions and perspectives on the work presented in Chapters 2-5 of this thesis.

6.1 Broader challenges

As discussed in the Chapter 1, practical implementations of integrated photonic sensors require three critical elements: (1) a light source for the sensing mechanism, (2) a means by which light can interact with the chemical of interest, and (3) optical read-out with a single element detector or spectrometer. Many interesting and practical

systems can be realized by integrating one or two of the aforementioned elements on a single chip (the rest being coupled to the chip with free space optical elements or fibers). There are many interesting, potentially high-volume applications that would require these systems to be low-cost, have low-power consumption, and be readily manufacturable at high volumes. Thus, a grand challenge in photonic chemical sensing is to monolithically integrate all components on a single semiconductor substrate, or multiple chips optically connected without any free space lenses or fibers (edge coupled to one another, connected with an interposer chip, or die-to-wafer bonded). Monolithic integration would enable truly compact, chip-sized systems to be realized, and would result in large decreases to module cost as fiber packaging and assembly is currently a relatively large fraction of the total module cost.

Source integration is a significant challenge for realizing integrated chemical sensors. Especially for absorption spectroscopy where a broadband source is required, it can be difficult to find a suitable spatially coherent light source to couple into a waveguide and accommodate sensing at specific wavelengths of interest. Since single mode waveguides tend to have relatively narrow optical bandwidths, devices tend to cover only a small fraction of the ‘fingerprint region’. Raman spectroscopy is a promising approach since it requires only a single frequency light source, and Raman shifts spanning the entire fingerprint region can be easily coupled back to a single mode waveguide. There is exciting work to be done in integrating sufficiently high-power light sources at near visible wavelengths with practical photonic platforms like silicon nitride. Although light sources have not been discussed in the context of this thesis, advances in this area will yield many opportunities for future photonic sensors.

Evanescent field sensing, despite its promise of significantly increasing the interaction volume of light with the analyte in the top cladding, is sensitive to contamination from ‘dirty’ real world environments. When the top-surface is exposed to the environment, small amounts of contamination from unwanted residue and particulates can attach to the waveguide and cause significant light scattering that rapidly attenuates the signal of interest. Either the chemicals in the top cladding must be very pure and particulate-free (as is the case in some applications like pharmaceutical ingredient

synthesis), or a porous material be applied above the waveguide to ensure that only chemicals (and not particulates) reach the sensitive waveguide layer.

Finally, waveguide integrated Fourier transform spectrometers are promising for high-resolution spectrum analysis, but the two primary challenges are realizing high-speed, low-loss optical switches and efficiently coupling light into the chip. Current thermo-optic modulators are convenient due to their small chip footprint and low insertion loss, but their switching speed is limited by the thermal time constant which is typically ~ 100 kHz in silicon-on-insulator platforms. Electro-optic techniques can enable switching at GHz speeds but consume a large chip footprint and have relatively high insertion losses. In terms of practical sensing applications, coupling light onto the chip with high efficiency is another challenge. On-chip spectrometers are therefore likely to find use in applications where light is already confined to a single mode fiber or waveguide (such as for evanescent field sensing, or for characterizing WDM signals).

The next few sections are devoted to potential future improvements to on-chip Fourier transform spectrometers and on-chip Raman spectroscopy.

6.2 Ultra high channel-count Fourier transform spectrometers

As mentioned in Chapter 2, chip-scale Fourier transform spectrometers fabricated monolithically in silicon are lightweight, robust, and potentially high-performance alternatives to larger free-space optical spectrum analyzers. However, in order to achieve comparable performance to free-space instruments, on-chip devices must be capable of: high spectral channel count (> 1000 's of spectral channels), large optical path length differences, a large interferometer visibility (which sets the instrument's dynamic range), and large spectral bandwidth. Given the attractive scaling laws described by Equations 2.1 and 2.2, it would seem rather straightforward to simply design another set of identical devices with additional optical switches. In fact, by increasing the total channel count via modest increases in switch numbers, the

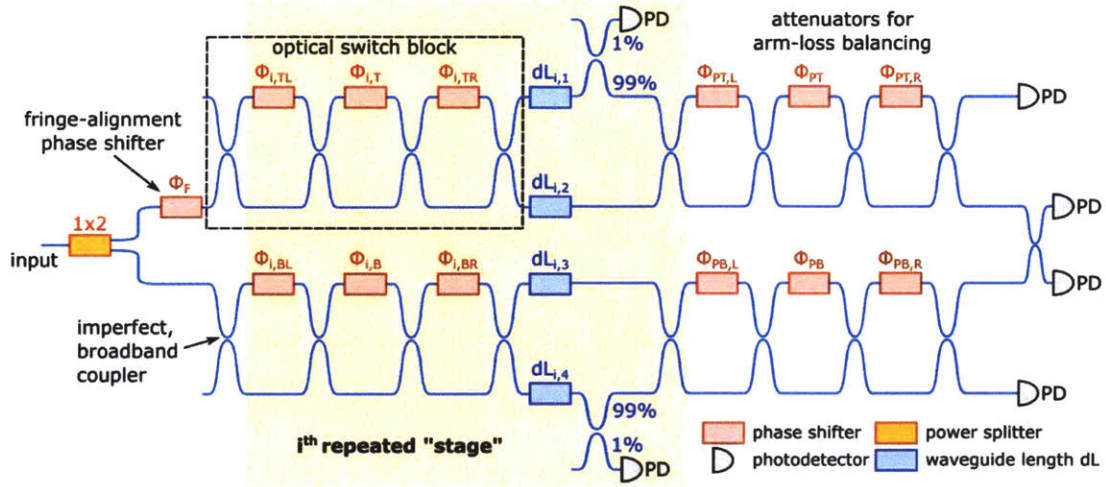


Figure 6-1: Overview of potential improvements to the reconfigurable Fourier-transform spectrometer concept. Figure reproduced with permission from Kita, *et al* [96]

calibration matrix A becomes more square and there is less need for regularized regression methods. Further additions to the spectrometer architecture, as detailed in Figure 6-1, can be made to improve the performance and ease-of-control for future reconfigurable spectrometers over the previous 6-stage Fourier transform spectrometer. Prototype chips with the improvements described in the following sections (except the ‘perfect’ optical switches) have been fabricated and packaged, and are shown in Figure 6-2.

6.2.1 Perfect optical switching

Traditional photonic optical switches utilize a Mach-Zehnder interferometer (MZI) consisting of a phase shifting element and two directional couplers which are assumed to have a perfect power splitting ratio. In practice, fabrication imperfections make it difficult to achieve true 50:50 splitting using waveguide directional couplers. These optical switches are the fundamental building block of the dFT spectrometer architecture, and imperfect switching results in light leakage onto undesired waveguide paths and problematic multi-path interference effects. A double Mach-Zehnder interferometer configuration, as proposed by Miller [124], can allow for dynamic tuning of the

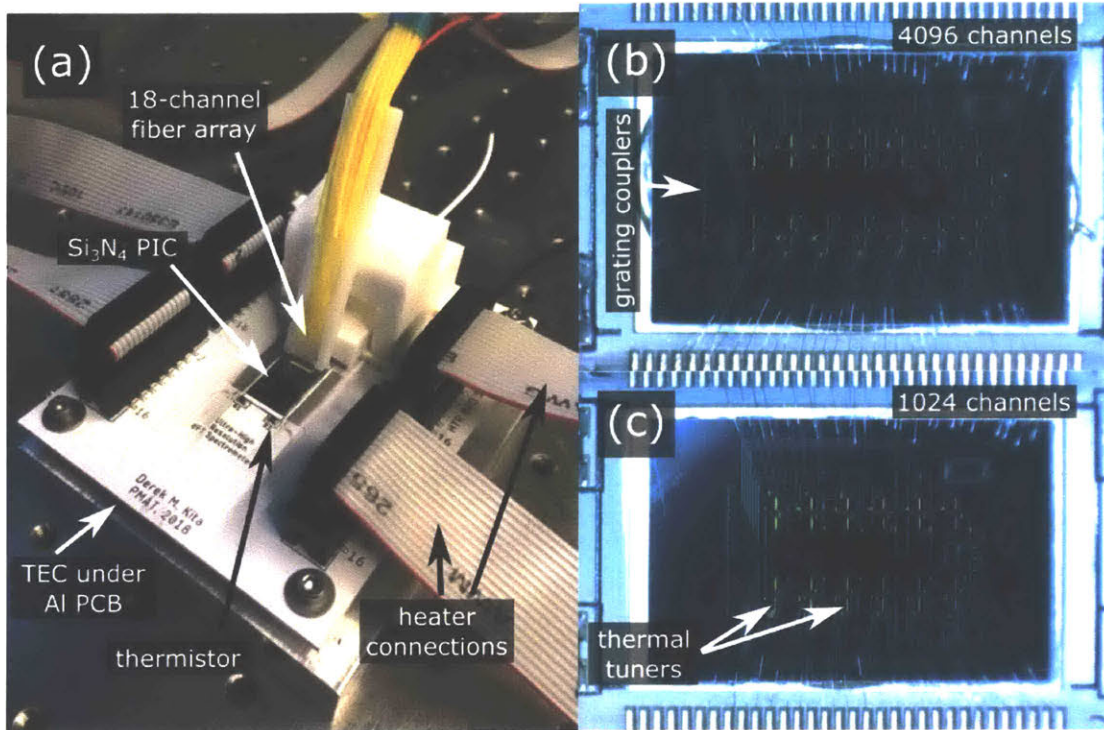


Figure 6-2: (a) Image of a fiber bonded and electrically wirebonded silicon nitride dFT spectrometer PIC. Images (b) and (c) depict 12- and 10-switch dFT spectrometers, respectively, with 4096 and 1024 unique optical path length difference permutations.

splitting efficiency. The addition of phase shifting elements before and after a typical MZI provides sufficient degrees of freedom to compensate for imperfect power splitting in each coupler and achieve near-perfect optical switching. Using this approach, 60.5 dB visibility has been experimentally observed in silicon photonic interferometers [190]. Furthermore, with a power monitor on one of the two arms that samples a small fraction of light (such as 1% as shown in Figure 6-1), it is straightforward to calibrate these optical switch blocks with a beam-splitter 50:50 setup algorithm [124].

In order to produce perfect optical switching across a sufficiently large bandwidth for typical applications, it is necessary to implement broadband optical components. Broadband asymmetric directional couplers with > 160 nm bandwidth [176,187] and inverse taper edge couplers provide sufficient means for dramatically increasing the spectral bandwidth of dFT devices, and should be used in future designs.

6.2.2 Spectrally segmented optical switching

Assuming perfect broadband components are implemented, Mach-Zehnder optical switches will still have wavelength dependence directly related to the wavelength λ and the waveguide dispersion. For example, a thermo-optic Mach-Zehnder optical switch with heaters of length L_{htr} will perfectly switch light to one of the two output channels when $\phi = \pi/2 + n\pi$ ($n \in \mathbb{Z}$):

$$\phi = \frac{2\pi\nu}{c_0} \frac{\partial n_{\text{eff}}(\lambda)}{\partial T} \Delta T L_{\text{htr}} \quad (6.1)$$

As a result, there exists some finite bandwidth $\Delta\nu_{\text{switch}}$ over which each of the optical switches have sufficiently high extinction. Within this frequency range, the spectrometer basis vectors (visualized by rows of the calibration matrix A , seen in Figure 2-2) consist of cosines, as expected. Outside of this range, light is not perfectly switched and so the frequency response of the entire device is dominated by interference from the many optical paths. This issue can be remedied by calibrating the phases on the Mach-Zehnder switches for each of m different non-overlapping wavelength ranges, where $m = \Delta\nu/\Delta\nu_{\text{switch}}$. Each broadband spectrum measurement would consist of switching through all $m \cdot 2^j$ interferometer states, and calibration of the device would take m times longer, but would make possible spectrum measurements that span greater than half an octave.

6.2.3 Arm-loss balancing

Even with perfect optical switching, random component losses and waveguide propagation losses add and contribute to different optical powers in the top and bottom dFT interferometer arms. The net effect of this is decreased interferometer visibility, and therefore decreased dynamic range of the spectrometer. In order to compensate for different arm-losses (which vary for each spectrometer switch permutation), we propose the addition of a final optical switch block that can attenuate both arms independently and achieve an interferometer visibility limited only by the accuracy of the phase modulators.

6.2.4 Fringe alignment

The final improvement we present enables selective filtering of large narrowband signals. In many applications of Fourier transform spectroscopy, such as Raman spectroscopy or radio-frequency spectrum analysis, a large amplitude carrier signal or pump laser must be selectively filtered, else noise from this signal will carry-over to other frequency components (an effect referred to as Fellgett's disadvantage). However, with the addition of a phase-shifting element in-line with one or both arms of the dFT interferometer, as shown by the first phase shifter ϕ_f in Figure 6-1, it is possible to actively align the interferometer fringes such that a null coincides with the unwanted frequency at each spectrometer permutation.

6.3 Volume-current method applied to platforms for Raman spectroscopy

In Chapter 3 the volume current method was used to estimate the sidewall roughness induced losses and figure of merit for silicon waveguides. However, as described in Chapter 5 the most common material platform for Raman spectroscopy is silicon nitride. At visible wavelengths, there may be an advantage to using ~ 100 nm thick silicon nitride for sensing applications (compared to 200 nm thick), as this will increase the size of the optical mode and decrease the total sidewall area. In this section, the relative performance of various waveguide structures based on a 100 nm thick silicon nitride platform are quantitatively compared by means of the volume current method. At a wavelength of $\lambda = 808$ nm with water cladding, the following waveguide geometries were found to have well-confined quasi-TE fundamental modes: (1) strip waveguides with width from 800 nm to 2000 nm, (2) slot waveguides with edge-to-edge separation of 1.0, 1.5, and 2.0 μm and slot gaps from 25 nm to 195 nm. Using MPB, eigenmodes for the aforementioned waveguide geometries were solved for and the relative Raman gain factor β was computed via Equation 3.4. In addition, the Raman gain factor for the waveguide core region was computed to estimate the relative

enhancement in background fluorescence and Raman from the core material (using Equation 3.4 with integral over the core, not the clad). All results were normalized by β_{clad} for the 800 nm strip waveguide and are shown in Figure 6-3(a) and (b). A mesh resolution of 256 pixels/ μm was used for all eigenmode calculations. Next, the relative scattering loss (Figure 6-3(c)) was computed by the volume-current method presented in Chapter 3, with an FDTD resolution of 64 pixels/ μm – a value which was found to converge sufficiently for these waveguide geometries. Both the total power loss, as well as the power coupled into the backwards-propagating mode were recorded to extract the pump rejection ratio η (as described in Chapter 5), shown in Figure 6-3(d). Finally, the total Figure of Merit ($\beta'_{\text{clad}}/\alpha_s$) is shown plotted in Figure 6-3(f).

From these results, it is interesting to note that slot waveguides provide very little enhancement in the external Raman gain factor, but do reduce the waveguide-core Raman gain factor, which would reduce the amount of background from Si_3N_4 fluorescence and Raman scattering. However, strip waveguides have significantly lower propagation losses and seem to couple less roughness-scattered light into the backwards propagating mode (resulting in a better pump rejection ratio). For the Figure of Merit $\beta'_{\text{clad}}/\alpha_s$, the widest strip waveguide (width of 2 μm) outperforms nearly all of the slot waveguides by almost 10 \times .

6.4 Fully integrated spontaneous Raman spectroscopy systems

The fully-packaged, waveguide enhanced Raman sensor described in Chapter 5 integrated the evanescent-field sensing element and performed some (not all) of the pump light filtering on-chip. It is worthwhile to consider the opportunities and challenges associated with integrating the light source, filters, and the spectrometer on the same chip as the sensing element. Such a device, if made practical, would eliminate the need for optical packaging and fiber attachment, would greatly reduce the size of the

system, and could lower the power consumption and potentially the cost of the entire sensing module.

One of the primary challenges associated with source integration is filtering out: (1) the relatively strong Raman pump light after the sensing element, (2) the amplified spontaneous emission (ASE) from the laser, and (3) the waveguide background fluorescence. The ideal filter for (1) is a band stop (notch) filter with both high optical transmission at wavelengths far from the pump frequency and a large stop band attenuation. Promising on-chip filters that could be applied to Raman spectroscopy include single- or multi-stage unbalanced Mach-Zehnder interferometers (i.e. lattice filters) with up to 20 dB rejection [181], on-chip high-performance Bragg reflectors up to 65 dB [73], and ring resonators up to 40 dB [194]. Attaining extinction ratios in excess of these values has proven challenging especially for Mach-Zehnder filters since the extinction ratio depends on the 2×2 coupler's splitting efficiency [124, 190], but approaches using coherency-broken Bragg filters are opening the possibility to achieve pump rejection filters with rejection greater than 80 dB [135]. Filtering the ASE on-chip from the laser source is also challenging since the transmission loss at the source wavelength must be high and the rejection must be sufficiently broadband to span the entire fingerprint region (~ 120 THz). One promising technique is to utilize contra-directional grating couplers [128, 129], which have been demonstrated to have -5.6 dB insertion loss at ~ 772 nm wavelength and 68.5 dB extinction when cascaded [131]. Finally, waveguide background fluorescence is another noise source, but it is difficult to remove in the waveguide sensing region without re-evaluating the entire material platform [49, 152]. Nevertheless, moving the filters on-chip and closer to the sensing region will decrease the distance the pump light travels in fibers or the waveguide and will correspondingly decrease the background noise.

Semiconductor light sources for Raman spectroscopy are relatively mature, and one potential route forward is hybrid integration of an AlGaAs/GaAs distributed feedback laser and silicon nitride photonic chip for on-chip filtering and sensing. Such a route would leverage the high-power handling capability and low cost of silicon nitride chips while also using an appropriately mature light source. A significant

challenge would be integrating a low-noise detector at the output for readout of the Raman signal. The detector (or detector array) would need to be extremely sensitive and likely cooled to reduce thermal noise. In addition, the input aperture of the device should be relatively small to prevent cross-talk between the signal of interest and significant levels of stray light which is generated after light is rejected by the on-chip filters or scattered from sidewall roughness and various components on the chip. Finally, thermal cooling and stabilization of both the laser and detector is a substantial challenge to realizing fully integrated, compact devices with low power consumption.

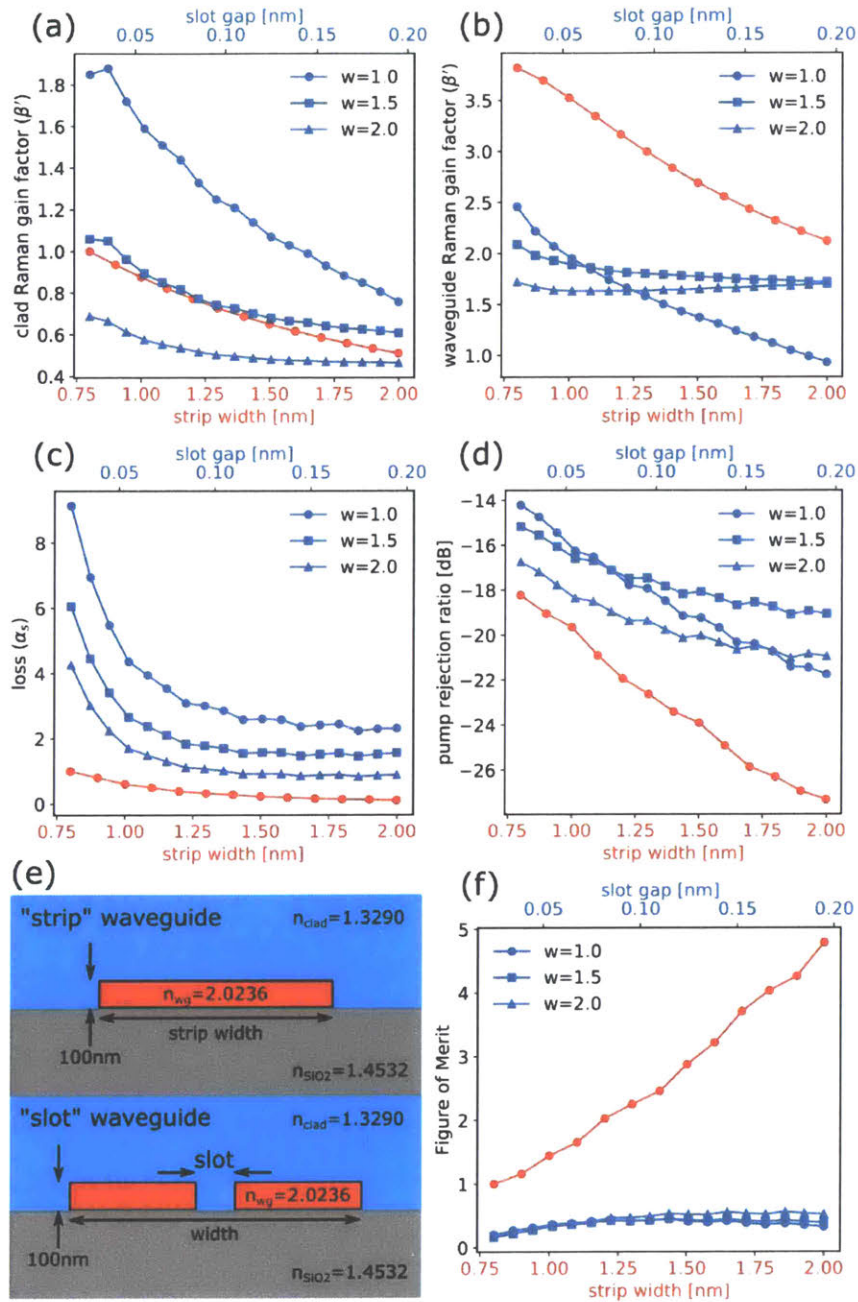


Figure 6-3: Analysis of quasi-TE polarized, 100 nm thick, Si₃N₄ strip and slot waveguides for Raman sensing. Numerically computed values of (a) the Raman gain factor in the cladding, (b) Raman gain factor in the waveguide, (c) scattering loss, (d) pump rejection ratio, and (f) Figure of Merit for 100 nm thick silicon nitride waveguides (strip and slot) clad in water with a pump wavelength of $\lambda = 808$ nm depicted in (e). Volume current method FDTD resolution used is 64 pixels/ μm , and eigenmode solver resolution is 256 pixels/ μm (used both for volume current method and field integrals for the Raman gain factor).

Appendix A

dFT spectrometer characterization and reconstruction methods

A.1 Elastic- D_1 spectral reconstruction method

Given the measured interferogram y (of size $N \times 1$) and a calibration matrix A of size $N \times D$, we seek to accurately reconstruct the input optical signal x that obeys:

$$y = Ax \tag{A.1}$$

where $D \gg N$, and in our case $D = 801$, $N = 64$. For our 64-channel device, there are two types of signals available to us for testing the quality of optical reconstruction: (1) laser lines that are characterized by sparse spectra, and (2) broadband sources (like spontaneous emission from an EDFA) with a broad spectrum (non-sparse). Since the problem we are solving is underconstrained, there are infinite solutions x that solve Equation A.1. However, we can place constraints on the sparsity and magnitude of the spectrum and prevent over-fitting issues by minimizing the L_1 and L_2 norms of x [163]:

$$\min_x \left\{ \|y - Ax\|_2^2 + \alpha_1 \|x\|_1 + \alpha_2 \|x\|_2^2 \right\} \tag{A.2}$$

where α_1 and α_2 are the corresponding hyperparameters. For an arbitrary optical input, we find that the “smoothness” of the spectrum is an important characteristic of the spectra and a good regularizer. To induce the appropriate amount of smoothness, characterized by the first-derivative of the spectrum, we used the finite difference matrix D to define the following regularizer $\|Dx\|_2^2$. We cast our reconstruction problem with L_1 norm, L_2 norm, and the first-derivative smoothness prior as follows:

$$\min_{x, x > 0} \left\{ \|y - Ax\|_2^2 + \alpha_1 \|x\|_1 + \alpha_2 \|x\|_2^2 + \alpha_3 \|Dx\|_2^2 \right\} \quad (\text{A.3})$$

Using $\|Mx\|_2^2 = x^T Mx$, and the fact that our spectrum is non-negative (and thus $\|x\|_2 = 1^T x$), we may rewrite Eq. A.3 as a non-negative quadratic program:

$$\min_{x, x > 0} \left\{ x^T (A^T A + \alpha_2 I + \alpha_3 D^T D)x + (\alpha_2 1 - 2A^T y)^T x \right\} \quad (\text{A.4})$$

The above form is easily computed with standard quadratic program solvers [10]. With this method of solving for the signal x , the last step is to determine the suitable hyperparameters α_1 , α_2 , and α_3 that correspond to the correct input. However, since we don’t have access to the true spectrum, we use a standard holdout cross-validation technique, which requires only two successive measurements of the interferogram, characterized by the same input signal with different noise. The cross-validation technique is as follows: with two independent measurements y_1 and y_2 of the same source, and given two measurements of the basis A_1 and A_2 (performed only once in advance as a calibration step for the spectrometer), we solve for x_1 via Equation A.4 for a suitably large range of hyperparameter values, and arguments y_1 and A_1 . We then choose the spectrum x_1 corresponding to the unique set of α ’s that maximize the coefficient of determination R^2 (see Eq. A.5 below) between the second measurement y_2 and the value $A_2 x_1$:

$$\max_{\alpha_{1,2,3}} \{R^2(y_2, A_2 x_1)\} = \max_{\alpha_{1,2,3}} \left\{ 1 - \frac{\sum_{i=0}^{n-1} (y_{2,i} - (A_2 x_1)_i)^2}{\sum_{i=0}^{n-1} (y_{2,i} - \langle y_2 \rangle)^2} \right\} \quad (\text{A.5})$$

where in the above the subscript i specifies the specific interferogram measurement (out of $n = 64$ total measurements) and angled brackets denote the average value $\langle y_2 \rangle = (1/n) \sum_{i=0}^{n-1} y_i$. The coefficient of determination value of 1 corresponds to a perfect match between inputs, and a value less than 0 means the measurement (y_2) is more accurately fit by a straight line than it is fit by the model ($A_2 x_1$). Maximizing the coefficient of determination above guarantees that our computed spectrum x_1 corresponds to a back-computed interferogram that closely matches a second experimental measurement of the interferogram. This technique allows for the unique determination of a set of hyperparameters that minimize the impact of experimental noise on the spectral reconstruction process. In addition, the hyperparameter search method is trivially parallelizable to systems with multiple processors.

Any regularizer can be used with elastic- D_1 if one can encode this new regularizer with a matrix R and substitute D_1 with R . Thus, our method suggests that any regularizer R can be used to encode any combination of new priors that can be expressed as a matrix. In addition we want to point out the trivial extension to include additional regularizer terms $x^T R_i x$ to elastic- D_1 . This can be easily done by defining the optimization problem

$$\|Ax - y\|_2^2 + \alpha_1 \|x\|_1 + \alpha_2 \|x\|_2^2 + \beta_1 x^T R_1 x + \dots \beta_k x^T R_k x \quad (\text{A.6})$$

with β_i denoting the i -th hyperparameter for each of the k regularizers encoded by the matrix R_i . This can be used to include additional regularizers, and can be solved using hold-out cross validation and with the convex libraries used before. As long as $k = O(1)$, the algorithm will remain polynomial time. In practice, we predict k should be at most 2 or 3. If one adds many more regularizers the algorithm runtime becomes exponential in k . To avoid this one would have to use techniques different from hold-out cross validation.

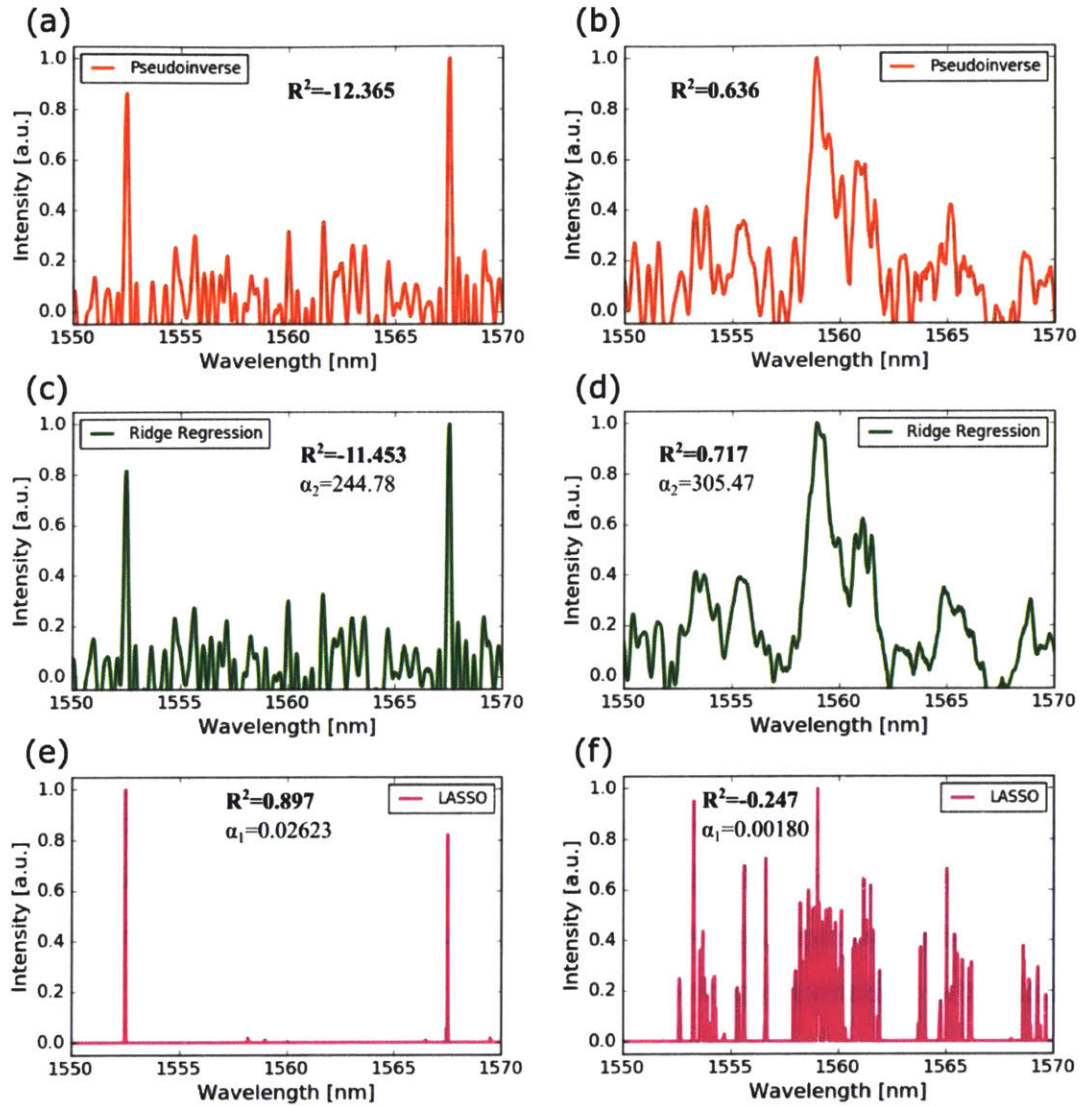


Figure A-1: Comparison of reconstruction techniques. Images of reconstructed spectra for two different optical inputs: two CW laser lines with 15 nm wavelength detuning (a,c,e) (as depicted in Figure 2-3 bottom) and a broadband signal generated by EDFA amplified spontaneous emission (b,d,f) (Figure 2-4c). The reconstruction techniques shown are: pseudoinverse (a,b), ridge regression (c,d), and LASSO (e,f). The R^2 scores and associated hyperparameters (which were selected through cross-validation) are shown as insets.

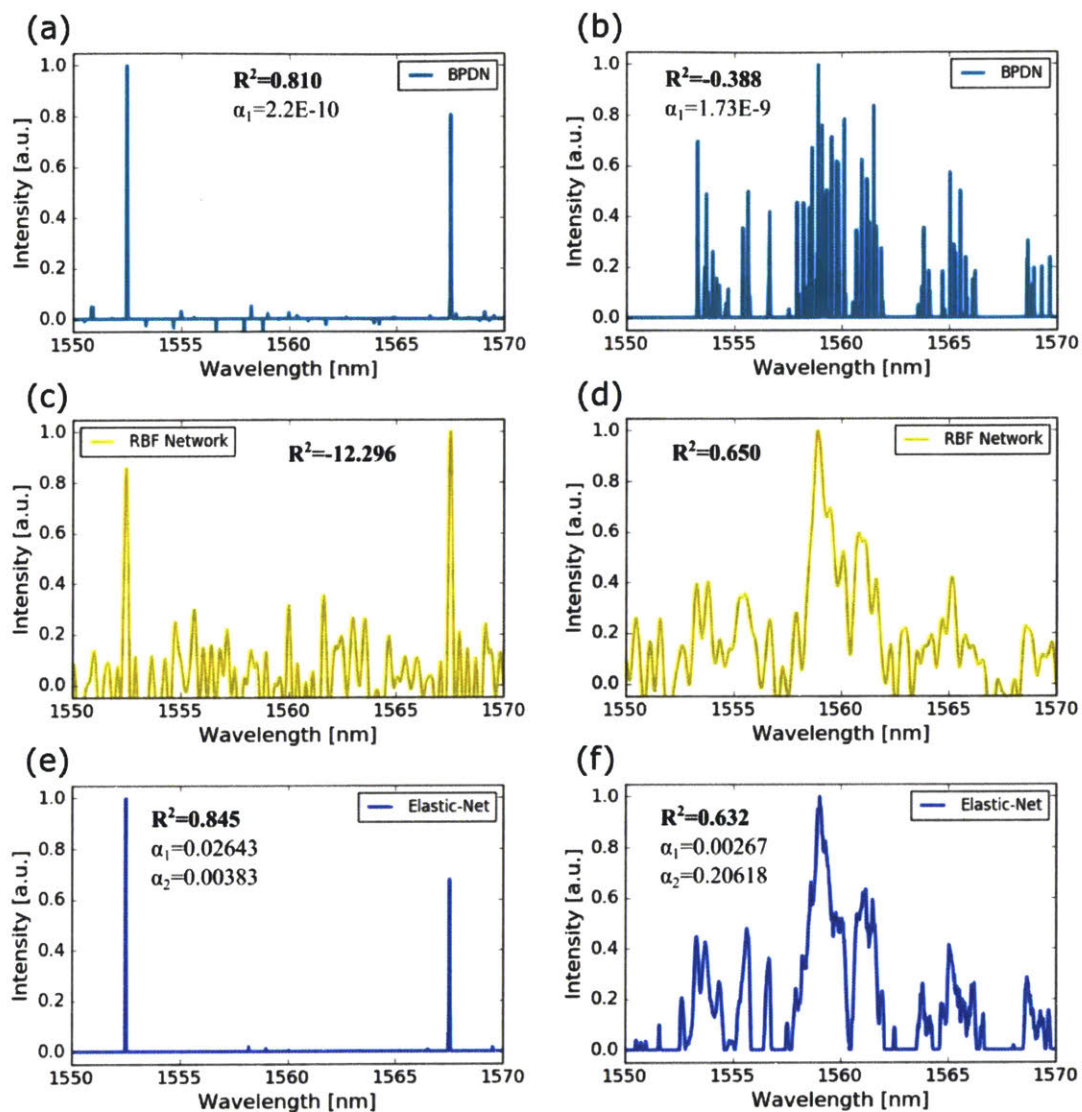


Figure A-2: Comparison of reconstruction techniques. Images of reconstructed spectra for two different optical inputs: two CW laser lines with 15 nm wavelength detuning (a,c,e) (as depicted in Figure 2-3 bottom) and a broadband signal generated by EDFA amplified spontaneous emission (b,d,f) (Figure 2-4c). The reconstruction techniques shown are: BPDN (a,b), RBF Network (c,d), and elastic net (e,f). The R^2 scores and associated hyperparameters (which were selected through cross-validation) are shown as insets.

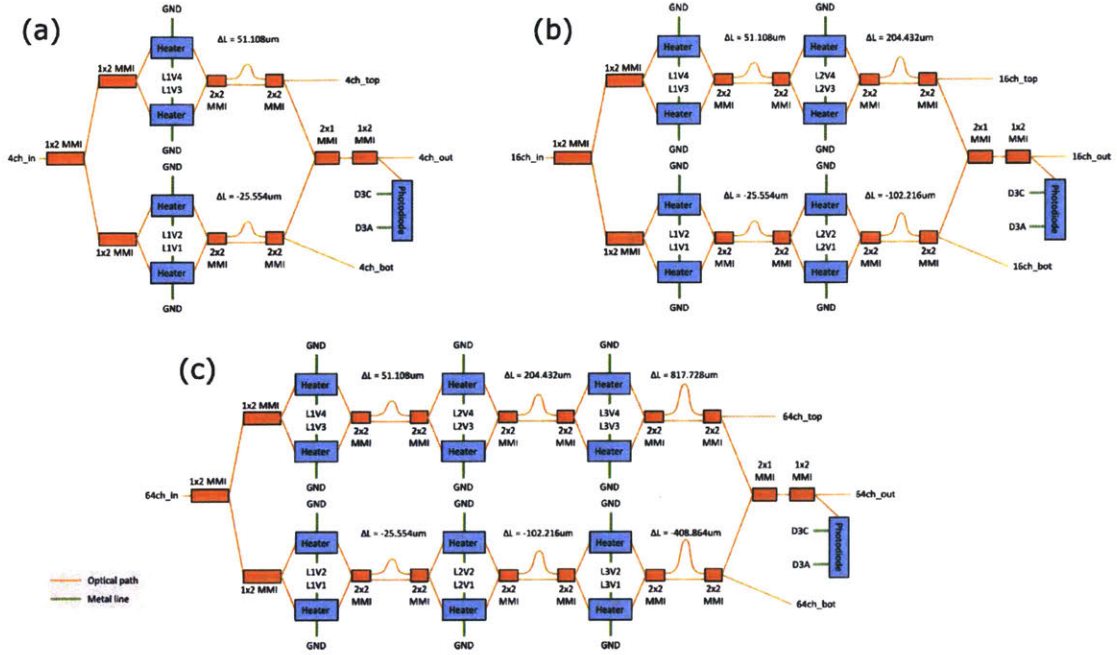


Figure A-3: Schematic of dFT spectrometers. Block diagram of the fabricated 1-stage (a), 2-stage (b), and 3-stage (c) dFT spectrometers fabricated all on a single chip. Orange denotes optical paths and passive optical components, while blue denotes active photonic components (heaters and photodetectors), and green denotes electrical wiring (metal traces).

A.2 Insertion loss measurements of the dFT spectrometers

In order to estimate the total loss of the 64-channel dFT spectrometer, as well as the switching loss per stage, we measured the optical power before and after a set of reference waveguides, as well as dFT structures with 1, 2, and 3 stages (corresponding to 4-channel, 16-channel, and 64-channel dFT spectrometers), as illustrated in Figure A-3.

We determined the polarization-dependent insertion loss of the photonic components as a function of wavelength by scanning a single frequency tunable laser. We first performed a reference measurement of the grating coupler and fiber losses using a loopback waveguide on the chip (two grating couplers connected only by a straight waveguide). The fiber-to-fiber loopback loss was measured at 6.7 ± 0.7 dB across the

1550 – 1570 nm wavelength range. Next, we measured the insertion loss across the 64 channel dFT spectrometer by sending light into port “64ch_in” and measuring the outputs at both top and bottom tap-ports (labelled “64ch_top” and “64ch_bot” in Figure A-3c. When the spectrometer is powered on, the top and bottom tap-ports have a relatively flat spectral response (in contrast to the “64ch_out” port, which exhibits the distinct interference fringes). Since the light in the final 2×2 MMI is split 50:50 amongst the tap port and the final 2×1 combiner, the total optical power that would exit the 2×1 combiner is equivalent to the sum of the two tap-ports (neglecting the loss of the 2×1 MMI).

Summing the two tap-ports and normalizing by the reference waveguide losses, the measured insertion loss across the spectrum was 9.1 ± 1.7 dB. The same chip contained 1- and 2-stage dFT spectrometers (Supplementary Figure A-3a and A-3b), and the same procedure as above was used to determine their insertion losses. The corresponding loss of the 2-stage dFT spectrometer was 6.8 ± 1.2 dB and the 1-stage dFT spectrometer was 5.5 ± 0.8 dB. The loss per stage was determined via linear regression to be 1.7 dB/stage, with a standard deviation error on this parameter of 0.4 dB (extracted from the parameter covariance matrix).

We note that the final 2×2 MMI’s on the top and bottom arms incur a 3 dB loss penalty on the total insertion loss of the spectrometer. In future designs, it is possible to place an additional optical switch on both top and bottom arms to guide 100% of the light to the beam-combiner (this switch-state would depend on whether the input of the 2×2 MMI comes from the top or bottom port) to solve this issue.

A.3 Modulation efficiency estimates for thermo-optic and electro-optic phase shifters

For thermo-optic modulators, we assume a constant temperature rise of 60°C in the Si waveguide (with $dn/dT = 1.8 \times 10^{-4}$ K⁻¹) induced by local heating elements and an operating wavelength of 1550 nm. From these figures, a modulation efficiency

(induced phase per unit waveguide length) is 433 rad/cm.

For electro-optic modulators [51], we assume a typical $V_\pi L_\pi = 1$ V·cm and applied voltage of 100 V. From this, the resulting modulation efficiency is 314 rad/cm.

To estimate the modulation efficiency of direct waveguide path modulation, we have a group index of $n_g = 4.25$ for the SOI waveguide geometry we employed, which yields a modulation efficiency of 172281 rad/cm, a factor of 398 and 548 times greater than that of the thermo-optic and electro-optic shifters, respectively.

A.4 Temperature dependence of the dFT spectrometer

By detuning the thermoelectric heating/cooling element below the dFT chip, we performed a set of measurements and spectral reconstructions of a single-frequency laser at 1560.0 nm. Using matrices A_1 and A_2 both measured at $T = 25.00^\circ\text{C}$ and the temperature detuned interferogram measurements y_1 and y_2 (temperatures ranging from 25.00°C to 23.87°C), we used the elastic- D_1 method to reconstruct the spectrum.

For sparse (narrowband) inputs, the temperature detuning produced only a shift in the center wavelength of the single frequency laser, and otherwise did not produce significant spectral noise. Using this data, we characterized the first-order temperature sensitivity to be $-85.2 \pm 1.3^\circ\text{C}$, as shown in Figure A-4.

A.5 Performance benchmarking

In the following, we compare the performance of the dFT spectrometer with several other experimental demonstrations of on-chip photonic spectrometers. The results are presented in Table A.1 and the analysis methods are outlined below.

5-stage dFT: The insertion loss value was estimated from the measured loss per switching stage (2.75 dB per stage) and the insertion loss of the 64-channel device (10.0 dB).

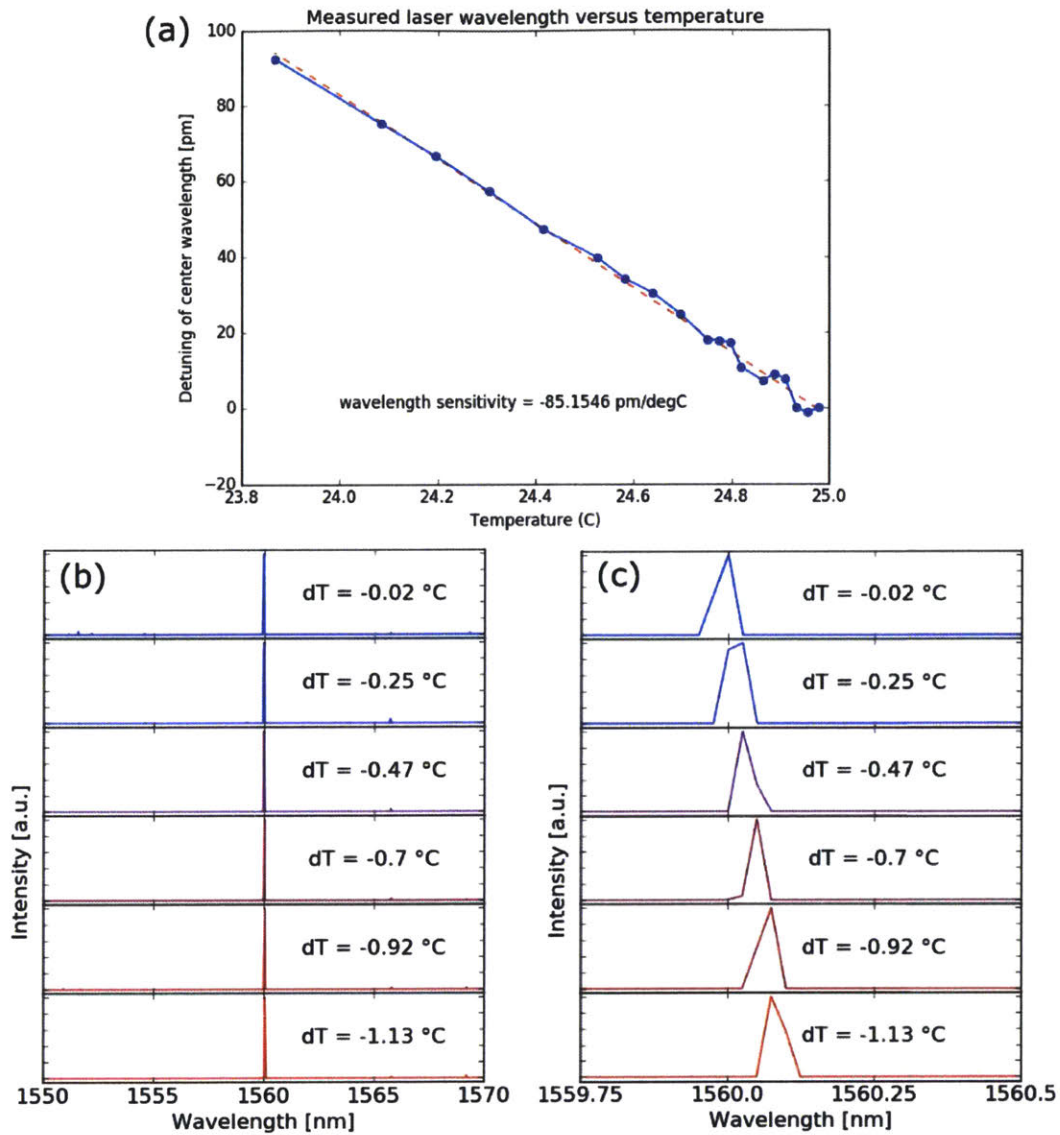


Figure A-4: Temperature dependence of narrowband dFT reconstructions. (a) Measured detuning of the center wavelength (given an input laser at constant wavelength of $\lambda = 1560.0$ nm) for different temperatures as measured by a thermistor near the photonic chip. Images at bottom show the reconstructed laser line for a number of different temperatures across the full 20 nm band (b) and a zoomed in image is provided to show the change in center wavelength (c).

32-channel MZI array (Velasco, *et al.* [182]): Insertion loss was estimated from the reported 4 dB/cm propagation loss, average waveguide length of 0.565 cm, and equal power splitting amongst 32 channels. This is a lower bound, as additional losses

from power-splitting elements (1×2 MMI's) and waveguides leading up to the spirals are not included.

32-channel MZI array (Herrero-Bermello, *et al.* [78]) Insertion loss was estimated from the reported 4 dB/cm propagation loss, average waveguide length of 1.89 cm, and equal power splitting amongst 32 channels. This is a lower bound, as additional losses from power-splitting elements (1×2 MMI's) and waveguides leading up to the spirals are not included.

42-channel MZI array (Nedeljkovic, *et al.* [130]): Insertion loss was estimated from the reported 8.8 dB/cm propagation loss, approximate waveguide length of 1.9 cm (estimated from reported 0.95 cm^2 device footprint), and equal power splitting amongst 42 channels. This is a lower bound, as additional losses from power-splitting elements (1×2 MMI's) and bending losses are not included.

Thermo-optic FTIR (Souza, *et al.* [172]): Insertion loss estimated from the reported 2 dB/cm propagation loss, 30.407 mm arm length of the thermally tuned interferometer, and 0.3 dB loss per y-junction (2 total).

50-channel AWG (Cheben, *et al.* [34]): Insertion loss calculated from the reported 17 dB insertion loss and the power splitting amongst 50 channels.

6-channel AWG (Ryckeboer, *et al.* [160]): Insertion loss calculated from the reported 4 dB insertion loss and the power splitting amongst 6 channels.

6-channel AWG (Muneeb, *et al.* [127]): Insertion loss calculated from the reported average 2.0 dB insertion loss and power splitting amongst 6 channels.

8-channel AWG (Bogaerts, *et al.* [26]): Insertion loss calculated from averaging the minimum (center channel) insertion loss (1.1 dB) and maximum (outer channel) insertion loss (2.4 dB) and power splitting amongst 8 channels.

16-channel planar concave grating (Ryckeboer, *et al.* [160]): Insertion loss calculated from the average reported 6 dB insertion loss and the power splitting amongst 16 channels.

Random spectrometer (Redding, *et al.* [155]): Since no values for the insertion loss were reported, we simply display the loss due to power splitting (14 dB) and note that the true insertion loss is larger than this value.

Spectrometer type	Spectral channel count	Spectral resolution	Bandwidth	Insertion loss per channel*	Power consumption	On-chip detector integration
3-stage dFT (this work)	64	24.6 GHz	2.47 THz	10.0 dB	99 mW	yes
5-stage dFT (projected)	1024	1.5 GHz	2.47 THz	15.5 dB	165 mW	yes
32-channel MZI array with fixed OPL [182]	32	5.0 GHz	0.094 THz	>17.3 dB	N/A	no
32-channel MZI array with fixed OPL [78]	32	2.3 GHz	0.035 THz	>22.6 dB	N/A	no
MZI array with fixed OPL [130]	42	57.9 GHz	0.54 THz	>32.9 dB	N/A	no
Thermo-optic FTIR [172]	18	380 GHz	7 THz	6.7 dB	2.5 W	no
Arrayed waveguide grating [34]	50	25 GHz	1.26 THz	34 dB	N/A	no
Arrayed waveguide grating [160]	6	99.1 GHz	0.801 THz	11.8 dB	N/A	yes
Arrayed waveguide grating [127]	6	202 GHz	1.2 THz	9.8 dB	N/A	yes
Arrayed waveguide grating [26]	8	400 GHz	3.2 THz	10.8 dB	N/A	no
Planar concave grating [160]	16	397.5 GHz	9.3 THz	18.0 dB	N/A	yes
Random spectrometer [155]	25	100 GHz	3.28 THz	>14 dB	N/A	no

Table A.1: Comparison of on-chip spectrometers. Side-by-side comparison of the demonstrated 64-channel dFT spectrometer along with previously reported MZI array FTIR, thermo-optic FTIR, arrayed waveguide grating, and random spectrometers. *Values in the “Insertion loss per channel” column account for the power loss per channel in dispersive spectrometers [34, 155, 160] when measuring broadband inputs and the loss from power-splitting in MZI array Fourier transform spectrometers [78, 130, 147, 182]. †For Fourier transform spectrometers with continuously tunable arms, we define the effective spectral channel count as the bandwidth divided by the minimum spectral resolution.

Appendix B

Roughness calculations

The following Appendix section provides additional information to Chapter 3. First, we derive the relevant figures of merit (FOM) for absorption spectroscopy, refractometry, and waveguide-enhanced Raman spectroscopy. Second, we outline methods for computing the polarizability of random Gaussian-correlated roughness. Lastly, the exact volume-current methods for computing the relative scattering loss of strip, slot, and sub-wavelength grating (SWG) waveguides in the main text are presented in detail.

B.1 Figure of merit for absorption spectroscopy and refractometry

In the following, we explicitly compute the appropriate performance metrics for three different modes of sensing to illustrate their proportionality to the absorption spectroscopy and refractometry figure of merit, $\text{FOM} = \Gamma_{\text{clad}}/(\alpha_s \lambda)$.

B.1.1 Absorption sensing

On-chip absorption spectroscopic sensors measure the change in optical power when chemicals of interest in the waveguide cladding absorb light from the evanescent field. In this scheme, light of input power $P(z = 0)$ (z is the distance along the direction of

propagation) at a known wavelength λ is attenuated due to molecular absorption in the cladding region and scattering losses from waveguide imperfections. The rate of change in optical power P in the presence of scattering losses (or other non-sensing losses, such as large Ohmic loss for plasmonic waveguides) α_s and absorption α_{abs} is:

$$\frac{dP}{dz} = -\Gamma_{\text{clad}}\alpha_{\text{abs}}P - \alpha_s P \quad (\text{B.1})$$

where Γ_{clad} is the external confinement factor that accounts for both slow-light effects and the fraction of electromagnetic energy residing in the waveguide cladding [70, 90, 99, 138, 157, 165, 177, 189]

$$\Gamma_{\text{clad}} = \frac{n_{\text{clad}}c\epsilon_0 \int_{\text{clad}} |\vec{E}|^2 dx^2}{\int_{\infty} \text{Re}\{\vec{E} \times \vec{H}^*\} \hat{z} dx^2} = \frac{n_g \int_{\text{clad}} \epsilon |\vec{E}|^2 dx^2}{n_{\text{clad}} \int_{\infty} \epsilon |\vec{E}|^2 dx^2} \quad (\text{B.2})$$

with n_{clad} the cladding index, n_g the group velocity, c the speed of light, ϵ_0 the vacuum permittivity, ϵ the material permittivity, and E and H the electric and magnetic fields of the waveguide modes. The absorption coefficient $\alpha_{\text{abs}} = \alpha_0 \cdot m$ is a wavelength-dependent attenuation coefficient that describes free-space optical absorption and depends on both the number density of molecules in the cladding, m , and the molecular absorption coefficient α_0 (related to the transition dipole moment). The absorption coefficient tends to have strong peaks in the infrared due to vibrational and rotational transitions, so measuring power changes at wavelengths of high absorption is a sensitive and selective method for identifying specific gases or liquids [113].

The relevant quantity of interest is the change in optical power $P(L) - P(0)$ along a waveguide of length L normalized by the input power $P(0)$ when a small amount of chemical/analyte is introduced to the sensing region. The figure of merit (FOM) we care about is the corresponding sensitivity $S_{\text{abs}} = dp/dm$, where $p = (P(0) - P(L))/P(0)$ is the fractional optical power change.

$$S_{\text{abs}} = \frac{d}{dm}(1 - e^{-\Gamma_{\text{clad}}\alpha_{\text{abs}}z - \alpha_s z}) = \Gamma_{\text{clad}}\alpha_0 z e^{-\Gamma_{\text{clad}}\alpha_{\text{abs}}z - \alpha_s z} \quad (\text{B.3})$$

The sensitivity can then be maximized with respect to the waveguide length z :

$$\frac{dS_{\text{abs}}}{dz} = 0 = 1 - z_{\text{max}}(\Gamma_{\text{clad}}\alpha_{\text{abs}} + \alpha_s) \quad (\text{B.4})$$

$$z_{\text{max}} = \frac{1}{\Gamma_{\text{clad}}\alpha_{\text{abs}} + \alpha_s} \quad (\text{B.5})$$

The optimized sensitivity is then:

$$S_{\text{max,abs}} = \frac{\Gamma_{\text{clad}}\alpha_0}{\Gamma_{\text{clad}}\alpha_{\text{abs}} + \alpha_s} \cdot e^{-1} \quad (\text{B.6})$$

In most cases the fabrication-induced scattering losses is significantly larger than absorption (especially for sensing of trace molecules). Thus, maximizing the external confinement factor and minimizing scattering losses is a suitable FOM since it maximizes the relative optical power change due to nearby absorbing chemicals.

$$S_{\text{max,abs}} = \frac{\Gamma_{\text{clad}}\alpha_0}{\alpha_s} e^{-1} \quad (\text{B.7})$$

B.1.2 Mach–Zehnder refractometry

For a typical Mach–Zehnder refractometer-based sensor, which consists of a 1×2 beam splitter, two waveguides with path lengths z_1 and z_2 , and a 2×2 (or 2×1) combiner, one measures a change in optical power at the output the interferometer to infer a change in the cladding refractive index Δn_{clad} . As light propagates along one of the arms, it acquires an additional phase $\Delta\phi_1 = 2\pi\Gamma_{\text{clad}}\Delta n_{\text{clad}}z_1/\lambda + 2\pi n_g\Delta z/\lambda$ (where $\Delta z = z_2 - z_1$) due to the presence of chemicals in the cladding and the path length difference. If we take $\Delta z = \lambda/(4n_g)$ (for convenience, and with no loss of generality) and $z_1 \sim z_2$ (which follows if $z \gg \Delta z$), the corresponding optical power at each of the two output ports is [161]:

$$P_1 = P(0) \cos^2(\pi\Gamma_{\text{clad}}\Delta n_{\text{clad}}z/\lambda + \pi/4)e^{-\alpha_s d} \quad (\text{B.8})$$

$$P_2 = P(0) \sin^2(\pi\Gamma_{\text{clad}}\Delta n_{\text{clad}}z/\lambda + \pi/4)e^{-\alpha_s d} \quad (\text{B.9})$$

The sensitivity of our refractometer is the fractional power change ($p = (P_1 - P(0))/P(0)$) at one of the two ports for a small increase in analyte that produces an index shift Δn_{clad} in the cladding:

$$S_{\text{MZI}} = \frac{dp}{d(\Delta n_{\text{clad}})} = \frac{z\Gamma_{\text{clad}}\pi}{\lambda} \cos\left(\frac{2\pi\Gamma_{\text{clad}}\Delta n_{\text{clad}}z}{\lambda}\right) e^{-\alpha_s z} \quad (\text{B.10})$$

The above metric is often called the figure of merit for Mach-Zehnder refractometers (the $e^{-\alpha_s z}$ term is often omitted, assuming no optical loss) [19, 57, 77, 115]. For small index shifts, the cosine term tends towards 1 and the optimal arm length z (that solves $dS/dz = 0$) is $z_{\text{max}} = 1/\alpha_s$:

$$S_{\text{max,MZI}} = \frac{\Gamma_{\text{clad}}\pi}{\lambda\alpha_s} e^{-1} \quad (\text{B.11})$$

B.1.3 Ring-resonator refractometry

Likewise, ring-resonator-based refractometry sensors measure changes in the through-port power of a CW laser when molecules in the cladding change the index surrounding the ring waveguide core. In this scheme, we assume a laser line is tuned to the steepest slope of the ring's resonance. Corresponding changes in the index of the surroundings will shift the resonance and produce a corresponding change in output optical power. The lineshape of a ring resonator nearby the resonance (assuming low cavity loss such that $\alpha d \ll 1$, with d the ring roundtrip length) is given by [161]:

$$\frac{P_{\text{output}}}{P(0)} = 1 - \frac{1}{1 + \left(\frac{2\pi(\nu - \nu_0)n_{\text{eff}}}{\alpha c_0}\right)^2} \quad (\text{B.12})$$

where $\nu_0 = q\frac{c_0}{n_{\text{eff}}d}$ is the frequency of the q -th resonator mode, c_0 is the speed of light, and α is the resonator waveguide's loss per unit length. In particular, the maximum slope occurs when the laser is tuned to $\nu = \nu_0 \pm \frac{\alpha c_0}{4\sqrt{3}n_{\text{eff}}\pi}$. We can now define a sensitivity metric (similar to before) as being the fractional change in optical power $p = P_{\text{output}}/P(0)$ for a small change in the cladding index. To first order, the entire resonance shifts by a frequency amount $\Delta\nu = -q\frac{c_0}{n_{\text{eff}}^2 d}\Gamma_{\text{clad}}\Delta n_{\text{clad}}$, so that the

maximum sensitivity is:

$$S_{\max,\text{ring}} = \frac{dp}{d(\Delta n_{\text{clad}})} = \frac{dp}{d\nu} \frac{d\nu}{d(\Delta n_{\text{clad}})} = \frac{3\sqrt{3}\pi q}{4n_{\text{eff}}d} \frac{\Gamma_{\text{clad}}}{\alpha_s} \quad (\text{B.13})$$

where in the above we assume that the loss is predominantly due to scattering ($\alpha \approx \alpha_s$).

Here we showed that the sensitivity metric depends on the factor $\Gamma_{\text{clad}}/\alpha_s$ for optical intensity interrogation. Furthermore, the sensitivity for other ring resonator sensing schemes such as wavelength interrogation are also proportional to $\Gamma_{\text{clad}}/\alpha_s$ [81]. In general, one can show that the sensitivity metric for almost all evanescent waveguide absorption sensors and refractometers includes the $\Gamma_{\text{clad}}/\alpha_s$ proportionality factor. Other constants in the sensitivity metric account for the correct dimensionality and are in general not a function of the waveguide geometry. Therefore, we choose the following dimensionless FOM as a suitable metric for comparing different waveguide geometries used in common refractometers and absorption sensors.

$$\text{FOM}_\Gamma = \frac{\Gamma_{\text{clad}}}{\alpha_s \lambda} \quad (\text{B.14})$$

B.2 Spontaneous Raman spectroscopy figure of merit

In waveguide integrated sensors that operate via spontaneous Raman spectroscopy, light at an initial wavelength λ_p interacts with nearby molecules in the cladding and scatters light at a new wavelength λ_n . The collection of this light serves as the signal of interest, and so the relevant figure of merit is the ratio of Raman scattered optical power collected by the waveguide P_n to initial power P_p in the waveguide, P_n/P_p . Our semiclassical analysis (similar to derivations that use Fermi's golden rule [47, 91]) accounts for the molecule's interaction with the electric field mediated by the full Raman polarizability matrix $\hat{\alpha}_{\text{ram}}$, and can be readily extended to the study of anisotropic scatterers and scattering mechanisms such as coherent Raman spectroscopy. For a single molecular scatterer, the incident light excites a current source equal to the derivative of the change in dipole moment, $\vec{J}(\vec{x}) = -i\omega_n \Delta p(\vec{x}, \omega_n) \delta(\vec{x} - \vec{x}_0) =$

$-i\omega_n \hat{\alpha}_{\text{ram}} \cdot \vec{E}_p(\vec{x}, \omega_p) \delta(\vec{x} - \vec{x}_0)$, where ω_n is the new Raman scattered frequency, E_p is the electric field of the incident waveguide mode (denoted by p) with frequency ω_p , Δp is the induced dipole moment, \vec{x}_0 is the location of the single molecule scatterer, and $\hat{\alpha}_{\text{ram}}$ is the spontaneous Raman polarizability of the molecule, a rank-2 tensor. The total power radiated by a current source into each of the i electromagnetic modes of the system (not waveguide modes) is given by [136]:

$$P = \frac{\pi}{4} \sum_i \frac{\left| \int \vec{E}_i^*(\vec{x}) \cdot \vec{J}(\vec{x}) dx^3 \right|^2}{\int_{\infty} \epsilon(\vec{x}) |\vec{E}_i(\vec{x})|^2 dx^3} \delta(\omega - \omega_i) \quad (\text{B.15})$$

where the denominator serves to normalize the energy of the electric field. For a constant cross-section waveguide (translationally invariant along the propagation direction \hat{z}), the total power coupled into the waveguide modes (indexed by n') is:

$$P_{\text{wg}} = \frac{\pi}{4} \sum_{n'} \int dk_z \frac{\left| \int_{\text{cs}} \vec{E}_{n'}^*(\vec{x}, k) \cdot \vec{J}(\vec{x}) \right|^2}{\int_{\text{cs}} \epsilon(\vec{x}) |\vec{E}_{n'}(\vec{x}, k)|^2} \delta(\omega - \omega_{n'}(k_z)) \quad (\text{B.16})$$

where the “cs” subscript denotes integration over the entire two-dimensional cross-section, \vec{x} vectors refer to the 2-dimensional position vector, and k_z is the wave vector in the \hat{z} direction (the integrand is sometimes referred to as the “mutual density of states”, or MDOS [121]). We now wish to compute the power radiated into a single waveguide mode (denoted by n), and so the above is simplified to:

$$P_n = \frac{\pi}{4} \frac{\left| \int_{\text{cs}} \vec{E}_n^*(\vec{x}, \omega_n) \cdot \vec{J}(\vec{x}) \right|^2}{\int_{\text{cs}} \epsilon(\vec{x}) |\vec{E}_n(\vec{x}, \omega_n)|^2} \rho_{1D}(\omega_n) \quad (\text{B.17})$$

In the above, $\rho_{1D} = 1/(\pi v_g)$ is the 1-dimensional density of states for the waveguide arising from the delta function with a Jacobian factor [11]. Direct substitution of the driven current source expression for a single-molecule scatterer yields:

$$P_n = \frac{\omega_n^2}{4v_g(\omega_n)} \frac{\left| \vec{E}_n^*(\vec{x}_0, \omega_n) \cdot \hat{\alpha}_{\text{ram}} \cdot \vec{E}_p(\vec{x}_0, \omega_p) \right|^2}{\int_{\text{cs}} \epsilon(\vec{x}) |\vec{E}_n(\vec{x}, \omega_n)|^2} \quad (\text{B.18})$$

We typically only care about the amount of power scattered into the waveguide for a given number density of scatterers m (number per unit volume) in the cladding region over an infinitesimal distance dz along the propagation direction. Therefore we take an average of the collected power over all inequivalent positions in the cladding (denoted by the subscript “clad”):

$$\langle P_n \rangle = \left(\frac{\omega_n^2 \cdot m \cdot dz}{4v_g(\omega_n)} \right) \frac{\int_{\text{clad}} \left| \vec{E}_n^*(\vec{x}, \omega_n) \cdot \hat{\alpha}_{\text{ram}} \cdot \vec{E}_p(\vec{x}, \omega_p) \right|^2}{\int_{\text{cs}} \epsilon(\vec{x}) |\vec{E}_n(\vec{x}, \omega_n)|^2} \quad (\text{B.19})$$

For simplicity, we assume the polarizability $\hat{\alpha}_{\text{ram}}$ is independent of position, but in general this could change if the density varies. Finally, we normalize the average Raman-scattered power to the input laser power P_p :

$$\frac{\langle P_n \rangle}{P_p} = \left(\frac{\omega_n^2 \cdot m \cdot dz}{4v_g(\omega_n)v_g(\omega_p)} \right) \times \quad (\text{B.20})$$

$$\frac{\int_{\text{clad}} \left| \vec{E}_n^*(\vec{x}, \omega_n) \cdot \hat{\alpha}_{\text{ram}} \cdot \vec{E}_p(\vec{x}, \omega_p) \right|^2}{\left(\int_{\text{cs}} \epsilon(\vec{x}) |\vec{E}_p(\vec{x}, \omega_p)|^2 \right) \left(\int_{\text{cs}} \epsilon(\vec{x}) |\vec{E}_n(\vec{x}, \omega_n)|^2 \right)} \quad (\text{B.21})$$

If we assume the molecules are isotropic and uniformly distributed, then the polarizability matrix is simply a scalar and we can factor it from the integral in the numerator. When comparing waveguide geometries for the purpose of maximizing the signal of interest for waveguide Raman spectroscopy, the relevant design parameters are the two factors of group velocity v_g that account for slow light effects, the electric field strength of the incident waveguide mode at ω_p , and the electric field strength of the new waveguide mode at ω_n . Thus, the relevant quantity of interest is the Raman gain coefficient β in units of inverse distance:

$$\beta = \frac{\langle P_n \rangle}{P_p} \frac{1}{dz} = \quad (\text{B.22})$$

$$\left(\frac{\alpha_{\text{ram}}^2 \cdot \omega_n^2 \cdot m}{4v_g(\omega_n)v_g(\omega_p)} \right) \frac{\int_{\text{clad}} \left| \vec{E}_n^*(\vec{x}, \omega_n) \vec{E}_p(\vec{x}, \omega_p) \right|^2}{\left(\int_{\text{cs}} \epsilon(\vec{x}) |\vec{E}_p(\vec{x}, \omega_p)|^2 \right) \left(\int_{\text{cs}} \epsilon(\vec{x}) |\vec{E}_n(\vec{x}, \omega_n)|^2 \right)} \quad (\text{B.23})$$

For waveguides with period Λ , Eq. B.16 can be equivalently rewritten in terms of 3-dimensional integrals over the entire unit cell:

$$P_{\text{wg}} = \frac{\pi}{4} \sum_{n'} \frac{\Lambda}{2\pi} \int_{-\frac{\pi}{\Lambda}}^{\frac{\pi}{\Lambda}} dk_z \frac{\left| \int_{\text{unit cell}} \vec{E}_{n'}^*(\vec{x}, k) \cdot \vec{J}(\vec{x}) \right|^2}{\int_{\text{unit cell}} \epsilon(\vec{x}) |\vec{E}_{n'}(\vec{x}, k)|^2} \delta(\omega - \omega_{n'}(k_z)) \quad (\text{B.24})$$

and we note that the delta function in $\vec{J}(\vec{x})$ above is 3-dimensional in contrast to the 2-dimensional delta function used in Eq. B.16 (thus preserving units). If we proceed in the same manner as before, we arrive at the Raman gain coefficient for periodic structures:

$$\beta_{\text{SWG}} = \left(\frac{\alpha_{\text{ram}}^2 \cdot \omega_n^2 \cdot m}{4v_g(\omega_n)v_g(\omega_p)} \right) \left(\frac{\Lambda}{2\pi} \right) \times \quad (\text{B.25})$$

$$\frac{\int_{\text{clad}} \left| \vec{E}_n^*(\vec{x}, \omega_n) \vec{E}_p(\vec{x}, \omega_p) \right|^2}{\left(\int_{\text{unit cell}} \epsilon(\vec{x}) |\vec{E}_p(\vec{x}, \omega_p)|^2 \right) \left(\int_{\text{unit cell}} \epsilon(\vec{x}) |\vec{E}_n(\vec{x}, \omega_n)|^2 \right)} \quad (\text{B.26})$$

Now, we may readily incorporate the effects of scattering loss due to waveguide imperfections. This is typically described by the scattering loss attenuation coefficient α with units of inverse length. The change in our signal P_n per unit length is similar to Eq. B.1, but with an additional loss term to account for the Raman gain coefficient and propagation losses at both signal- and Raman-scattered wavelengths:

$$\frac{dP_n}{dz} = -\alpha_n P_n + \beta P_p e^{-\alpha_p z} \quad (\text{B.27})$$

where α_p and α_n denote the scattering loss at the incident wavelength and new Raman scattered wavelength, respectively. Solving this differential equation yields:

$$\frac{P_n(z)}{P_p(0)} = \frac{\beta e^{-\alpha_n z}}{\alpha_n - \alpha_p} [e^{z(\alpha_n - \alpha_p)} - 1] \quad (\text{B.28})$$

Further simplification can be made by assuming the scattering losses at incident and

signal wavelengths are equal.

$$\lim_{\alpha_n \rightarrow \alpha_p} P_n(z) = \beta P_p z e^{-\alpha_{n,p} z} \quad (\text{B.29})$$

Our goal is then to maximize the signal power by optimizing z , the length of the waveguide. We can see from Eq. B.29 that too short of a waveguide has insufficient length for the light to interact with the analyte and generate a signal, while a waveguide that is too long loses a significant amount of incident and signal light from scattering losses.

$$\frac{dP_n(z)}{dz} = 0 = \beta P_p e^{-\alpha_{n,p} z_{\max}} - \alpha_{n,p} z_{\max} \beta P_p e^{-\alpha_{n,p} z_{\max}} \quad (\text{B.30})$$

$$z_{\max} = 1/\alpha_{n,p} \quad (\text{B.31})$$

If we consider a waveguide integrated Raman sensor with optimized waveguide length, the relevant figure of merit for sensing is then simply the signal power at $z = z_{\max}$ divided by the input power at $z = 0$.

$$\frac{P_n(z_{\max})}{P_p(0)} = \frac{\beta}{\alpha_{n,p}} \cdot e^{-1} \quad (\text{B.32})$$

In this work, we are interested in determining only the optimal waveguide geometries for spontaneous Raman sensing. Therefore, constants such as the Raman polarizability and the number density of scatterers are not relevant and are set to unity in our comparison. In most practical Raman spectrometers, $\omega_n \approx \omega_p$. This is in part due to increased Raman scattering efficiencies at higher optical frequencies such as $\bar{\nu} = 12,500 - 20,000 \text{ cm}^{-1}$ ($\lambda_p = 500 - 800 \text{ nm}$), since α_{ram} scales with ω^4 [63]. Meanwhile, typical Raman shifts of interest correspond to low-energy vibrational or rotational transitions in the region of $500 - 1,500 \text{ cm}^{-1}$. Therefore, our dimensionless figure of merit that involves only terms relevant for comparing different waveguide geometries

(i.e. constants and prefactors set equal to 1) is:

$$\text{FOM}_\beta = \frac{\beta}{\alpha_s} \propto \frac{1}{\alpha_s} \cdot \frac{n_g^2(\omega_p)}{n_{\text{clad}}^2} \frac{\int_{\text{clad}} |\vec{E}(x_0, \omega_p)|^4 dx_0}{(\int_{\text{cs}} \epsilon(x) |\vec{E}(x, \omega_p)|^2 dx)^2} \quad (\text{B.33})$$

and for periodic structures,

$$\text{FOM}_{\beta_{\text{SWG}}} = \frac{\beta_{\text{SWG}}}{\alpha_s} \propto \frac{\Lambda}{\alpha_s} \cdot \frac{n_g^2(\omega_p)}{n_{\text{clad}}^2} \frac{\int_{\text{clad}} |\vec{E}(x_0, \omega_p)|^4 dx_0}{(\int_{\text{unit cell}} \epsilon(x) |\vec{E}(x, \omega_p)|^2 dx)^2} \quad (\text{B.34})$$

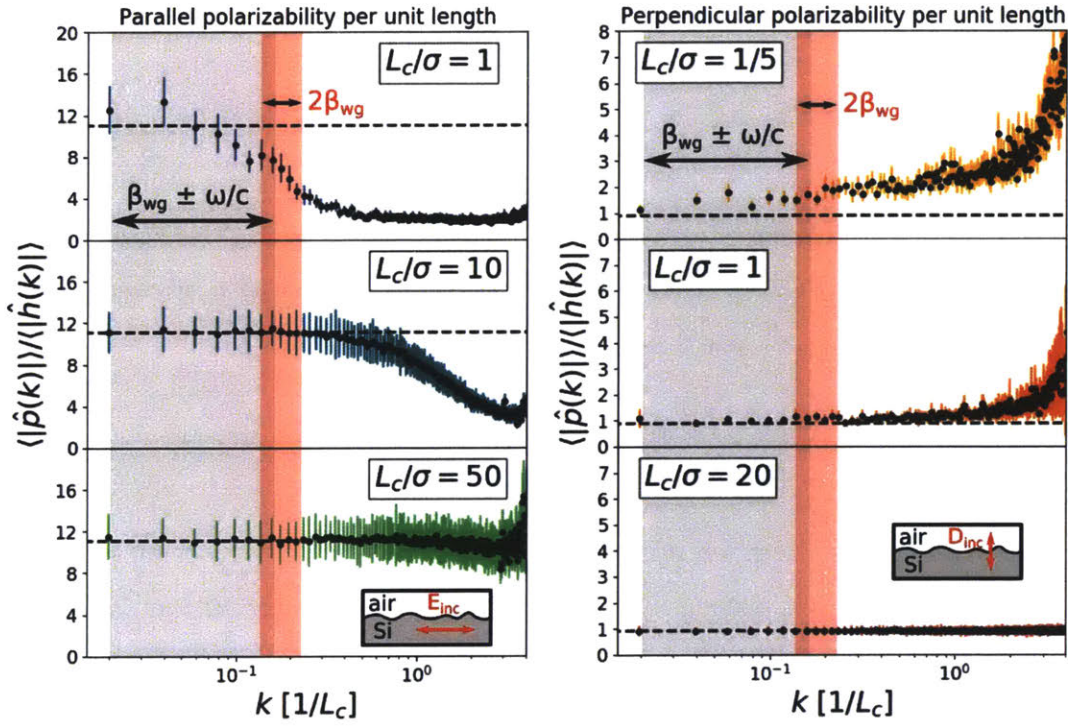


Figure B-1: Numerically computed Fourier components of the polarizability for a randomly generated surface with Gaussian correlation length and a unit-valued incident field parallel (left) and perpendicular (right) to the interface for different ratios of L_c/σ . Black dashed lines correspond to the analytical polarizabilities of $\alpha_{\parallel} = 11.1$ and $\gamma_{\perp} = 0.92$ for a flat shifted silicon/air interface. Gray shaded regions correspond to Fourier-components of the roughness that scatter light into the far-field and red shaded regions correspond to components that reflect light in the backwards direction (β_{wg} corresponds to the range of propagation coefficients for all waveguide-geometries considered in this text, and is scaled assuming a roughness correlation length of 75 nm and wavelength of $\lambda=1550$ nm). Colored errorbars denote the standard error of the mean for multiple computations.

B.3 Polarizability of rough surfaces

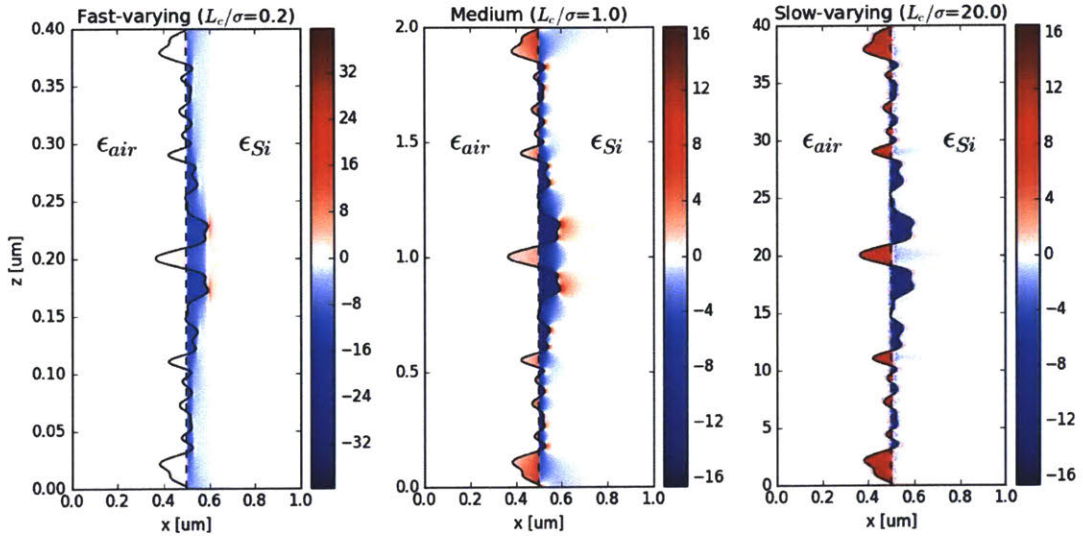


Figure B-2: Computed changes in the perturbed polarization density $\Delta P(\vec{r}) \cdot \hat{z}$ along a rough waveguide sidewall with short ($L_c/\sigma = 0.2$), medium ($L_c/\sigma = 1.0$), and long ($L_c/\sigma = 20$) correlation lengths with respect to the RMS roughness σ . Solid black line shows the perturbed sidewall, and dashed black line shows the straight, unperturbed sidewall.

In the volume-current method, it is critically important to understand the nature of the perturbed dipole moments from perturbations at a dielectric interface. For small, localized perturbations (such as bumps or point-defects), the electric polarizability α_{\parallel} and γ_{\perp} relates the magnitude of the current source \vec{J} to the incident field. However, for roughness that exists along the entire interface, our goal is to understand the statistical properties of the ensemble of dipole moments in the quasi-static limit. In the following, we computationally verify that the flat shifted-interface polarizability is an accurate approximation for Gaussian-correlated randomly rough sidewalls so long as the correlation length L_c is considerably larger than the root-mean-square (RMS) amplitude of the perturbation height σ .

To determine the appropriate limits for which the flat-shifted interface is valid, we determined the Fourier components of the 1-dimensional electrostatic polarizability density (along the interface-direction) by numerically computing the induced dipole moment density (per unit length) for randomly generated surfaces. Zero-mean side-

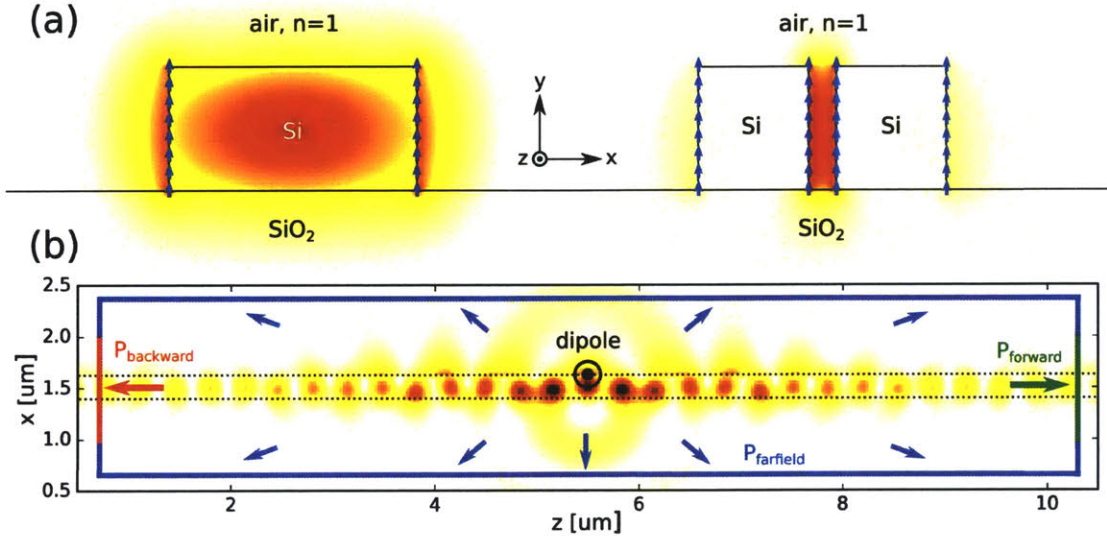


Figure B-3: (a) Cross-sectional image of the electric field magnitude $|\vec{E}|^2$ for a dipole radiating along the surface of a strip waveguide. The blue solid line indicates the position of power flux monitors measuring the amount of radiation into the far-field. The green and red solid lines denote locations of power flux monitors that measure the radiation that couples back into the forward and backwards propagating waveguide mode. Simulation resolution shown above and in all calculations is 32 pixels/ μm . (b) Cross-sectional image in the $\hat{x} - \hat{y}$ plane for both strip (left) and slot (right) structure waveguides with $|\vec{E}|^2$ shown in red. For each FDTD simulation, a line of current sources are placed at each inequivalent sidewall position (only one for each strip waveguide geometry and two for each slot waveguide geometry), with the appropriate complex amplitude retrieved from the waveguide mode's electric field strength at each point.

wall functions $h(z)$ with a Gaussian autocorrelation function $R(z') = \sigma^2 \exp(-z'^2/L_c^2)$ were generated to represent the roughness profile, where σ is the root mean square (RMS) roughness amplitude and L_c denotes the roughness correlation length [134]. This was done by filtering Gaussian white noise with the appropriate filter functions specified by the desired roughness autocorrelation function [23, 92, 117, 199]. We then solved the corresponding electrostatic Poisson equation using FEniCS, an open-source partial differential equation solver [9], to obtain the resulting charge distribution for silicon/air interfaces with a sidewall profile $h(z)$, as shown in Figure B-2. For perpendicular incident fields with constant field D_{\perp} , we use periodic boundary conditions at the edges of the interface and Neumann boundary conditions for simulation bound-

aries parallel to the interface. For parallel incident fields with constant field E_{\parallel} , we specify the corresponding electrostatic potential via appropriate Dirichlet boundary conditions along the simulation boundaries. Each simulation window used was $320 \cdot L_c$ long and $40 \cdot \sigma$ wide, with an adaptive finite-element mesh. The dipole moment density corresponding to each specific roughness profile $h(z)$ was then computed from the spatial charge distribution through [86]:

$$p_{1D,\perp}(z) = \frac{1}{\Delta z} \int_{-\infty}^{\infty} \int_{z-\Delta z/2}^{z+\Delta z/2} (x - x_0) \cdot \Delta \rho(\vec{x}) d\vec{x} \quad (\text{B.35})$$

$$p_{1D,\parallel}(z) = \frac{1}{\Delta z} \int_{-\infty}^{\infty} \int_{z-\Delta z/2}^{z+\Delta z/2} (\Delta \vec{P}(\vec{x}) \cdot \hat{z}) d\vec{x} \quad (\text{B.36})$$

where Δz is the pixel size along the interface, $\Delta \vec{P}$ is the change in electrostatic polarization density ($\vec{P} = \epsilon_0(\epsilon - 1)\vec{E}$) and \hat{x} is normal to the interface (perpendicular to \hat{z}). In principle, we can use the same expression for both perpendicular and parallel components, but we found the above expressions converged faster at a given finite resolution. The dipole moment density per unit perturbation height $h(z)$ is then related to the polarizability through $p_{\parallel}/h = \alpha_{\parallel} E_{\parallel}$ (and likewise $p_{\perp}/h = \gamma_{\perp} D_{\perp}$). Using this technique, we also performed a set of validation tests on flat-shifted boundaries and cylindrical/square perturbations to ensure that our method (and mesh resolution) accurately reproduces the correct electrostatic polarizabilities.

Using this technique to compute the induced dipole moment densities, we investigated the effect of different surface roughness statistics, quantified by the dimensionless ratio L_c/σ . Figure B-1 shows the ratio of the averaged Fourier components (in spatial-frequency space) of the dipole moment density $\hat{p}(k)$ to the Fourier components of the surface profile $\hat{h}(k)$. For a locally flat interface, the induced dipole moments are proportional to the perturbed height, and so far from L_c we expect $\hat{p} \sim \hat{h}$. In the limit of long correlation lengths (large L_c/σ) our computations recover the expected polarizability of a flat-shifted interface, shown by dashed black lines in Figure B-1. In general, the surface roughness will act as a diffraction grating [101] that couples incident light of wavevector β to $k' = k_z + \beta$ with a strength proportional

to the roughness induced dipole moment $\hat{p}(k_z)$. However, light can only be scattered into the light cone or reflected back into the waveguide, which limits the relevant frequency components to being within $k' = \pm \frac{\omega}{c}$ (far-field radiation) and at $k' = 2\beta$ (reflection). The appropriate ranges for all waveguide geometries considered in the main text are depicted by the shaded regions in Figure B-1 (assuming a roughness correlation length of $L_c=75$ nm and $\lambda=1550$ nm).

As $L_c \rightarrow \infty$, it must be true that the locally flat result is recovered. In our analysis, we observe the useful result that for even relatively short correlation lengths on the order of $L_c = 10\sigma$, the Fourier components of the numerically computed polarizability match the simple shifted-boundary approximation by $\leq 1.2\%$ for the interface-parallel components and $\leq 0.5\%$ for the interface-perpendicular components. In state-of-the-art SOI waveguides, the correlation length of line-edge roughness was experimentally assessed to be between 50 to 100 nm, whereas the root mean square (RMS) roughness is typically between 0.5 to 2 nm [104, 185, 192, 195], corresponding to L_c/σ ratios on the order of 25–200. Therefore, we may accurately model the roughness-induced effective current-sources as flat-shifted interfaces for a large number of practical silicon photonic waveguide devices.

B.4 Volume-current method calculations

The relative scattering losses for each waveguide structure was determined by calculating the relative powers per unit volume of sidewall roughness (defined as the volume of the “bumps” on a surface) scattered into both the far-field P_{ff} and reflected backwards in the waveguide P_r . We restricted our focus to vertically symmetric (y -direction symmetric) line-edge roughness, and therefore modeled the roughness with 1-dimensional line current sources (in all 3-directions) with corresponding local amplitudes and phases proportional to the modal electric field, as depicted in Figure B-3(a). The electric and displacement field of each waveguide mode was computed using the MIT Photonic Bands software package [89], and special care was taken to ensure that the normalization of the 3-dimensional SWG modes are equivalent to the normal-

ization of the 2-dimensional strip and slot waveguide modes. We also make sure to normalize the input modal fields by *power*, rather than *energy*, to properly account for group velocity effects, and since our metric of interest is the scattered *power* per unit input power P_s/P_{in} . The current-source is determined by Equation 3.6:

$$\vec{J} = -i\omega\Delta h(\Delta\epsilon E_{\parallel} - \epsilon\Delta(\epsilon^{-1})D_{\perp})\delta(\vec{x}) \quad (\text{B.37})$$

For each waveguide geometry and each inequivalent sidewall position, the corresponding line of current sources is then simulated using MEEP, a freely available finite-difference time domain (FDTD) software package [137]. The amount of power scattered into the far-field, versus forward and backward scattered power are determined by monitoring the power flux (at a wavelength of 1550 nm) through the simulation boundaries, as shown in Figure B-3(b). Each FDTD simulation is computed with a resolution of 32 pixels/ μm and a domain size of $10\ \mu\text{m} \times 2.5\ \mu\text{m} \times 2.5\ \mu\text{m}$ with perfectly matched layers (PML) at the boundaries, except for SWGs where we place adiabatic absorbers at the z_{min} and z_{max} boundaries. The total power loss P_s (the sum of the far-field power P_{ff} and the reflected power P_r) is then averaged over all sidewall positions and computed per unit waveguide length.

Appendix C

Software and measurement systems

In the following sections, I will describe several notable infrastructure projects that I have started and made significant developments on over the last few years. These systems will hopefully aid future graduate students and researchers who wish to rapidly design lithography masks for integrated photonics, automate optical characterization measurements, and program test routines for complex photonic circuits (such as silicon nitride photonic circuits with many heaters).

C.1 PICwriter: A python module for generating GDSII masks for integrated photonics

PICwriter is a python library I developed for rapidly generating integrated photonics masks. This project aims to reduce the time from concept to mask generation, and the following features have been implemented:

- The library contains a set of commonly used parameterized cells ('PCells') for common components such as grating couplers, directional couplers, ring resonators, multi-mode interferometers. Each cell is a python class that can be instantiated and placed in the mask. Functions exist for drawing the corresponding shapes and connecting multiple components.
- Waveguides are implemented with a waypoint routing list, and support exists

for strip, slot, and subwavelength grating waveguides.

- All components can be easily linked to one another using port attributes (each port contains both a position and angle property).
- Generated masks contain information about the intended fabrication. For example, by specifying the photoresist tone (positive or negative) and etch type (liftoff or direct etch), PICwriter will generate the appropriate mask file.
- PICwriter is open-source and leverages gdspsy (github.com/heitzmann/gdspsy/), another open-source python library used for streaming out designs to the GDSII file format.

PICwriter is tested on Windows, Mac, and Linux and can be installed via python's pypi package manager.

```
pip install picwriter
```

For information on using or contributing to PICwriter, the documentation is online at picwriter.readthedocs.io/ and source code at github.com/DerekK88/PICwriter.

C.1.1 Example usage

As a quick example, the following code below demonstrates importing the necessary libraries, creating a gdspsy 'Cell' to add our components, making a template for the waveguides, and creating an 'S' shaped waveguide.

```
import gdspsy
from picwriter import toolkit as tk
import picwriter.components as pc

top = gdspsy.Cell("top")
wgt = pc.WaveguideTemplate(wg_width=0.45,
                           clad_width=10.0,
                           bend_radius=100,
                           resist='+',
                           fab='ETCH',
                           wg_layer=1,
                           wg_datatype=0,
```

```

                                clad_layer=2,
                                clad_datatype=0)

wg = pc.Waveguide([(25, 25), (975, 25),
                    (975,500), (25,500),
                    (25,975), (975,975)], wgt)

tk.add(top, wg)

tk.build_mask(top, wgt, final_layer=3, final_datatype=0)

gdspy.LayoutViewer()
gdspy.write_gds('tutorial.gds', unit=1.0e-6, precision=1.0e-9)

```

C.2 A semi-automated wafer-scale testbed for integrated photonics

During the development of the silicon nitride integrated photonics process flow on full 150 mm wafers outlined in Chapter 4, the volume of unique fabricated devices rapidly increased and it became increasingly important to automate optical measurements. For example, a grating coupler design was experimentally optimized by writing a grid with 13×13 unique grating couplers with varying pitch and duty-cycle. The traditional means of testing these components manually by aligning fibers to the individual devices is tedious and unreliable when done by a human operator.

To solve this, I built a custom test bed for automating the repetitive process of aligning fibers, then taking a measurement, and moving the stage to the next device. The platform was initially designed and assembled in a CAD environment (Solidworks) to make sure components were sized appropriately, the motorized stages had sufficient range, and there was sufficiently many degrees of freedom to perform the optical alignment. Designing the system in a CAD environment facilitated the process of rapidly designing custom steel components that could be quickly sent to external shops for CNC milling. A rendering of this setup as well as photographs of the real system during measurement are shown in Figures C-1 & C-2.

The complete system consists of a motorized XY translation sample stage (with manual rotation for the wafer) and two 6-axis fiber positioners (X-, Y-, and Z-

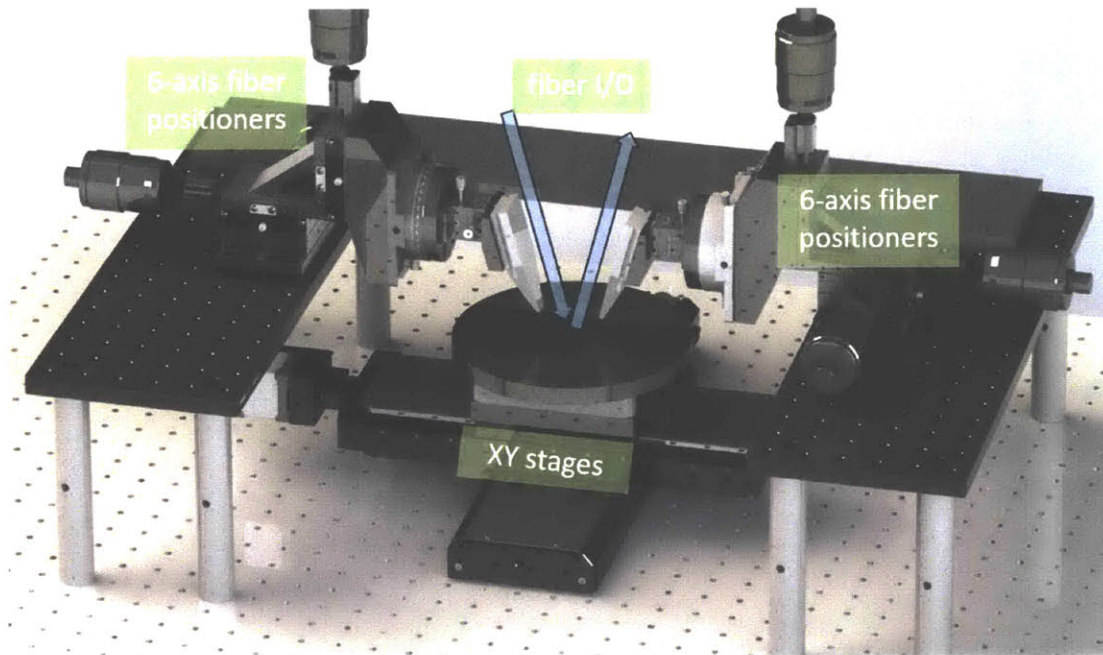


Figure C-1: CAD rendering of the wafer-scale automated wafer prober.

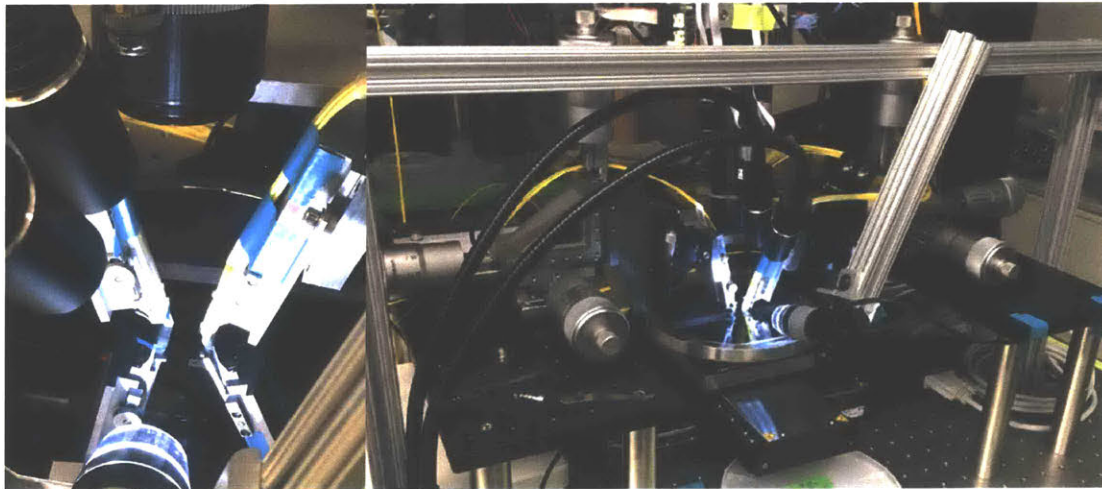


Figure C-2: Photograph images of the measurement system with a wafer loaded and one of the fiber arrays lowered above the wafer for measurement.

translation and pitch, yaw, and roll rotations) resting atop raised optical benches. Each 6-axis fiber positioner can be loaded with either a chuck for mounting single fibers, or another chuck for mounting entire fiber arrays. Once loaded, the fibers must be manually lowered above the wafer or chip and the angles must be optimized to achieve maximum optical coupling. Once aligned, the fibers remain fixed and the

motorized XY translation stage moves the chip/wafer below the fibers. Since the fiber positions are fixed and there will inevitably be some height difference from one edge of the wafer/chip to the opposite edge (i.e. the wafer will not sit perfectly flat), the fiber height needs to be re-optimized when moving to very distant wafer locations. Optical alignment to each device is performed using the XY stages, which have a minimum incremental motion of 100 nm and total travel of 150 mm. Software to control the motorized XY stages, the optical power meter, and the LUNA optical vector analyzer was written entirely in python. Alignment is performed using an initial coarse-resolution Archimedes spiral scan, followed by a fine-resolution Archimedes spiral scan in the vicinity of the point with maximum power coupling. Once alignment is achieved, either the photodetector is triggered to take a power measurement or the LUNA system is triggered to measure the frequency-dependent Jones matrix of the device. The code includes a graphical front-end that users interact with to manually move the stage, perform a single optical alignment, or automate measurements of grids of many devices with constant spacing without any programming. Since the chip or wafer XY coordinates are inevitably rotated slightly from the XY coordinates of the wafer-translation stages, a rotation correction step can be performed prior to running automated measurements of many devices on a grid. This correction procedure consists of first finding the stage positions for maximum coupling from two waveguide devices, then comparing these positions with the expected positions specified by the GDSII mask positions, and then applying an appropriate coordinate transformation in software.

Using this system, I was able to acquire enough experimental data to generate a database of performance optimized passive photonic components for the Si_3N_4 platform (grating couplers, directional couplers, 99:1 optical taps, power splitters, multi-mode interferometers, photonic crystal filters, and ring resonators).

CAD component files, assembly files, python code, and the bill of materials for this system can be freely accessed at github.com/DerekK88/PIC_WaferProbeSystem.

C.3 A photonics data acquisition module for silicon nitride PICs with thermal tuners

As described in Section 6.2, ultra-high channel count spectrometers with very high spectral resolution can be made from programmable photonic circuits with many tunable phase modulators. These devices require a measurement and control system that is capable of both independently biasing each phase modulator as well as monitoring the power from many optical channels. The optical power can be monitored via on-chip photodetectors (as was the case for the 64-channel spectrometer prototype with integrated germanium photodetectors) or sent off-chip for monitoring with an external fiber-coupled photodetector. Since the next set of optical chips with 1024 and 4096 spectrometer channels were designed and fabricated on a silicon nitride platform, the measurement system needed to record all optical signals externally. These chips contained as many as 30 thermal phase tuners (for configuring the optical switches) and 16 output channels each requiring a dedicated photodetector.

To accommodate testing the spectrometer chips as well as future chips with similar complexity and measurement requirements, I built a data acquisition module with the following targets in mind:

- Recording optical signals and outputting electrical signals should be *fast*. This means using a microcontroller to enable fast read/write from ADC's & DAC's.
- There should be up to 16 fiber coupled photodetectors that can all be read independently, with reasonably high bandwidth and high sensitivity (sub-10 pW optical power).
- The system must be capable of biasing up to 32 thermal phase tuners. Each channel must be independently controllable, and be capable of sourcing ~ 200 mW of power to achieve the appropriate $\pi/2$ phase shift for optical switching.
- The module must be *easy-to-use*, self-contained, and wrapped with a sufficiently

complete python library and API to enable rapid device testing with minimal high-level programming.

With this in mind, the system schematically illustrated in Figure C-3 was designed. With help from David Bono, custom printed circuit boards (PCBs) were designed, utilizing 16-bit DACs (Analog Devices AD5676), 16-bit precision ADCs (Analog Devices AD4001), and a Teensy 3.6 microcontroller that uses a 180 MHz ARM Cortex processor. Signals from each of the 16 photodetectors are read in using a separate PCB designed specifically to measure low-signal optical powers below 10 pW from a fiber coupled InGaAs photodetector (Thorlabs FGA01FC). These modular photodetector PCBs leverage a high-speed current-to-voltage logarithmic amplifier with 100 dB dynamic range (Analog Devices ADL5304) for sensing optical signals below 10 pW. Custom machined aluminum blocks allow these photodetector PCBs to be mounted to the front panel and shield the photodetector wires and PCB traces from electromagnetic noise.

The PCB designs and components were streamed out to CAD formats to facilitate designing a chassis for the entire system, as depicted in Figure C-4. After design of all components, the PCBs were manufactured and assembled externally, the custom aluminum components were milled by an external CNC service, and the front and back panel openings were cut on a water jet system.

The software that controls the photonics data acquisition module consists of C code loaded onto the Teensy microcontroller and a python module that the user interacts with. The microcontroller code is structured as a state-machine and alternates between accepting commands from the computer over USB, writing values to the DACs, reading in signals from the ADCs, and passing recorded data back to the computer over USB. The python module automatically establishes a serial connection with the microcontroller, passes instructions in a standardized format, reads in the data, and performs higher-level functions. Instructions (which consist of biasing specific phase tuners or reading values from specific photodetectors) are aggregated into large batches and sent to the microcontroller all at once. They are then executed sequentially and the data is sent back to the computer and received by the python

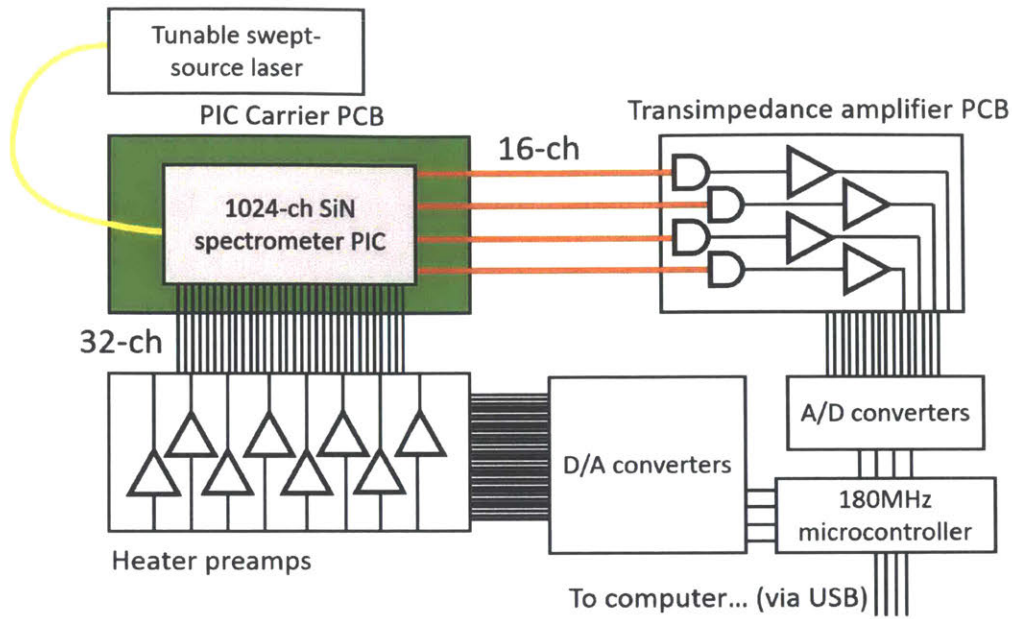


Figure C-3: Schematic overview of the photonics DAQ system.

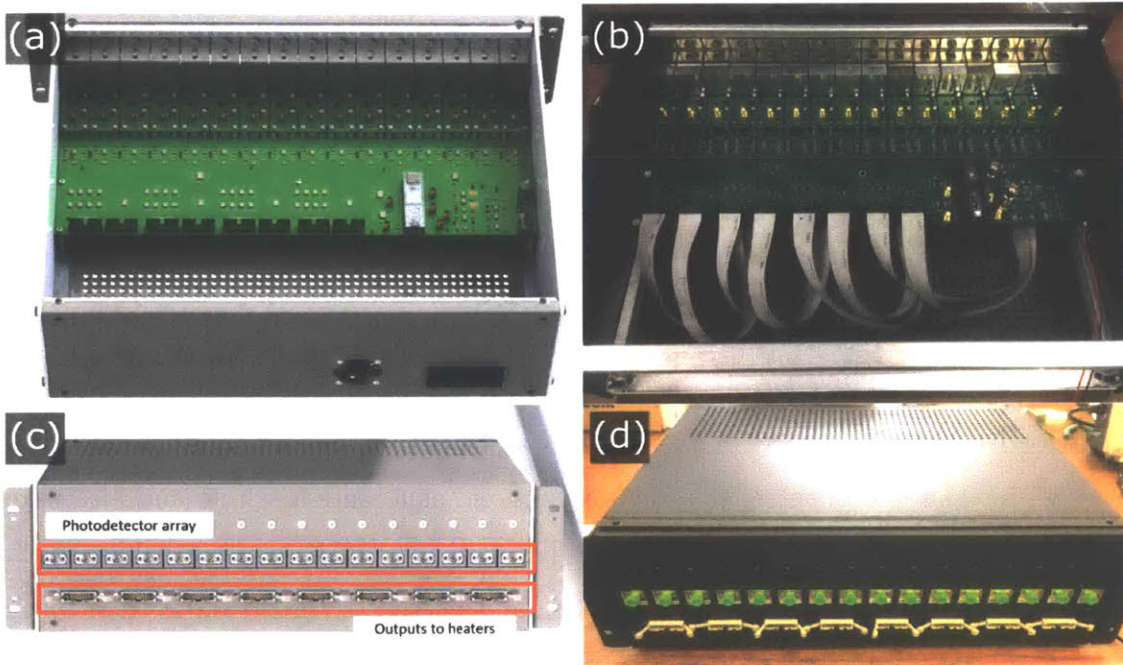


Figure C-4: Top-down CAD rendering (a) and photograph image (b) of the photonics DAQ assembly with PCB, mechanical enclosure, cables, and connectors. Front panel CAD rendering (c) and photograph image (d) of the module, showing the 16 FC/PC connectorized InGaAs detectors and electrical connectors for biasing up to 32 phase modulators.

library. High level program calls are used to generate and assemble these instructions into batches.

Bibliography

- [1] MLA150 fact sheet 2018. Technical report, Heidelberg Instruments Mikrotechnik GmbH, Heidelberg, 2018.
- [2] Ligentec Foundry, 2019.
- [3] LioniX International in Detail, 2019.
- [4] MTL Fabrication Machine Charge Chart, 2019.
- [5] PIX4life Schedule, 2019.
- [6] Yaser S. Abu-Mostafa. Learning From Data, 2012.
- [7] B. Imran Akca. Design of a compact and ultrahigh-resolution Fourier-transform spectrometer. *Optics Express*, 25(2):1487–1494, 2017.
- [8] T Alasaarela, D Korn, L Alloatti, A Tervonen, R Palmer, J Leuthold, W Freude, and S Honkanen. Reduced propagation loss in silicon strip and slot waveguides coated by atomic layer deposition. *Optics Express*, 19(12):11529–11538, 2011.
- [9] Martin S Alnaes, Jan Blechta, Johan Hake, August Johansson, Benjamin Kehlet, Anders Logg, Chris Richardson, Johannes Ring, Marie E Rognes, and Garth N Wells. The FEniCS project version 1.5. *Archive of Numerical Software*, 3(100):9–23, 2015.
- [10] M. Andersen, J. Dahl, and L. Vandenberghe. CVXOPT: Python software for convex optimization, 2016.
- [11] George B. Arfken and Hans-Jurgen Weber. *Mathematical methods for physicists*. Academic Press, 5th edition, 2000.
- [12] S. Babin, A. Bugrov, S. Cabrini, S. Dhuey, A. Goltsov, I. Ivonin, E. B. Kley, C. Peroz, H. Schmidt, and V. Yankov. Digital optical spectrometer-on-chip. *Applied Physics Letters*, 95(4), 2009.
- [13] Tom Baehr-jones, Michael Hochberg, Chris Walker, and Axel Scherer. High-Q optical resonators in silicon-on-insulator-based slot waveguides. *Applied Physics Letters*, 86(081101):1–3, 2005.

- [14] Tom Baehr-Jones, Alexander Spott, Rob Ilic, Andrew Spott, Boyan Penkov, William Asher, and Michael Hochberg. Silicon-on-sapphire integrated waveguides for the mid-infrared. *Optics Express*, 18(12):12127–12135, 2010.
- [15] William L Barnes. Surface plasmon–polariton length scales: A route to sub-wavelength optics. *Journal of Optics A: Pure and Applied Optics*, 8:S87–S93, 2006.
- [16] Carlos A. Barrios, María José Bañuls, Victoria González-Pedro, Kristinn B. Gylfason, Benito Sánchez, Amadeu Griol, A. Maquieira, H. Sohlström, M. Holgado, and R. Casquel. Label-free optical biosensing with slot-waveguides. *Optics Letters*, 33(7):708, 2008.
- [17] Carlos A. Barrios, Kristinn B. Gylfason, Benito Sánchez, Amadeu Griol, H. Sohlström, M. Holgado, and R. Casquel. Slot-waveguide biochemical sensor. *Optics Letters*, 32(21):3080, 2007.
- [18] Tymon Barwicz and Henry I. Smith. Evolution of line-edge roughness during fabrication of high-index-contrast microphotonic devices. *Journal of Vacuum Science & Technology B: Microelectronics and Nanometer Structures*, 21(6):2892–2896, 2003.
- [19] Ana R. Bastos, Carlos M. S. Vicente, Rui Oliveira-Silva, Nuno J. O. Silva, Marta Tacao, Joao P. da Costa, Mario Lima, Paulo S. Andre, and Rute A. S. Ferreira. Integrated optical Mach–Zehnder interferometer based on organic-inorganic hybrids for photonics-on-a-chip biosensing applications. *Sensors*, 18(840):1–11, 2018.
- [20] Jared F Bauters, Martijn J R Heck, Demis John, Daoxin Dai, Ming-chun Tien, Jonathon S Barton, Arne Leinse, René G Heideman, Daniel J Blumenthal, and John E Bowers. Ultra-low-loss high-aspect-ratio Si_3N_4 waveguides. *Optics Express*, 19(4):3163–3174, 2011.
- [21] Pierre Berini. Figures of merit for surface plasmon waveguides. *Optics Express*, 14(26):13030–13042, 2006.
- [22] Aleksandr Biberman and Keren Bergman. Optical interconnection networks for high-performance computing systems. *Reports on Progress in Physics*, 75(4), 2012.
- [23] K. Y. R. Billah and M. Shinozuka. Numerical method for colored-noise generation and its application to a bistable system. *Rapid Communications*, 42(12):7492–7495, 1990.
- [24] Daniel J. Blumenthal, René Heideman, Douwe Geuzebroek, Arne Leinse, and Chris Roeloffzen. Silicon Nitride in Silicon Photonics. *Proceedings of the IEEE*, 106(12):2209–2231, 2018.

- [25] Przemek J Bock, Pavel Cheben, Jens H Schmid, Jean Lapointe, André Delâge, Siegfried Janz, Geof C Aers, Dan-Xia Xu, Adam Densmore, and Trevor J Hall. Subwavelength grating periodic structures in silicon-on-insulator: a new type of microphotonic waveguide. *Optics Express*, 18(19):20251–20262, 2010.
- [26] Wim Bogaerts, Shankar Kumar Selvaraja, Pieter Dumon, Joost Brouckaert, Katrien De Vos, Dries Van Thourhout, and Roel Baets. Silicon-on-insulator spectral filters fabricated with CMOS technology. *IEEE Journal on Selected Topics in Quantum Electronics*, 16(1):33–44, 2010.
- [27] Richard J Bojko, Jing Li, Li He, Tom Baehr-jones, Michael Hochberg, and Yukinori Aida. Electron beam lithography writing strategies for low loss, high confinement silicon optical waveguides. *Journal of Vacuum Science & Technology B: Microelectronics and Nanometer Structures*, 29(6), 2011.
- [28] Matthew Borselli, Thomas J Johnson, and Oskar Painter. Beyond the Rayleigh scattering limit in high-Q silicon microdisks: theory and experiment. *Optics Express*, 13(5):1515–1530, 2005.
- [29] Giuseppe Calafiore, Alexander Koshelev, Scott Dhuey, Alexander Goltsov, Pavel Sasorov, Sergey Babin, Vladimir Yankov, Stefano Cabrini, and Christophe Peroz. Holographic planar lightwave circuit for on-chip spectroscopy. *Light: Science and Applications*, 3(9), 2015.
- [30] Manuel Caño-García, David Poudereux, Fernando J. Gordo, Morten A. Geday, José M. Otón, and Xabier Quintana. Integrated Mach-Zehnder interferometer based on liquid crystal evanescent field tuning. *Crystals*, 9(225), 2019.
- [31] C. F. Carlborg, K. B. Gylfason, A. Kaźmierczak, F. Dortu, M. J. Bañuls Polo, A. Maquieira Catala, G. M. Kresbach, H. Sohlström, T. Moh, L. Vivien, J. Popplewell, G. Ronan, C. A. Barrios, G. Stemme, and W. van der Wijngaart. A packaged optical slot-waveguide ring resonator sensor array for multiplex label-free assays in labs-on-chips. *Lab Chip*, 10(3):281–290, 2010.
- [32] Yu-Chi Chang, Vincent Paeder, Lubos Hvozدارa, Jean-Michel Hartmann, and Hans Peter Herzig. Low-loss germanium strip waveguides on silicon for the mid-infrared. *Optics Letters*, 37(14):2883–2885, 2012.
- [33] Tien-Hsin Chao and David P. Casasent. Optical pattern recognition XIX. In *Proceedings of SPIE - The International Society for Optical Engineering*, page 69770P, 2008.
- [34] P. Cheben, J. H. Schmid, A. Delâge, A. Densmore, S. Janz, B. Lamontagne, J. Lapointe, E. Post, P. Waldron, and D.-X. Xu. A high-resolution silicon-on-insulator arrayed waveguide grating microspectrometer with sub-micrometer aperture waveguides. *Optics Express*, 15(5):2299–2306, 2007.

- [35] Lukas Chrostowski and Michael Hochberg. *Silicon Photonics Design: From Devices to Systems*. Cambridge University Press, 1st editio edition, 2015.
- [36] Shun Lien Chuang. *Physics of Photonic Devices*. John Wiley & Sons, Inc., Hoboken, New Jersey, 2nd edition, 2009.
- [37] Tom Claes, Jordi Gironès Molera, Katrien De Vos, Etienne Schacht, Roel Baets, and Peter Bienstman. Label-free biosensing with a slot-waveguide-based ring resonator in silicon on insulator. *IEEE Photonics Journal*, 1(3):197–204, 2009.
- [38] Larry A. Coldren, Scott W. Corzine, and Milan L. Masanovic. *Diode Lasers and Photonic Integrated Circuits*. John Wiley & Sons, Inc., Hoboken, New Jersey, 2nd edition, 2012.
- [39] V. Constantoudis, G. P. Patsis, A. Tserepi, and E. Gogolides. Quantification of line-edge roughness of photoresists. II. Scaling and fractal analysis and the best roughness descriptors. *Journal of Vacuum Science & Technology B: Microelectronics and Nanometer Structures*, 21(3):1019, 2003.
- [40] David A. Coucheron, Dushan N. Wadduwage, G. Senthil Murugan, Peter T.C. So, and Balpreet S. Ahluwalia. Chip-Based Resonance Raman Spectroscopy Using Tantalum Pentoxide Waveguides. *IEEE Photonics Technology Letters*, 31(14):1127–1130, 2019.
- [41] Kapil Debnath, Ali Z Khokhar, Stuart A Boden, Hideo Arimoto, Swe Zin Oo, Harold M H Chong, Graham T Reed, and Shinichi Saito. Low-loss slot waveguides with silicon (111) surfaces realized using anisotropic wet etching. *Frontiers in Materials*, 3(November):1–5, 2016.
- [42] Francesco Dell’Olio and Vittorio M Passaro. Optical sensing by optimized silicon slot waveguides. *Optics Express*, 15(8):4977, 2007.
- [43] Qingzhong Deng, Lu Liu, Xinbai Li, Jurgen Michel, and Zhiping Zhou. Linear-regression-based approach for loss extraction from ring resonators. *Optics Letters*, 41(20):4747–4750, 2016.
- [44] Qingzhong Deng, Qiaojing Yan, Lu Liu, Xinbai Li, Jurgen Michel, and Zhiping Zhou. Robust polarization-insensitive strip-slot waveguide mode converter based on symmetric multimode interference. *Optics Express*, 24(7):7347, 2016.
- [45] A. Densmore, M. Vachon, D.-X. Xu, S. Janz, R. Ma, Y.-H. Li, G. Lopinski, A. Delâge, J. Lapointe, C. C. Luebbert, Q. Y. Liu, P. Cheben, and J. H. Schmid. Silicon photonic wire biosensor array for multiplexed real-time and label-free molecular detection. *Optics Letters*, 34(23):3598, 2009.
- [46] Ashim Dhakal, Frédéric Peyskens, Ananth Z Subramanian, Nicolas Le Thomas, and Roel Baets. Enhancement of light absorption, scattering and emission in high index contrast waveguides. In *OSA Advanced Photonics Congress*, pages 1–3, 2013.

- [47] Ashim Dhakal, Ali Raza, Frédéric Peyskens, Ananth Z. Subramanian, Stéphane Clemmen, Nicolas Le Thomas, and Roel Baets. Efficiency of evanescent excitation and collection of spontaneous Raman scattering near high index contrast channel waveguides. *Optics Express*, 23(21):27391, 2015.
- [48] Ashim Dhakal, Ananth Z Subramanian, Pieter Wuytens, Frédéric Peyskens, Nicolas Le Thomas, and Roel Baets. Evanescent excitation and collection of spontaneous Raman spectra using silicon nitride nanophotonic waveguides. *Optics Letters*, 39(13):4025–4028, 2014.
- [49] Ashim Dhakal, Pieter Wuytens, Ali Raza, Nicolas Le Thomas, and Roel Baets. Silicon Nitride Background in Nanophotonic Waveguide Enhanced Raman Spectroscopy. *Materials*, 10(140), 2017.
- [50] Ashim Dhakal, Pieter C. Wuytens, Frederic Peyskens, Karolien Jans, Nicolas Le Thomas, and Roel Baets. Nanophotonic Waveguide Enhanced Raman Spectroscopy of Biological Submonolayers. *ACS Photonics*, 3(11), 2016.
- [51] R Ding, T Baehr-Jones, Y Liu, R Bojko, J Witzens, S Huang, J Luo, S Benight, P Sullivan, J-M Fedeli, M Fournier, L Dalton, A Jen, and M Hochberg. Demonstration of a low $V\pi L$ modulator with GHz bandwidth based on electro-optic polymer-clad silicon slot waveguides. *Optics Express*, 18(15):15618–15623, 2010.
- [52] Ran Ding, Tom Baehr-jones, Woo-Joong Kim, Xugang Xiong, Richard Bojko, Jean-Marc Fedeli, Maryse Fournier, and Michael Hochberg. Low-loss strip-loaded slot waveguides in silicon-on-insulator. *Optics Express*, 18(24):25061–25067, 2010.
- [53] Christopher Doerr and Long Chen. Silicon Photonics in Optical Coherent Systems. *Proceedings of the IEEE*, 106(12):2291–2301, 2018.
- [54] Christopher R. Doerr. Silicon photonic integration in telecommunications. *Frontiers in Physics*, 3:37, 2015.
- [55] Wolfgang Drexler and James G. Fujimoto, editors. *Optical Coherence Tomography Technology and Applications*. Springer, 2nd edition, 2015.
- [56] Qingyang Du, Yizhong Huang, Okechukwu Ogbuu, Wei Zhang, Junying Li, Vivek Singh, Anuradha M. Agarwal, and Juejun Hu. Gamma radiation effects in amorphous silicon and silicon nitride photonic devices. *Optics Letters*, 42(3):587–590, 2017.
- [57] Firehun Tsige Dullo, Susan Lindecrantz, J Jana, Jørn H Hansen, Magnus Engqvist, Stian Andre Solbø, and Gaute Hellesø. Sensitive on-chip methane detection with a cryptophane-A cladded Mach-Zehnder interferometer. *Optics Express*, 23(24):31564–31573, 2015.

- [58] Pieter Dumon, Wim Bogaerts, Vincent Wiaux, Johan Wouters, Stephan Beckx, Joris Van Campenhout, Dirk Taillaert, Bert Luyssaert, Peter Bienstman, and Dries Van Thourhout. Low-loss SOI photonic wires and ring resonators fabricated with deep UV lithography. *IEEE Photonics Technology Letters*, 16(5):1328–1330, 2004.
- [59] Brian A. Eckenrode, Edward G. Bartick, Scott D. Harvey, Mark E. Vucelick, Bob W. Wright, and Rebecca A. Huff. Raman spectrum of acetaminophen.
- [60] Benjamin Eggleton, Barry Luther-Davies, and Kathleen Richardson. Chalcogenide photonics. *Nature Photonics*, 5:141–148, dec 2011.
- [61] Christopher C Evans, Chengyu Liu, and Jin Suntivich. Low-loss titanium dioxide waveguides and resonators using a dielectric lift-off fabrication process. *Optics Express*, 23(9):11160–11169, 2015.
- [62] Christopher C. Evans, Chengyu Liu, and Jin Suntivich. TiO₂ nanophotonic sensors for efficient integrated evanescent Raman spectroscopy. *ACS Photonics*, 3(9):1662–1669, 2016.
- [63] John R. Ferraro. *Introductory raman spectroscopy*. Academic Press, 2nd edition, 2002.
- [64] Jonas Flueckiger, Shon Schmidt, Valentina Donzella, Ahmed Sherwali, Daniel M. Ratner, Lukas Chrostowski, and Karen C. Cheung. Sub-wavelength grating for enhanced ring resonator biosensor. *Optics Express*, 24(14):15672, 2016.
- [65] Xuetao Gan, Nadia Pervez, Ioannis Kymissis, Fariba Hatami, and Dirk Englund. A high-resolution spectrometer based on a compact planar two dimensional photonic crystal cavity array. *Applied Physics Letters*, 100(23), 2012.
- [66] Sinha G. Gaurav. *Silicon Photonics: Technologies and Global Markets*. Technical report, BCC Publishing, 2017.
- [67] M Gnan, S Thoms, D S Macintyre, R M De La Rue, and M Sorel. Fabrication of low-loss photonic wires in silicon-on-insulator using hydrogen silsesquioxane electron-beam resist. *Electronics Letters*, 44(2):115–116, 2008.
- [68] Peter R. Griffiths and James A. De Haseth. *Fourier Transform Infrared Spectrometry*. Wiley, 2nd edition, 2007.
- [69] Ruimin Guo, Bing Wang, Xingjun Wang, Lei Wang, Lingjun Jiang, and Zhiping Zhou. Optical amplification in Er/Yb silicate slot waveguide. *Optics Letters*, 37(9):1427–1429, 2012.
- [70] V. L. Gupta and Enakshi K. Sharma. Metal-clad and absorptive multilayer waveguides: an accurate perturbation analysis. *Journal of the Optical Society of America*, 9(6):953–956, 1992.

- [71] Peter Hanggi and Peter Jung. Colored noise in dynamical-systems. In *Advances in Chemical Physics*, pages 239–326. John Wiley & Sons, Inc., 1994.
- [72] Niranjana M. Hanumegowda, Caleb J. Stica, Bijal C. Patel, Ian White, and Xudong Fan. Refractometric sensors based on microsphere resonators. *Applied Physics Letters*, 87(20):201107, 2005.
- [73] Nicholas C. Harris, Davide Grassani, Angelica Simbula, Mihir Pant, Matteo Galli, Tom Baehr-Jones, Michael Hochberg, Dirk Englund, Daniele Bajoni, and Christophe Galland. Integrated source of spectrally filtered correlated photons for large-scale quantum photonic systems. *Physical Review X*, 4(4):041407, 2014.
- [74] Nicholas C Harris, Yangjin Ma, Jacob Mower, Tom Baehr-jones, Dirk Englund, Michael Hochberg, and Christophe Galland. Efficient, compact and low loss thermo-optic phase shifter in silicon. *Optics Express*, 22(9):10487–10493, 2014.
- [75] M. Harwit. *Hadamard transform optics*. Elsevier, 2012.
- [76] Martijn J.R. Heck. Highly integrated optical phased arrays: photonic integrated circuits for optical beam shaping and beam steering. *Nanophotonics*, 6(1):93–107, 2017.
- [77] R G Heideman and P V Lambeck. Remote opto-chemical sensing with extreme sensitivity: Design, fabrication and performance of a pigtailed integrated optical phase-modulated Mach–Zehnder interferometer system. *Sensors and Actuators, B: Chemical*, 61:100–127, 1990.
- [78] Alaine Herrero-Bermello, Aitor V. Velasco, Hugh Podmore, Pavel Cheben, Jens H. Schmid, Siegfried Janz, María L. Calvo, Dan-Xia Xu, Alan Scott, and Pedro Corredera. Temperature dependence mitigation in stationary Fourier-transform on-chip spectrometers. *Optics Letters*, 42(11):2239, 2017.
- [79] Scott A. Holmstrom, Todd H. Stievater, Dmitry A. Kozak, Marcel W. Pruessner, Nathan Tyndall, William S Rabinovich, R Andrew McGill, and Jacob B Khurgin. Trace gas Raman spectroscopy using functionalized waveguides. *Optica*, 3(8):891–896, 2016.
- [80] Juejun Hu, Nathan Carlie, Laetitia Petit, Anu Agarwal, Kathleen Richardson, and Lionel C. Kimerling. Cavity-enhanced infrared absorption in planar chalcogenide glass microdisk resonators: Experiment and analysis. *Journal of Lightwave Technology*, 27(23):5240–5245, 2009.
- [81] Juejun Hu, Xiaochen Sun, Anu Agarwal, and Lionel C Kimerling. Design guidelines for optical resonator biochemical sensors. *Journal of the Optical Society of America*, 26(5):1032–1041, 2009.

- [82] Juejun Hu, Vladimir Tarasov, Nathan Carlie, Ning-Ning Feng, Laeticia Petit, Anu Agarwal, Kathleen Richardson, and Lionel Kimerling. Si-CMOS-compatible lift-off fabrication of low-loss planar chalcogenide waveguides. *Optics Express*, 15(19):11798–11807, 2007.
- [83] Lijun Huang, Huiping Tian, Daquan Yang, Jian Zhou, Qi Liu, Pan Zhang, and Yuefeng Ji. Optimization of figure of merit in label-free biochemical sensors by designing a ring defect coupled resonator. *Optics Communications*, 332:42–49, 2014.
- [84] Maidul Islam, Dibakar Roy Chowdhury, Amir Ahmad, and Gagan Kumar. Terahertz plasmonic waveguide based thin film sensor. *Journal of Lightwave Technology*, 35(23):5215–5221, 2017.
- [85] E. Jaberansary, T. M B Masaud, M. M. Milosevic, M. Nedeljkovic, G. Z. Mashanovich, and H. M H Chong. Scattering loss estimation using 2-D Fourier analysis and modeling of sidewall roughness on optical waveguides. *IEEE Photonics Journal*, 5(3), 2013.
- [86] John David Jackson. *Classical electrodynamics*. John Wiley & Sons, Inc., 3rd edition, 1999.
- [87] S. G. Johnson, M. L. Povinelli, M. Soljacic, A. Karalis, S. Jacobs, and J. D. Joannopoulos. Roughness losses and volume-current methods in photonic-crystal waveguides. *Applied Physics B: Lasers and Optics*, 81(2-3):283–293, 2005.
- [88] Steven Johnson, M. Ibanescu, M. Skorobogatiy, O. Weisberg, J. Joannopoulos, and Y. Fink. Perturbation theory for Maxwell’s equations with shifting material boundaries. *Physical Review E*, 65(6):066611, jun 2002.
- [89] Steven Johnson and John Joannopoulos. Block-iterative frequency-domain methods for Maxwell’s equations in a planewave basis. *Optics Express*, 8(3):173, 2001.
- [90] Steven G. Johnson, Mihai Ibanescu, M. Skorobogatiy, Ori Weisberg, Torkel Engeness, Marin Soljačić, Steven Jacobs, J. Joannopoulos, and Yoel Fink. Low-loss asymptotically single-mode propagation in large-core OmniGuide fibers. *Optics Express*, 9(13):748–779, 2001.
- [91] Young Chul Jun, Ryan M Briggs, Harry A Atwater, and Mark L Brongersma. Broadband enhancement of light emission in silicon slot waveguides. *Optics Express*, 17(9):7479–7490, 2009.
- [92] N. Jeremy Kasin. Discrete simulation of colored noise and stochastic processes and $1/f^\alpha$ power law noise generation. *Proceedings of the IEEE*, 83(5):802–827, 1995.

- [93] Muhammad Umar Khan, Yufei Xing, Yinghao Ye, and Wim Bogaerts. Photonic Integrated Circuit Design in a Foundry + Fabless Ecosystem. *IEEE Journal of Selected Topics in Quantum Electronics*, 25(5), 2019.
- [94] Derek M. Kita, Hongtao Lin, Anu Agarwal, Kathleen Richardson, Igor Luzinov, Tian Gu, and Juejun Hu. On-chip infrared spectroscopic sensing: redefining the benefits of scaling. *IEEE Journal of Selected Topics in Quantum Electronics*, 23(2), 2017.
- [95] Derek M. Kita, Jérôme Michon, Steven G. Johnson, and Juejun Hu. Are slot and sub-wavelength grating waveguides better than strip waveguides for sensing? *Optica*, 5(9):1046–1054, 2018.
- [96] Derek M. Kita, Carlos Rios, and Juejun Hu. Performance Optimization Strategies for Nanophotonic Digital Fourier Transform Spectrometers. In *Optical Sensors and Sensing Congress (ES, FTS, HISE, Sensors)*, OSA Technical Digest (Optical Society of America, 2019), page FTu4B.5. 2019.
- [97] Christian Koos, P Vorreau, T Vallaitis, P Dumon, W Bogaerts, R Baets, B Esembeson, I Biaggio, T Michinobu, F Diederich, W Freude, and J Leuthold. All-optical high-speed signal processing with silicon–organic hybrid slot waveguides. *Nature Photonics*, 3(April):216–219, 2009.
- [98] Peter Kozma, Florian Kehl, Eva Ehrentreich-Förster, Christoph Stamm, and Frank F Bier. Biosensors and bioelectronics integrated planar optical waveguide interferometer biosensors : A comparative review. *Biosensors and Bioelectronics*, 58:287–307, 2014.
- [99] Arun Kumar, S. I. Hosain, and A. K. Ghatak. Propagation characteristics of weakly guiding lossy fibres: An exact and perturbation analysis. *Optica Acta*, 28(4):559–566, 1981.
- [100] BBC Kyotoku, Long Chen, and Michal Lipson. Sub-nm resolution cavity enhanced microspectrometer. *Optics Express*, 18(1):102–107, 2010.
- [101] J. P. R. Lacey and F. P. Payne. Radiation loss from planar waveguides with random wall imperfections. *IEEE Proceedings*, 137(4):282–288, 1990.
- [102] Etienne Le Coarer, Sylvain Blaize, Pierre Benech, Ilan Stefanon, Alain Morand, Gilles Léronnel, Grégory Leblond, Pierre Kern, Jean Marc Fedeli, and Pascal Royer. Wavelength-scale stationary-wave integrated Fourier-transform spectrometry. *Nature Photonics*, 1(8):473–478, 2007.
- [103] Nicolas Le Thomas, Ashim Dhakal, Ali Raza, Frédéric Peyskens, and Roel Baets. Impact of fundamental thermodynamic fluctuations on light propagating in photonic waveguides made of amorphous materials. *Optica*, 5(4):328–336, 2018.

- [104] Dong Ho Lee, Sung Joong Choo, Uiseok Jung, Kyung Woon Lee, Kwang Woong Kim, and Jung Ho Park. Low-loss silicon waveguides with sidewall roughness reduction using a SiO₂ hard mask and fluorine-based dry etching. *Journal of Micromechanics and Microengineering*, 25(1), 2015.
- [105] Hansuek Lee, Tong Chen, Jiang Li, Oskar Painter, and Kerry J Vahala. Ultra-low-loss optical delay line on a silicon chip. *Nature Communications*, 3(May):867, 2012.
- [106] Kevin K Lee, Desmond R Lim, and Lionel C Kimerling. Fabrication of ultralow-loss Si/SiO₂ waveguides by roughness reduction. *Optics Letters*, 26(23):1888–1890, 2001.
- [107] Kevin K Lee, Desmond R Lim, Hsin-Chiao Luan, Anuradha Agarwal, James Foresi, and Lionel C Kimerling. Effect of size and roughness on light transmission in a Si/SiO₂ waveguide: Experiments and model. *Applied Physics Letters*, 77(11):1617–1619, 2000.
- [108] Jinyang Li, Dan-feng Lu, and Zhi-mei Qi. Miniature Fourier transform spectrometer based on wavelength dependence of half-wave voltage of a LiNbO₃ waveguide interferometer. *Optics Letters*, 39(13):3923–3926, 2014.
- [109] Qing Li, Ali A Eftekhari, Zhixuan Xia, and Ali Adibi. Azimuthal-order variations of surface-roughness-induced mode splitting and scattering loss in high-Q microdisk resonators. *Optics letters*, 37(9):1586–1588, 2012.
- [110] Andreas C. Liapis, Boshen Gao, Mahmudur R. Siddiqui, Zhimin Shi, and Robert W. Boyd. On-chip spectroscopy with thermally tuned high-Q photonic crystal cavities. *Applied Physics Letters*, 108(2), 2016.
- [111] Andy Eu-Jin Lim, Tsung-Yang Liow, Jun-Feng Song, Ming-Bin Yu, Chao Li, Xiao-Guang Tu, Kok-Kiong Chen, Roger Poh-Cher Tern, Ying Huang, Xian-Shu Luo, and Guo-Qiang Lo. *Path to Silicon Photonics Commercialization: The Foundry Model Discussion*, pages 191–215. Springer Berlin Heidelberg, Berlin, Heidelberg, 2016.
- [112] Andy Eu-Jin Lim, Junfeng Song, Qing Fang, Chao Li, Xiaoguang Tu, Ning Duan, Kok Kiong Chen, Roger Poh Cher Tern, and Tsung Yang Liow. Review of Silicon Photonics Foundry Efforts. *IEEE Journal of Selected Topics in Quantum Electronics*, 20(4):405–416, 2014.
- [113] Hongtao Lin, Zhengqian Luo, Tian Gu, Lionel C. Kimerling, Kazumi Wada, Anu Agarwal, and Juejun Hu. Mid-infrared integrated photonics on silicon: A perspective. *Nanophotonics*, 7(2), 2017.
- [114] Qiankun Liu, Joan Manel Ramirez, Vladyslav Vakarin, Xavier Le Roux, Andrea Ballabio, Jacopo Frigerio, Daniel Chrastina, Giovanni Isella, David Bouville, Laurent Vivien, Carlos Alonso Ramos, and Delphine Marris-Morini. Mid-

- infrared sensing between 5.2 and 6.6 μm wavelengths using Ge-rich SiGe waveguides. *Optical Materials Express*, 8(5):1305–1312, 2018.
- [115] Qing Liu, Xiaoguang Tu, Kyung Woo Kim, Jack Sheng Kee, Yong Shin, Kyung-sup Han, Yong Jin Yoon, Guo Qiang Lo, and Mi Kyoung Park. Highly sensitive Mach–Zehnder interferometer biosensor based on silicon nitride slot waveguide. *Sensors and Actuators, B: Chemical*, 188:681–688, 2013.
- [116] Hua Lu, Xueming Liu, Dong Mao, and Guoxi Wang. Plasmonic nanosensor based on Fano resonance in waveguide-coupled resonators. *Optics Letters*, 37(18):3780–3782, 2012.
- [117] Kun Lu and Jing-Dong Bao. Numerical simulation of generalized Langevin equation with arbitrary correlated noise. *Physical Review E*, 72(067701):1–4, 2005.
- [118] Xiao Ma, Mingyu Li, and Jian Jun He. CMOS-compatible integrated spectrometer based on echelle diffraction grating and MSM photodetector array. *IEEE Photonics Journal*, 5(2), 2013.
- [119] Dietrich Marcuse. Mode conversion caused by surface imperfections of a dielectric slab waveguide. *The Bell System Technical Journal*, (December):3187–3215, 1969.
- [120] David Marpaung, Jianping Yao, and José Capmany. Integrated microwave photonics. *Nature Photonics*, 13:80–90, 2019.
- [121] R C McPhedran, L C Botten, J Mcorist, A A Asatryan, C M De Sterke, and N A Nicorovici. Density of states functions for photonic crystals. *Physical Review E*, 69(016609):1–16, 2004.
- [122] D. Melati, A. Melloni, and F. Morichetti. Real photonic waveguides: Guiding light through imperfections. *Advances in Optics and Photonics*, 6:131, 2014.
- [123] Fan Meng, Ren-Jye Shiue, Noel Wan, Luozhou Li, Jing Nie, Nicholas C Harris, Edward H Chen, Tim Schröder, Nadia Pervez, Ioannis Kymissis, Dirk Englund, Nadia Pervez, Ioannis Kymissis, and Dirk Englund. Waveguide-integrated photonic crystal spectrometer with camera readout. *Applied Physics Letters*, 105(051103), 2014.
- [124] David A. B. Miller. Perfect optics with imperfect components. *Optica*, 2(8):747, 2015.
- [125] Francesco Morichetti, Antonio Canciamilla, Carlo Ferrari, Matteo Torregiani, Andrea Melloni, and Mario Martinelli. Roughness induced backscattering in optical silicon waveguides. *Physical Review Letters*, 104(3):1–4, 2010.

- [126] M Muneeb, X Chen, P Verheyen, G Lepage, S Pathak, E Ryckeboer, A Malik, B Kuyken, M Nedeljkovic, J Van Campenhout, G Z Mashanovich, and G Roelkens. Demonstration of silicon-on-insulator mid-infrared spectrometers operating at $3.8 \mu\text{m}$. *Optics Express*, 21(10):11659–11669, 2013.
- [127] M. Muneeb, A. Vasiliev, A. Ruocco, A. Malik, H. Chen, M. Nedeljkovic, J. S. Penades, L. Cerutti, J. B. Rodriguez, G. Z. Mashanovich, M. K. Smit, E. Tourni, and G. Roelkens. III-V-on-silicon integrated micro - spectrometer for the $3 \mu\text{m}$ wavelength range. *Optics Express*, 24(9):9465–9472, 2016.
- [128] Behnam Naghdi and Lawrence R. Chen. Silicon photonic contradirectional couplers using subwavelength grating waveguides. *Optics Express*, 24(20):23429–23438, 2016.
- [129] Behnam Naghdi and Lawrence R. Chen. Spectral engineering of subwavelength-grating-based contradirectional couplers. *Optics Express*, 25(21):25310–25317, 2017.
- [130] Milos Nedeljkovic, Aitor V Velasco, Ali Z Khokhar, André Delâge, Pavel Cheben, and Goran Z Mashanovich. Mid-infrared silicon-on-insulator Fourier-transform spectrometer chip. *IEEE Photonics Technology Letters*, 28(4):528–531, 2016.
- [131] Xiaomin Nie, Nina Turk, Yang Li, Zuyang Liu, and Roel Baets. High extinction ratio on-chip pump-rejection filter based on cascaded grating-assisted contradirectional couplers in silicon nitride rib waveguides. *Optics Letters*, 44(9):2310–2313, 2019.
- [132] Arthur Nitkowski, Antje Baeumner, and Michal Lipson. On-chip spectrophotometry for bioanalysis using microring resonators. *Biomedical Optics Express*, 2(2):271–277, jan 2011.
- [133] Peter Offermans, Martijn C. Schaafsma, Said R. K. Rodriguez, Yichen Zhang, Mercedes Crego-Calama, Sywert H. Brongersma, and Jaime Gomez Rivas. Universal scaling of the figure of merit of plasmonic sensors. *ACS Nano*, 5(6):5151–5157, 2011.
- [134] Alan V. Oppenheim, Ronald W. Schafer, and John R. Buck. *Discrete-time signal processing*. Prentice-Hall, Inc., Upper Saddle River, New Jersey, 2nd edition, 1999.
- [135] Dorian Oser, Florent Mazeas, Xavier Le Roux, Diego Pérez-Galacho, Olivier Alibart, Sébastien Tanzilli, Laurent Labonté, Delphine Marris-Morini, Laurent Vivien, Éric Cassan, and Carlos Alonso-Ramos. Coherency-Broken Bragg Filters: Overcoming On-Chip Rejection Limitations. *Laser & Photonics Reviews*, 13(1800226):1–8, 2019.

- [136] Ardavan Oskooi and Steven G Johnson. *Chapter 4: Electromagnetic Wave Source Conditions*. Artech House, 2013.
- [137] Ardavan F. Oskooi, David Roundy, Mihai Ibanescu, Peter Bermel, J. D. Joannopoulos, and Steven G. Johnson. Meep: A flexible free-software package for electromagnetic simulations by the FDTD method. *Computer Physics Communications*, 181(3):687–702, 2010.
- [138] Zorica Pantic and Raj Mittra. Quasi-TEM analysis of microwave transmission lines by the finite-element method. *IEEE Transactions on Microwave Theory and Techniques*, MTT-34(11):1096–1103, 1986.
- [139] Vittorio Passaro, Benedetto Troia, Mario La Notte, and Francesco De Leonardis. Photonic resonant microcavities for chemical and biochemical sensing. *RSC Advances*, 3:25–44, 2012.
- [140] Shibnath Pathak. *Silicon Nano-Photonics based Arrayed Waveguide Gratings*. PhD thesis, Ghent University, 2014.
- [141] G. P. Patsis, V. Constantoudis, A. Tserepi, E. Gogolides, and G. Grozev. Quantification of line-edge roughness of photoresists. I. A comparison between off-line and on-line analysis of top-down scanning electron microscopy images. *Journal of Vacuum Science & Technology B: Microelectronics and Nanometer Structures*, 21(3):1008, 2003.
- [142] F.P. Payne and J. P. R. Lacey. A theoretical analysis of scattering loss from planar optical waveguides. *Optical and Quantum Electronics*, 26:977–986, 1994.
- [143] Daniel Pérez, Juan Fernández, Rocío Baños, José David Doménech, Ana M. Sánchez, Josep M. Cirera, Roser Mas, Javier Sánchez, Sara Durán, Emilio Pardo, Carlos Domínguez, Daniel Pastor, José Capmany, and Pascual Muñoz. Thermal tuners on a Silicon Nitride platform. 2016.
- [144] Martin H. P. Pfeiffer, Junqiu Liu, Arslan S. Raja, Tiago Morais, Bahareh Ghadiani, and Tobias J. Kippenberg. Ultra-smooth silicon nitride waveguides based on the Damascene reflow process: fabrication and loss origins. *Optica*, 5(7):884–892, 2018.
- [145] Molly Piels and Darko Zibar. Compact silicon multimode waveguide spectrometer with enhanced bandwidth. *Scientific Reports*, 7:1–7, 2017.
- [146] Thierry Pinguet, Scott Denton, Steffen Gloeckner, Michael Mack, Gianlorenzo Masini, Attila Mekis, Simon Pang, Mark Peterson, Subal Sahni, and Peter De Dobbelaere. High-Volume Manufacturing Platform for Silicon Photonics. *Proceedings of the IEEE*, 106(12):2281–2290, 2018.
- [147] Hugh Podmore, Alan Scott, Pavel Cheben, Aitor V. Velasco, Jens H. Schmid, Martin Vachon, and Regina Lee. Demonstration of a compressive-sensing Fourier-transform on-chip spectrometer. *Optics Letters*, 42(7):1440–1443, 2017.

- [148] Christopher V. Poulton, Ami Yaacobi, David B. Cole, Matthew J. Byrd, Manan Raval, Diedrik Vermeulen, and Michael R. Watts. Coherent solid-state LIDAR with silicon photonic optical phased arrays. *Optics Letters*, 42(20):4091–4094, 2017.
- [149] Abdul Rahim, Jeroen Goyvaerts, Bertrand Szelag, Jean-Marc Fedeli, Philippe Absil, Timo Aalto, Mikko Harjanne, Callum Littlejohns, Graham Reed, Georg Winzer, Stefan Lischke, Lars Zimmermann, Dieter Knoll, Douwe Geuzebroek, Arne Leinse, Michael Geiselmann, Michael Zervas, Hilde Jans, Andim Stassen, Carlos Dominguez, Pascual Munoz, David Domenech, Anna Lena Giesecke, Max C. Lemme, and Roel Baets. Open-access silicon photonics platforms in Europe. *IEEE Journal of Selected Topics in Quantum Electronics*, 25(5), 2019.
- [150] Abdul Rahim, Eva Ryckeboer, Ananth Z Subramanian, Stephane Clemmen, Bart Kuyken, Ashim Dhakal, Ali Raza, Artur Hermans, Muhammad Muneeb, Soren Dhoore, Yanlu Li, Utsav Dave, Peter Bienstman, Nicolas Le Thomas, Gunther Roelkens, Dries Van Thourhout, Philippe Helin, Simone Severi, Xavier Rottenberg, and Roel Baets. Expanding the Silicon Photonics Portfolio With Silicon Nitride Photonic Integrated Circuits. *Journal of Lightwave Technology*, 35(4):639–649, 2017.
- [151] Anand Ramaswamy, Leif A. Johansson, Jonathan Klamkin, Hsu Feng Chou, Colin Sheldon, Mark J. Rodwell, Larry A. Coldren, and John E. Bowers. Integrated coherent receivers for high-linearity microwave photonic links. *Journal of Lightwave Technology*, 26(1):209–216, 2008.
- [152] Ali Raza, Stephane Clemmen, Pieter Wuytens, Michiel De Goede, Amy S. K. Tong, Nicolas Le Thomas, Chengyu Liu, Jin Suntivich, Andre G. Skirtach, Sonia M. Garcia-Blanco, Daniel J. Blumenthal, James S. Wilkinson, and Roel Baets. High index contrast photonic platforms for on-chip Raman spectroscopy. *Optics Express*, 27(16):23067–23079, 2019.
- [153] Ali Raza, Stéphane Clemmen, Pieter Wuytens, Muhammad Muneeb, Michiel Van Daele, Jolien Dendooven, Christophe Detavernier, Andre Skirtach, and Roel Baets. ALD assisted nanoplasmonic slot waveguide for on-chip enhanced Raman spectroscopy. *APL Photonics*, 3:116105, 2018.
- [154] Brandon Redding, Seng Fatt Liew, Yaron Bromberg, Raktim Sarma, and Hui Cao. Evanescently coupled multimode spiral spectrometer. *Optica*, 3(9):956–962, 2016.
- [155] Brandon Redding, Seng Fatt Liew, Raktim Sarma, and Hui Cao. Compact spectrometer based on a disordered photonic chip. *Nature Photonics*, 7(9):746–751, 2013.
- [156] Carlos Ríos, Matthias Stegmaier, Peiman Hosseini, Di Wang, Torsten Scherer, C David Wright, Harish Bhaskaran, and Wolfram H P Pernice. Integrated all-photonic non-volatile multi-level memory. *Nature Photonics*, 9:725–732, 2015.

- [157] Jacob T Robinson, Kyle Preston, Oskar Painter, and Michal Lipson. First-principle derivation of gain in high-index-contrast waveguides. *Optics Express*, 16(21):16659–16669, 2008.
- [158] Chris G. H. Roeloffzen, Leimeng Zhuang, Caterina Taddei, Arne Leinse, René G. Heideman, Paulus W. L. van Dijk, Ruud M. Oldenbeuving, David A. I. Marpaung, Maurizio Burla, and Klaus J. Boller. Silicon nitride microwave photonic circuits. *Optics Express*, 21(19):22937–22961, 2013.
- [159] E Ryckeboer, R Bockstaele, M Vanslembrouck, and R Baets. Glucose sensing by waveguide-based absorption spectroscopy on a silicon chip. *Biomedical Optics Express*, 5(5):1636–48, may 2014.
- [160] E Ryckeboer, A Gassenq, M Muneeb, N Hattasan, W Bogaerts, L Cerutti, J B Rodriguez, and E Tournié. Silicon-on-insulator spectrometers with integrated GaInAsSb photodiodes for wide-band spectroscopy from 1510 to 2300 nm. *Optics Express*, 21(5):6101–6108, 2013.
- [161] M.C. Saleh, B.E.A. and Teich. *Fundamentals of Photonics*. John Wiley & Sons, Inc., 2nd edition, 2007.
- [162] Stefano Sardo, Fabrizio Giacometti, Sergio Doneda, Umberto Colombo, Melissa Di, Anna Donghi, Romano Morson, Giorgio Mutinati, Alessandro Nottola, Massimo Gentili, and Maria Chiara Ubaldi. Line edge roughness (LER) reduction strategy for SOI waveguides fabrication. *Microelectronic Engineering*, 85:1210–1213, 2008.
- [163] S. Shalev-Shwartz and S. Ben-David. *Understanding machine learning: From theory to algorithms*. Cambridge University Press, 2014.
- [164] Michael J. Shaw, Junpeng Guo, Gregory A. Vawter, Scott Habermehl, and Charles T. Sullivan. Fabrication techniques for low-loss silicon nitride waveguides. In Eric G. Johnson Suleski, Gregory P. Nordin, and Thomas J., editors, *Micromachining Technology for Micro-Optics and Nano-Optics III*, volume 5720, pages 109–118. SPIE, 2005.
- [165] Shou Xian She. Propagation loss in metal-clad waveguides and weakly absorptive waveguides by a perturbation method. *Optics Letters*, 15(16):900–902, 1990.
- [166] Yichen Shen, Nicholas C Harris, Scott Skirlo, Mihika Prabhu, Tom Baehr-Jones, Michael Hochberg, Xin Sun, Shijie Zhao, Hugo Larochelle, Dirk Englund, and Marin Soljačić. Deep learning with coherent nanophotonic circuits. *Nature Photonics*, 11:441–447, 2017.
- [167] Joshua W. Silverstone, Damien Bonneau, Jeremy L. O’Brien, and Mark G. Thompson. Silicon quantum photonics. *IEEE Journal of Selected Topics in Quantum Electronics*, 22(6):390–402, 2016.

- [168] Vivek Singh, Pao Tai Lin, Neil Patel, Hongtao Lin, Lan Li, Yi Zou, Fei Deng, Chaoying Ni, Juejun Hu, James Giammarco, Anna Paola Soliani, Bogdan Zdyrko, Igor Luzinov, Spencer Novak, Jackie Novak, Peter Wachtel, Sylvain Danto, J David Musgraves, Kathleen Richardson, Lionel C Kimerling, and Anuradha M Agarwal. Mid-infrared materials and devices on a Si platform for optical sensing. *Science and Technology of Advanced Materials*, 15(1), 2014.
- [169] Meint Smit, Kevin Williams, and Jos van der Tol. Past, present, and future of InP-based photonic integration. *APL Photonics*, 4(050901), 2019.
- [170] Allan W. Snyder and John D. Love. *Optical waveguide theory*. Chapman and Hall, London, 1983.
- [171] Cheryl Sorace-Agaskar, Dave Kharas, Siva Yegnanarayanan, Ryan T. Maxson, Gavin Neal West, William Loh, Suraj Bramhavar, Rajeev J. Ram, John Chiverini, Jeremy Sage, and Paul W. Juodawlkis. Versatile Silicon Nitride and Alumina Integrated Photonic Platforms for the Ultraviolet to Short-Wave Infrared. *IEEE Journal of Selected Topics in Quantum Electronics*, 25(5), 2019.
- [172] Mario C.M.M. Souza, Andrew Grieco, Newton C. Frateschi, and Yeshaiah Fainman. Fourier transform spectrometer on silicon with thermo-optic non-linearity and dispersion correction. *Nature Communications*, 9(1):1–8, 2018.
- [173] Ananth Z Subramanian, Eva Ryckeboer, Ashim Dhakal, Frédéric Peyskens, Aditya Malik, Bart Kuyken, Haolan Zhao, Shibnath Pathak, Alfonso Ruocco, Andreas De Groote, Pieter Wuytens, Daan Martens, Francois Leo, Weiqiang Xie, Utsav Deepak Dave, Muhammad Muneeb, Pol Van Dorpe, Joris Van Campenhout, Wim Bogaerts, Peter Bienstman, Nicolas Le Thomas, Dries Van Thourhout, Zeger Hens, Gunther Roelkens, and Roel Baets. Silicon and silicon nitride photonic circuits for spectroscopic sensing on-a-chip. *Photonics Research*, 3(5):B47–B59, 2015.
- [174] Jie Sun, Erman Timurdogan, Ami Yaacobi, Ehsan Shah Hosseini, and Michael R. Watts. Large-scale nanophotonic phased array. *Nature*, 493:195–199, 2013.
- [175] Rong Sun, Po Dong, Ning-Ning Feng, Ching-Yin Hong, Michal Lipson, and Lionel Kimerling. Horizontal single and multiple slot waveguides: Optical transmission at $\lambda = 1550$ nm. *Optics Express*, 15(26):17967–17972, 2007.
- [176] Heba Tamazin, Eslam El-Fiky, Yun Wang, Yannick Damello, David Patel, Amar Kumar, and David V. Plant. Ultra-broadband Compact Adiabatic Coupler in Silicon-on-Insulator for Joint Operation in the C- and O-Bands. *2018 Conference on Lasers and Electro-Optics, CLEO 2018 - Proceedings*, 2018.
- [177] Christos Themistos, B M Azizur Rahman, Angelos Hadjicharalambous, Kenneth Thomas, and Victor Grattan. Loss/gain characterization of optical waveguides. *Journal of Lightwave Technology*, 13(8):1760–1765, 1995.

- [178] David Thomson, Aaron Zilkie, John E. Bowers, Tin Komljenovic, Graham T. Reed, Laurent Vivien, Delphine Marris-Morini, Eric Cassan, Léopold Virost, Jean Marc Fédéli, Jean Michel Hartmann, Jens H. Schmid, Dan Xia Xu, Frédéric Boeuf, Peter O'Brien, Goran Z. Mashanovich, and M. Nedeljkovic. Roadmap on silicon photonics. *Journal of Optics (United Kingdom)*, 18(7), 2016.
- [179] T. G. Tiecke, K. P. Nayak, J. D. Thompson, T. Peyronel, N. P. de Leon, V. Vuletić, and M. D. Lukin. Efficient fiber-optical interface for nanophotonic devices. *Optica*, 2(2):70–75, 2015.
- [180] Nathan F. Tyndall, Todd H. Stievater, Dmitry A. Kozak, Kee Koo, R. Andrew McGill, Marcel W. Pruessner, William S. Rabinovich, and Scott A. Holmstrom. Waveguide-enhanced Raman spectroscopy of trace chemical warfare agent simulants. *Optics Letters*, 43(19):4803–4806, 2018.
- [181] Nathan F. Tyndall, Todd H. Stievater, Dmitry A. Kozak, Marcel W. Pruessner, Scott A. Holmstrom, and William S. Rabinovich. Ultrabroadband lattice filters for integrated photonic spectroscopy and sensing. *Optical Engineering*, 57(12):127103, 2018.
- [182] Aitor V Velasco, Pavel Cheben, Przemek J Bock, André Delâge, Jens H Schmid, Jean Lapointe, Siegfried Janz, María L Calvo, Dan-Xia Xu, Mirosław Florjańczyk, and Martin Vachon. High-resolution Fourier-transform spectrometer chip with microphotonic silicon spiral waveguides. *Optics Letters*, 38(5):706–708, 2013.
- [183] William E. Wallace. NIST Mass Spectrometry Data Center. In P. J. Linstrom and W. G. Mallard, editors, *NIST Chemistry WebBook, NIST Standard Reference Database Number 69*, chapter Infrared S. Gaithersburg, MD.
- [184] Linghua Wang, Weiqiang Xie, Dries Van Thourhout, Yazhen Zhang, Hui Yu, and Shaohao Wang. Nonlinear silicon nitride waveguides based on PECVD deposition platform. *Optics Express*, 26(8):9645–9654, 2018.
- [185] Peng Wang, Aron Michael, and Chee Yee Kwok. Fabrication of sub-micro silicon waveguide with vertical sidewall and reduced roughness for low loss applications. *Procedia Engineering*, 87(612):979–982, 2014.
- [186] Xiaodong Wang, Xueling Quan, Min Liu, and Xiulan Cheng. Silicon-nitride-assisted edge coupler interfacing with high numerical aperture fiber. *IEEE Photonics Technology Letters*, 31(5):349–352, 2019.
- [187] Yun Wang, Luhua Xu, Han Yun, Minglei Ma, Amar Kumar, Eslam El-Fiky, Rui Li, Nicolas Abadiacalvo, Lukas Chrostowski, Nicolas A.F. Jaeger, and David V. Plant. Polarization-Independent Mode-Evolution-Based Coupler for the Silicon-on-Insulator Platform. *IEEE Photonics Journal*, 10(3), 2018.

- [188] J Gonzalo Wangüemert-Pérez, Pavel Cheben, Alejandro Ortega-Moñux, Carlos Alonso-Ramos, Diego Pérez-Galacho, Robert Halir, Iñigo Molina-Fernández, Dan-Xia Xu, and Jens H Schmid. Evanescent field waveguide sensing with subwavelength grating structures in silicon-on-insulator. *Optics Letters*, 39(15):4442–4445, 2014.
- [189] W. H. Weber, S. L. McCarthy, and G. W. Ford. Perturbation theory applied to gain or loss in an optical waveguide. *Applied Optics*, 13(4):715–716, 1974.
- [190] C. M. Wilkes, X. Qiang, J. Wang, R. Santagati, S. Paesani, X. Zhou, D. A. B. Miller, G. D. Marshall, M. G. Thompson, and J. L. O’Brien. 60 dB high-extinction auto-configured Mach-Zehnder interferometer. *Optics Letters*, 41(22):5318–5321, 2016.
- [191] Quentin Wilmart, Houssein El Dirani, Nicola Tyler, Daivid Fowler, Stéphane Malhouitre, Stéphanie Garcia, Marco Casale, Sébastien Kerdiles, Karim Hassan, Christelle Monat, Xavier Letartre, Ayman Kamel, Minhao Pu, Kresten Yvind, Leif Katsuo Oxenløwe, Wilfried Rabaud, Corrado Sciancalepore, Bertrand Szelag, and Ségolène Olivier. A versatile silicon-silicon nitride photonics platform for enhanced functionalities and applications. *Applied Sciences*, 9(2), 2019.
- [192] Michael G. Wood, Li Chen, Justin R. Burr, and Ronald M. Reano. Optimization of electron beam patterned hydrogen silsesquioxane mask edge roughness for low-loss silicon waveguides. *Journal of Nanophotonics*, 8(1):083098, 2014.
- [193] Kerstin Wörhoff, René G Heideman, Arne Leinse, and Marcel Hoekman. TriPleX: a versatile dielectric photonic platform. *Advanced Optical Technologies*, 4(2):189–207, 2015.
- [194] Fengnian Xia, Mike Rooks, Lidija Sekaric, and Yurii Vlasov. Ultra-compact high order ring resonator filters using submicron silicon photonic wires for on-chip optical interconnects. *Optics Express*, 15(19):11934–11941, 2007.
- [195] Fengnian Xia, Lidija Sekaric, and Yurii Vlasov. Ultracompact optical buffers on a silicon chip. *Nature Photonics*, 1(1):65–71, 2007.
- [196] Zhixuan Xia, Ali Asghar Eftekhar, Mohammad Soltani, Babak Momeni, Qing Li, Maysamreza Chamanzar, Siva Yegnanarayanan, and Ali Adibi. High resolution on-chip spectroscopy based on miniaturized microdonut resonators. *Optics Express*, 19(13):12356–12364, 2011.
- [197] Hai Yan, Lijun Huang, Xiaochuan Xu, Swapnajit Chakravarty, Naimei Tang, Huiping Tian, and Ray T. Chen. Unique surface sensing property and enhanced sensitivity in microring resonator biosensors based on subwavelength grating waveguides. *Optics Express*, 24(26):29724, 2016.

- [198] A. Yariv. Universal relations for coupling of optical power between microresonators and dielectric waveguides. *Electronics Letters*, 36(4):321–322, 2000.
- [199] David J Young and Norman C Beaulieu. The generation of correlated rayleigh random variates by inverse discrete Fourier transform. *IEEE Transactions on Communications*, 48(7):1114–1127, 2000.
- [200] Rukhsar Zafar and Mohammad Salim. Enhanced figure of merit in Fano resonance-based plasmonic refractive index sensor. *IEEE Sensors Journal*, 15(11):6313–6317, 2015.
- [201] Zhaojian Zhang, Junbo Yang, Xin He, Jingjing Zhang, Jie Huang, Dingbo Chen, and Yunxin Han. Plasmonic refractive index sensor with high figure of merit based on concentric-rings resonator. *Sensors*, 18(116):1–14, 2018.
- [202] Haolan Zhao, Stéphane Clemmen, Ali Raza, and Roel Baets. Stimulated Raman spectroscopy of analytes evanescently probed by a silicon nitride photonic integrated waveguide. *Optics Letters*, 43(6):1403–1406, 2018.
- [203] Haolan Zhao, Stéphane Clemmen, Ali Raza, and Roel Baets. Stimulated Raman spectroscopy of analytes evanescently probed by a silicon nitride photonic integrated waveguide. *Optics Letters*, 43(6):1403–1406, 2018.
- [204] S Zheng, H Cai, Y Gu, L K Chin, and A Q Liu. High-resolution on-chip spectrometer with a tunable micro-ring resonator filter. *Conference on Lasers and Electro-Optics (2016)*, 2:AM1J.2, 2016.